MSc. Eng. Sima Shabani

Title of thesis:

Analysis of the blade geometries for a highly efficient wet steam turbine stage

Doctoral dissertation

Scientific discipline: Environmental Engineering, Mining and Energy

Silesian University of Technology

Faculty of Energy and Environmental Engineering

Department of Power Engineering and Turbomachinery

Gliwice, Poland, 2025

Author:

Mgr inż. Sima Shabani

Silesian University of Technology
Faculty of Energy and Environmental Engineering
Department of Power Engineering and Turbomachinery
Konarskiego 18
44-100 Gliwice
Poland

Supervisor:

Dr hab. inż., Mirosław Majkut, prof. PŚ

Silesian University of Technology
Faculty of Energy and Environmental Engineering
Department of Power Engineering and Turbomachinery
Konarskiego 18
44-100 Gliwice
Poland

Polish title of the PhD dissertation:

Analiza kształtu profilu łopatkowego dla stopnia turbiny parowej o podwyższonej sprawności

List of Contents

Acknowledgement

First and foremost, I would like to express my deepest gratitude to my supervisor, Dr hab. inż., Mirosław Majkut, prof. PŚ, for their invaluable guidance, continuous support, and insightful feedback throughout the course of this research. Their expertise and encouragement played a critical role in shaping this work and helping me navigate the challenges of my doctoral journey.

I am also sincerely thankful to prof. dr hab. inż. Sławomir Dykas, the esteemed Dean of the Faculty, whose support and dedication to academic excellence provided an environment in which this research could thrive.

I am especially grateful to my spouse for his patience, understanding, and steady support throughout the course of this work. I also extend my heartfelt thanks to my parents, whose encouragement has been a constant source of strength, and to my friends, whose companionship and motivation helped me stay balanced during this demanding journey.

Nomenclature

c	Absolute velocity, m s^{-1}
C	Kantrowitz correction factor, -
c_p	Specific heat in constant pressure, J kg^{-1}K^{-1}
D	Droplet diameter, m
D_{32}	Sauter average diameter of droplet, m
h, H	Static enthalpy, J kg^{-1}
J	Nucleation rate, m^{-3}s^{-1}
k_B	Boltzmann constant, J K^{-1}
Kn	Knudsen number, -
l	Specific work, J kg^{-1}
L	Latent heat, J kg^{-1}
m	Molecular mass, kg
$\dot{m}$	Mass flow rate, kg s^{-1}
Ma	Mach number, -
n	Refractive index, -
N	Number of droplets, m^{-3}
p	Pressure, Pa
P_t	Output power, MW
Pr	Prandtl number, -
q_{Yo}	Young condensation coefficient, -
Q$_a$	Absorption coefficient, -
Q$_{ext}$	Extinction coefficient, -
Q$_s$	Scattering coefficient, -
r	Droplet radius, m
$r*$	Critical droplet radius, m
R	Gas constant, J kg^{-1}K^{-1}
s	Static entropy, J kg^{-1}K^{-1}
T	Temperature, K

t	Time, s
u	Velocity vector, m s^{-1}
V	Volume of the phases, m^3
w	Relative velocity, m s^{-1}
y	Liquid mass fraction, -

Greek Symbols

α_l	Liquid volume fraction, -
α	Flow angle
α_c	Condensation coefficient, -
α_{Yo}	Young empirical correction factor, -
β	Flow angle
β_c	Empirical correction factor, -
β_{Yo}	Young modelling parameter, -
γ	Ratio of specific heat, -
δ	Kronecker delta, -
η	Efficiency, -
λ	Thermal conductivity, W m^{-1}K^{-1}
μ	Dynamic viscosity, kg m^{-1}s^{-1}
ν	Young correction factor, -
ξ	Loss coefficients, -
ρ	Density, kg m^{-3}
σ	Surface tension, N m^{-1}
τ	Stress tensor, Pa

Subscripts

in	Inlet
l	Liquid
m	Mixture
out	Outlet
rel	Relative

R	Rotor
S	Stator
s	Isentropic, saturation state
v	Vapour
$_0$	Total parameters
i, j	Group number

Abbreviations

AS	Axial Sweep
ASCL	Axial Sweep Circumferential Lean
CL	Circumferential Lean
CNT	Classical Nucleation Theory
EOS	Equation of State
FS	Fuch-Sutugin
Gy	Gyarmathy
IAPWS	International Association for the Properties of Water and Steam
IWSEP	International Wet Steam Experimental Project
LEM	Light Extinction Method
LP	Low Pressure
LS	Last stage
NIST	National Institute of Standards and Technology
UDF	User-Defined Functions
Vu	Vukalovich
Yo	Young

1. Introduction

1.1 Fundamentals of wet steam flow in axial steam turbines

Axial steam turbines are crucial in many industrial applications due to their high efficiency and reliability, particularly for power generation and mechanical drives. They are commonly found in fossil fuel and nuclear power plants, and occasionally in renewable energy plants, to convert steam energy into electricity. In the oil and gas industry, they are essential for driving compressors and pumps used in extraction, refining, and transportation. Also in chemical processes, turbines power equipment and machinery are necessary for various technological processes. In petrochemical facilities, they drive machinery and generators, thus boosting plant efficiency. These examples represent just a fraction of the broad applications of steam turbines. This highlights the importance of studying and simulating the flow in steam turbine stages, especially in the final stages (low-pressure stages), where wet steam forms. During the expansion process in the low-pressure turbine, steam undergoes cooling and eventually nucleates, resulting in the formation of a two-phase mixture known as wet steam. The condensation phenomenon and presence of liquid droplets lead to losses that impact the turbine's efficiency.

In power stations, work is extracted from expanding steam through three stages: High Pressure (HP), Intermediate Pressure (IP), and Low Pressure (LP) turbines. During expansion in the LP turbine, steam cools and eventually nucleates, forming a two-phase mixture. It is well-documented that nucleating and wet stages in steam turbines are less efficient than those operating with superheated steam [1, 2]. This issue is exacerbated in water-cooled nuclear reactors, where the steam generated is saturated and supplied to the HP steam turbine, which must then handle wet steam. A significant problem associated with wet steam is blade erosion. Newly nucleated droplets are typically too small to cause damage, but some are collected by the blades and form films on the blade and casing walls. When these liquid streams reach the trailing edges or tips of the blades, they are re-entrained into the flow as larger coarse droplets. These larger droplets are responsible for erosion damage and braking loss in steam turbines. Additionally, the formation and behavior of these droplets have other important thermodynamic and aerodynamic effects that reduce the performance of the wet stages in steam turbines [3, 4]. Figure 1.1 demonstrates the process of steam expanding from a superheated state to a wet condition within the blades of a steam turbine. As steam moves through the turbine blades, it undergoes complex physical changes, particularly condensation, which significantly affects turbine operation and efficiency. Initially, high-pressure, high-temperature steam enters the

space between the blades as dry, superheated vapor at point (1). As it progresses through the channel, it expands, resulting in a pressure and temperature drop. This expansion continues until the steam reaches sonic conditions at point (2), where a transition from subsonic to supersonic flow occurs. At this point, the steam becomes supersaturated, crossing the saturation line and initiating the formation of droplet nuclei in the vapor—a process known as nucleation. By point (3), nucleation effectively stops, and the number of droplets stabilizes. Between points (3) and (4), these nuclei grow rapidly, driving the system back toward thermodynamic equilibrium. These condensation phenomena, governed by thermodynamics and fluid dynamics, are critical in understanding the behavior of steam in turbine stages and optimizing overall performance.

Condensation can occur in two forms: heterogeneous or homogeneous. Heterogeneous condensation occurs when vapor condenses on existing particles, such as dust, but in many engineering applications, like expansion flows in steam turbines, the lack of sufficient particles leads to homogeneous condensation, where nuclei form spontaneously in supercooled vapor. Interactions with shock waves in blade channels pose challenges, causes sudden changes in pressure and temperature, as supercooled droplets may evaporate or form ice upon impact. Simulating these processes is challenging due to the non-linear behavior of shock waves and the need for precise modeling to describe the size distribution of droplets accurately. Research can provide insights into wet steam generation and condensation, offering solutions to these challenges. Such studies are essential for improving turbine design, enhancing their ability to manage wet steam conditions, and resulting in more efficient turbines, ultimately benefiting power plants.
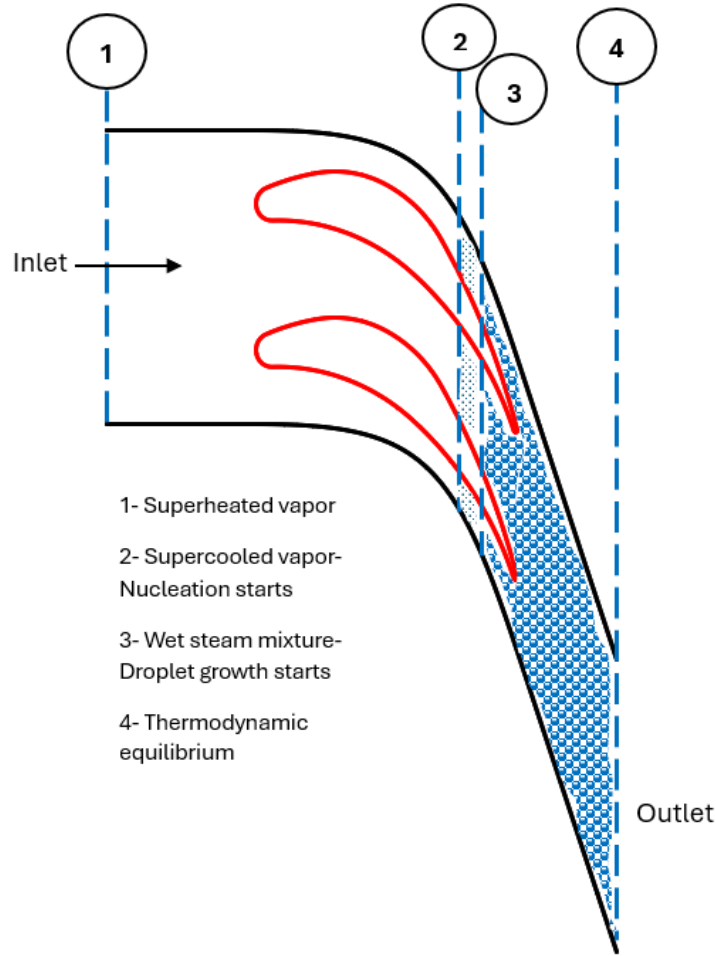
Fig. 1.1. The expansion process within the blades of LP section of a steam turbine

1.2 Literature review

The study of wet steam flows, particularly in supersonic nozzles, has been a significant focus in fluid dynamics research due to its practical implications in turbomachinery and power generation. For instance Young [5], Moses and Stein [6], and Barschdorff et al. [7] have contributed to this field using various numerical approaches to model condensation and droplet formation in steam flows. Furthermore, the wet steam flow simulations within the steam turbine blades especially in LP part has attracted the attention of many researchers. For instance, Bakhtar et al. [8], White [9], and Dykas et al. [10] have implemented significant contributions to model flows in condensing turbine blades conditions. The above mentioned studies are the base and benchmark for the nowadays researches and have advanced our understanding of this field. However, further improvements in modelling methods are required, as numerical results often do not fully match experimental data, indicating persistent uncertainties in this area. This topic is the main goal and focus of section 1.2.1. Furthermore, the experimental studies

presented in the publications are typically conducted using standard research methods, which primarily provide data on pressure distributions within the test channels. However, there is often a lack of experimental data on crucial aspects such as droplet size, droplet at key flow points, and flow visualization within the channels. Incorporating this type of information would enhance the depth of the research and significantly increase the credibility of numerical analysis results. It is also important to estimate losses in such flows and have a clear understanding of the amount of losses in real industrial cases. This is the main aim of section 1.2.2. After this step, it is necessary to explore and change the blades configuration and find the optimal condition to get the highest performance of the stage. This topic will be considered in section 1.2.3.

1.2.1. CFD simulation tools to model wet steam flows

Accurately predicting steam condensing flows is essential for optimizing system efficiency and performance. However, the complex nature of the condensation process makes developing effective numerical models, that can accurately capture the behaviour of steam during condensation, a challenging endeavor. In recent years, there has been growing interest in creating numerical models to predict steam condensing flows accurately [11, 12]. Among these studies, numerical methods developed for modeling such flows in in-house academic codes have constituted a significant part of the research. Notable examples include numerical codes developed by Cambridge University [13], Czech Technical University [14, 15], Silesian University of Technology [16], or Tohoku University [17, 18]. Although these codes demonstrate remarkable capabilities in simulation and can be developed, they are specific to particular applications and, therefore, cannot be generalized. However, in typical engineering practice, access to methods of calculation and design of structures based on widely available commercial tools, which are constantly reinforced by the results of scientific research, is more important. In this case, the issue of their application to difficult research problems, which is undoubtedly the phenomenon of steam condensation in the flow, and indicating their usefulness in the design process, becomes important. Hence, the aim of this study is to investigate the available commercial codes, which are universally accessible and usable.

The commercial codes discussed in this study, including ANSYS CFX and ANSYS Fluent, offer various tools for CFD simulation. Among these, different condensation models and equations of state play a crucial role, which constitutes the primary focus of this research. A detailed examination of these models and equations will be presented in Chapter 3. One of the significant projects that has addressed this topic is the "International Wet Steam Modeling Project"[19]

which evaluates computational methods in predicting condensing steam flows, comparing various approaches against experimental data from several nozzle test cases. In the study, thirteen research groups conducted calculations on several nozzle cases using various wet-steam flow solvers. While some methods showed reasonable alignment with experimental data, a noticeable variability in results was observed. This inconsistency largely originates from the different condensation models employed, as well as the specific implementation of these models and the characteristics of the underlying flow solvers used in the analysis. The study underscores the impact of nucleation and droplet growth models, alongside the critical role of the equation of state in determining the Wilson point. Therefore, exploring the appropriate condensation model and EOS which can be applied to the test cases under consideration in this study, is a significant step.

Selecting the appropriate condensation model is crucial for accurately capturing the complex phenomena occurring during the phase transition from vapor to liquid. Nucleation is the initial stage of phase change in the condensation process. As more molecules collide and interact, the phase transition continues, leading to the growth of condensed particles. The nucleation rate determines the formation rate of critical clusters per unit volume and time in a supersaturated state. Zeldovich [20] introduced a probability factor that accounts for the effects of evaporation in both critical and post-critical clusters. In 1935, Becker and Döring [21] developed the Classical Nucleation Theory (CNT), which serves as a fundamental framework for nucleation rate calculations. Today, this theory remains widely used as the basis for nucleation rate estimations in numerous research studies [22, 23]. Several modifications to CNT have been proposed by researchers [24-26] to enhance the accuracy of nucleation rate modeling. Among these, the Kantrowitz modification [26] is particularly well-known and has demonstrated high accuracy in predicting experimental data across numerous studies [19, 27]. The classical nucleation rate model assumes that clusters remain isothermal with the surrounding vapor. However, in reality, a temperature difference exists between the forming clusters and the steam, causing latent heat to transfer from the clusters to the flow. To account for this effect, Kantrowitz introduced a correction by modifying the evaporation rate in the CNT model to apply the correction of the temperature difference.

The accuracy of the growth model is just as crucial as the nucleation rate in droplet condensation problems. If the vapor is supersaturated, molecules diffuse through the gas mixture and condense on the droplet surface. During this process, the conversion of vapor molecular kinetic energy to heat at the droplet surface releases latent heat, which increases the temperature of the

surrounding flow. As a result, droplet growth is governed by heat and mass transfer between the droplet and the surrounding vapor. In general, droplet growth occurs in two stages:

1. Vapor diffusion from the gaseous region to the droplet's vicinity.

2. Molecular adhesion through collisions at the droplet surface from the Knudsen layer— a thin interfacial region where phase change is governed by molecular dynamics.

The selection of an appropriate growth rate model depends on the droplet Knudsen number (Kn), which determines the dominant condensation mechanism. Based on this parameter, droplet condensation is classified into three distinct regimes:

1. Continuum Regime (Kn < 0.01): In this regime, the mean free path of molecules is significantly smaller than the droplet diameter, leading to condensation governed primarily by pure diffusion. This regime typically applies to larger droplets with diameters exceeding 10 microns.

2. Transition Regime (0.01 < Kn < 4.5): Here, a Knudsen layer forms around the droplet, where kinetic effects influence the condensation or evaporation rate. However, beyond this interfacial layer, the surrounding gas behaves as a continuum medium.

3. Free Molecular Regime (Kn > 4.5): In this case, the mean free path of molecules is much larger than the droplet diameter, and condensation occurs through molecular collisions rather than diffusion. This regime is typical for nucleated droplets or flows undergoing high-speed expansion.

Each regime requires a different modeling approach to accurately describe the phase change dynamics and predict condensation behavior under various flow conditions. Spalding [28] developed a general equation for droplet growth that simultaneously considers mass and energy transfer between the droplet and the surrounding gas, ensuring an accurate representation of the process within the continuum flow regime. In the free molecular regime, the kinetic theory of gases must be applied to determine heat and mass transfer from the droplets. In this regime, the Hertz-Knudsen model [29] is used to estimate the droplet growth rate by linking the impingement flux of vapor molecules to their thermophysical properties. Although the mentioned models describe droplet growth in both the continuum and free molecular regimes, they fail to accurately predict growth in intermediate Knudsen number ranges, where droplets often evolve in supersonic nozzle flows. Therefore, a generalized formulation covering a wide range of Knudsen numbers is essential for more reliable predictions. There are several well-

known models, including those by Bakhtar and Zidi [30], Young [31], and Peters and Paikert [32]. They proposed equations that bridge the continuum and free molecular regimes using an interpolation technique. These models incorporate a wide range of droplet growth behaviors by utilizing the Knudsen number in their formulations. Gyarmathy [33] further simplified the general droplet growth equation by introducing an approximate definition for droplet temperature. Studies [34] have shown that Young and Gyarmathy's models closely align with experimental data for both single- and multi-component flows. Since these two models are among the most widely used for droplet growth predictions and are available in commercial CFD codes, they are selected in this study to evaluate the best condensation model for the test cases in Chapter 3.

An equally crucial aspect in developing numerical models for steam condensing flows is the selection of equations of state (EOS). The choice of a suitable EOS depends on various factors such as the specific application, temperature and pressure ranges, and the required prediction accuracy. In recent years, researchers have investigated different formulations to describe the thermodynamic behaviour of steam during condensation. Hanimann et al. [35] utilized two real gas equations of state and applied them to a transonic nozzle and a radial compressor, comparing their simulation results with those of the ideal gas model to highlight its limitations. Raman and Kim [36, 37] employed six different EOS to estimate flow characteristics through a converging-diverging nozzle. Wen et al. [38] developed a CFD model to examine how thermodynamic properties influence condensation, using a real gas model and comparing it to the ideal gas model, which consistently underestimated condensation. Furusawa et al. [39] proposed a method for estimating an EOS for supercooled gas, applicable to both low-pressure and high-pressure condensing flows. However, despite the significant effort of studies on this topic, there are few studies that utilize an EOS capable of accurately calculating the thermodynamic properties of steam in the wet-steam region (below the saturation line). The problem is that the equations of state for steam in the literature commonly refer to equilibrium states (dry-steam region). In order to compute the properties of supercooled vapor, it is important to extrapolate these equations into the meta-stable zone, which is beyond their valid range. Furthermore, the limited research in this area often employs equations that cannot be generalized to similar projects modelled in commercial codes. Thus, further research is needed to accurately predict the thermodynamic properties of supercooled steam. There are some common EOS which are available in commercial CFD codes. Virial equations developed by Vucalovich and the other by Young are available in ANSYS Fluent and have been utilized in some research [40, 41]. These

equations are general equations for calculating the wet steam thermodynamic properties, which use the virial coefficients, but their accuracy will be examined in chapter 3. IAPWS-IF97 formulations [42] which is available in ANSYS CFX, is a popular option among researchers for estimation of wet steam properties. They are tabular data which were developed by International Association for the Properties of Water and Steam. There is also another option in ANSYS Fluent, NIST real gas models [43], developed by National Institute of Standards and Technology. When one of the NIST real gas models is enabled, the solver dynamically loads the REFPROP v9.1 shared library to calculate the properties of the fluids. The comparison between the options available in commercial CFD codes for calculating wet steam thermodynamic properties showed that the IAPWS-IF97 results in more accurate simulations than the Virial equations [44-46].

1.2.2. The losses in wet steam flows within the condensing steam turbine

Steam turbines are subject to various types of losses that collectively reduce their efficiency and performance. These losses can broadly be categorized into thermodynamic, fluid dynamic, aerodynamic, and mechanical degradation losses. Thermodynamic losses arise from the deviation between actual turbine behavior and its ideal thermodynamic cycle, often due to irreversibilities during steam expansion. Closely related are fluid dynamic losses, which include both pressure drop and shock losses. Pressure drop losses are primarily caused by frictional resistance as steam flows through turbine stages, resulting in reduced energy transmission. In contrast, shock losses occur when steam flow reaches supersonic speeds, creating shock waves that abruptly dissipate kinetic energy and adversely affect performance. Aerodynamic losses are such as blade profile losses and flow separation. Blade profile losses occur due to imperfections in the blade design or surface roughness, leading to less effective conversion of thermal energy into mechanical energy. Additionally, flow separation happens when steam flow detaches from the surface of the blades, and creates turbulence and recirculating flow, leading to a loss in the efficiency of energy conversion. Another major source of inefficiency comes from exhaust heat losses. After passing through the turbine, residual thermal energy in the steam is often not recovered, especially in systems lacking cogeneration or heat recovery, which contributes to overall system inefficiency. Lastly, erosion and corrosion of turbine blades constitute mechanical forms of loss. Erosion occurs as high-speed droplets impact blade surfaces, leading to material wear. Corrosion, on the other hand, is driven by the presence of moisture and impurities in the steam, which can chemically degrade the metal components over time.

Understanding and minimizing condensation losses in the low-pressure sections of steam turbines have been a central research focus, as these losses significantly affect turbine efficiency. Several studies have addressed this issue using various numerical methods to simulate and compute the thermodynamic and aerodynamic losses associated with wet steam flow. Kermani and Gerber [47] developed a general formula for evaluating thermodynamic and aerodynamic losses in nucleating steam flows. Their work emphasizes using analytical methods combined with computational fluid dynamics to model the complex interaction between steam flow and condensation processes. They highlight challenges in accurately capturing the onset of nucleation and droplet growth, which are critical for reliable loss estimation. Yu et al. [48] proposed a 3D method to evaluate moisture losses in a low-pressure steam turbine, focusing on the last stage. They highlight the need for improved boundary condition models to better simulate real operating conditions. Bahr Ennil et al. [49] explored the minimization of losses in small-scale axial air turbines using CFD modeling and evolutionary algorithm optimization. Their study show the potential of combining CFD with optimization techniques to reduce aerodynamic losses. This specific focus on the small-scale applications limits the findings' applicability to larger industrial systems without further validation or scaling analysis. Ding et al. [50] focused on the energy efficiency and exergy destruction in supersonic steam ejectors, using a nonequilibrium condensation model. Their numerical approach integrates CFD simulations to account for nonequilibrium effects during condensation, providing insights into the inefficiencies that arise from rapid phase transitions. A key challenge identified is the accurate representation of nonequilibrium states, which can lead to discrepancies between predicted and actual performance. Wen et al. [51] investigated condensation losses in turbine blade cascades, utilizing detailed CFD simulations to analyze wet steam flows. Their study emphasizes the role of blade geometry in influencing condensation losses. They identify the need for more refined models to better predict the interaction between the flow and blade surfaces, which is crucial for optimizing blade designs to reduce losses. Vatanmakan et al. [52] investigated the entropy generation in condensing steam flows within turbine blades with volumetric heating. They suggested a volumetric heating method to reduce wetness and minimize entropy generation. However, their study lacks a practical correlation for calculating wetness-related losses. Lampart et al. [53] applied numerical optimization techniques to improve the flow efficiency of high-pressure and low-pressure steam turbine stages through 3D blading designs. Their work demonstrates how optimization algorithms can be used in conjunction with CFD to enhance turbine efficiency. However, they note the difficulty in capturing three-dimensional flow effects and the need for more sophisticated models to account

17

for complex geometrical features. Wróblewski et al. [54] evaluated the efficiency of LP steam turbines based on experimental measurements, combining results with numerical analysis. Their research highlights the importance of accurate measurement techniques to validate CFD models. They point out the challenges in aligning numerical results with empirical data, especially in the presence of high moisture content. Bondyra et al. [55] focused on the development of the last stage blade of the 13K215 turbine intermediate pressure module. They used advanced numerical techniques to optimize blade geometry for improved efficiency. Their research emphasizes the need for continued innovation in blade design to reduce condensation-related losses.

Despite progress in modeling wet steam flows, there are still challenges in applying these findings to industrial applications. Many studies focus on small scales, which makes it hard to use the results for large scale systems without more testing. Additionally, some research uses 2D models which may fail to capture the complex three-dimensional effects present in actual turbine blade structures, potentially affecting the accuracy of performance predictions. Furthermore, the lack of practical correlations for calculating wetness-induced losses limits the real-world applicability of these models. Therefore, to address these issues, the use of a realistic three-dimensional model is essential, as well as the development of a method to accurately estimate the existing losses. This topic is the main focus of chapter 4, and will be discussed further in detail.

1.2.3. Improving steam turbine performance through changing the blades configuration

Interest in researching wet steam emerged from the necessity to improve the efficiency of steam turbines used in power generation. This topic has become increasingly significant in recent decades due to the sharp rise in fuel costs. Traditionally, efforts to improve turbine efficiency concentrated on the high- and intermediate-pressure sections. Recently, however, manufacturers have shifted focus to the LP section. The LP section of the steam turbine accounts for a significant portion of the total power output, highlighting the importance of optimizing this section in modern turbine design [54]. This topic will be considered in chapter 5.

Enhancing the efficiency of this section at specific exhaust pressures can be achieved by lengthening the last stage blades (LSBs). This either reduces the number of LP modules needed or increases power output at lower condenser pressures with the same number of modules. However, extending the LSBs can significantly raise mechanical stresses and vibrations. These

blades are characterized by high centrifugal forces, high blade speeds, and relatively large unsteady flow forces during low-load operations, leading to increased maintenance needs and a higher risk of mechanical failure, which can negatively affect the turbine's reliability and lifespan. Heidari et al. [56] examined a three-dimensional model of steam turbine blades varying in length and thickness. Their findings revealed that longer blades experienced higher maximum Von Mises stress and strain compared to shorter blades. This is attributed to shorter blades having less surface area, resulting in lower force and deformation compared to longer blades. Moreover, thicker blades exhibited lower maximum Von Mises stress and strain than thinner ones, as increased thickness reduces the likelihood of bending or deformation compared to thinner blades.

Numerous researchers have conducted studies aimed at optimizing the geometry of turbine blades. The optimization process involves two key steps: First, select the optimization method and define the objectives. Second, identify the variables or parameters to be adjusted in the geometry to achieve the desired goal. Ansari et al. [57] applied an optimization method to mitigate wet steam loss and erosion rates. They also treated the blade as a component of the turbine stage, thereby assuming constant aerodynamic conditions at the inlet and outlet. Gribin et al. [58] employed parametric methods to optimize the stator blade profile, aiming to minimize kinetic energy losses and reduce the wetness fraction. They maintained constant mass flow rate and pressure drop during their analysis. Their focus area extended from the start of diffuser flow on the suction side to the blade's trailing edge. Additionally, they ensured that optimizing the suction side did not induce boundary layer separation in this region. Noori et al. [59] demonstrated that each optimization scenario should integrate two primary objective functions: minimizing entropy generation and minimizing maximum droplet diameter. The former targets reductions in thermodynamic and aerodynamic losses associated with condensing flow, while the latter aims to mitigate erosion losses caused by wet steam. Additionally, they observed that in non-condensing flows, optimization should be applied predominantly at the blade leading edge, whereas in condensing flows, the main modifications should occur near the blade trailing edge where nucleation occurs.

Some researchers made changes to the stator trailing edge and investigated its effects. For instance, Muhammad et al. [60] studied the impact of varying the thickness of the trailing edge of the stator. They observed that reducing the thickness of the trailing edge led to higher stator efficiency. This reduction in thickness resulted in an increased cross-sectional area of the steam flow, thereby lowering the steam expansion rate and subsequently reducing the nucleation rate. Cutback treatment is a repair method that involves removing the deteriorated trailing edge of a

turbine blade to prevent further cracking and potential blade fracture. Miyazawa et al. [61] tried the cutback method to repair the damaged trailing edge. Although this method reduced replacement costs, it had a negative impact on turbine performance. Wen et al. [62] discovered that increasing the cutback of the trailing edge results in higher expansion flow within the blade cascade and causes the homogeneous nucleation process to begin earlier. A 14% cutback of the trailing edge is considered suitable for repairing damaged blades, taking into account flow structure, nonequilibrium phase change, and condensation loss. However, a 21% cutback of the trailing edge leads to significant flow separation on the suction side and severely deteriorates flow structures in the blade cascades, ultimately resulting in unacceptable blade performance. Tavassoli khoei et al. [63] studied the impact of reducing the chord length on the losses. They discovered that optimizing the blade profile with a 4% reduction in chord length effectively decreased the liquid mass fraction, average droplet radius, and erosion rate, while also enhancing power output. However, to fully assess the real impact of these modifications, further investigation is required to evaluate the performance of the proposed profile within the entire turbine stage and assess its effects on the rotor flow dynamics.

Some researchers investigated the effects of changes in the flow expansion rate. For instance, Schippling et al. [64] examined the impact of varying expansion rates on condensation and the wetness loss in a Laval nozzle. They found that wetness reduction is achieved by reducing the expansion rate. In their study, the higher expansion rate in the diverging section of the nozzle resulted in a shorter nozzle length compared to the original design. Conversely, when the expansion rate was lower, a longer nozzle was necessary to allow the flow to expand to the desired outlet pressure ratio, compared to the original nozzle geometry. Keisari and Shams [65] conducted research on optimizing the shape of wet steam nozzles using a response surface model and genetic algorithm. They achieved an optimal nozzle shape characterized by a lower initial expansion rate compared to the baseline, resulting in earlier droplet nucleation conditions and reduced droplet formation in the condensation shock zone. Zhao et al. [66] studied the impact of altering the angle of the divergent section of a nozzle. They observed that increasing the angle resulted in decreased pressure and temperature within the divergent section, while the Mach number increased. Additionally, they found that increasing the angle led to higher rates of nucleation and liquid mass fraction. Nugraha et al. [67] explored the impact of varying the tilt angle of steam turbine blades. They found that for optimal performance, an optimal tilt angle of 35 degrees is ideal for aluminum alloy blades. At this angle, minimum deformation, minimum stress and strain occur.

1.3 Motivation and Goal

The ongoing research in numerical modelling of steam condensing flows has attracted significant attention due to its critical importance in various industrial applications. Recent studies, though extensive, represent only a fraction of the comprehensive efforts dedicated to this field. The motivation behind this thesis stems from the need to identify and develop suitable numerical models for simulating wet steam flow within steam turbine blades accurately. By exploring different condensation models and equations of state, this research aims to contribute valuable insights and tools for the engineering community. By conducting simulations and validating them against experimental data, this study seeks to determine the most proper numerical models for predicting condensation phenomena.

Moreover, the last stage of steam turbines, especially the stator blades, is a critical area where significant energy losses can occur. Understanding the flow behavior around these blades is pivotal for improving turbine efficiency. This thesis addresses these issues by employing advanced computational fluid dynamics (CFD) simulations to model the wet steam flow around stator blades, aiming to improve the blade configuration and reduce energy losses.

The primary goal of this thesis is to advance the understanding and modelling of steam condensing flows through numerical simulations and experimental validation. To achieve this, the research is structured around several key objectives:

1. Selection and evaluation of condensation models: The study aims to investigate various condensation models and equations of state to identify those that provide the most accurate predictions of steam condensing flows. Several cases are created using these models to simulate the flow through a Laval nozzle and a linear cascade (chapter 3).

2. Validation against experimental data: To ensure the reliability of the numerical models, the simulated results are validated against in-house experimental data. This validation process is crucial for confirming the accuracy and applicability of the models in real-world scenarios (chapter 3).

3. Simulation of 3D flow in steam turbines: Addressing a significant research gap, the thesis delves into the simulation of wet steam flow through the actual three-dimensional geometry of the last stage of a steam turbine. This aspect of the study is essential for understanding the complex flow patterns and energy losses in real turbine blades (chapter 4).

4. Improving the stator blades configuration: By analyzing the wet steam flow around the stator blades of a 200 MW steam turbine, the research aims to improve the blade configuration. The improvements focus on reducing energy losses. This objective is achieved through detailed CFD simulations and subsequent analysis (chapter 5).

In summary, this thesis aims to bridge the gap between numerical modelling and engineering application of steam condensing flows, providing engineers and researchers with the tools and knowledge necessary to design and optimize steam condensation systems. The ultimate goal is to improve energy efficiency, and enhance the operational performance of steam turbines, thereby contributing to the advancement of sustainable energy solutions.

2. Experimental study

The experimental study was conducted in a steam tunnel installed in the Machine Hall of the Silesian University of Technology. This facility uses superheated steam to simulate the conditions occurring in the last stages of a low-pressure turbine, with precise control of steam parameters. The research focuses on various measurement techniques, particularly the light extinction method (LEM), to evaluate wet steam flows and droplet sizes. The setup detail and calibration of the experimental apparatus, as well as the use of specialized probes, flow, pressure and temperature sensors are presented. Additionally, this chapter presents experimental results for the geometries, including a Laval nozzle and blade cascade, providing insights into the performance and behavior of steam flow in turbine components.

2.1 Steam tunnel facility

The steam tunnel (Fig. 2.1) is supplied with superheated steam generated by a 1 MW boiler, with the maximum steam mass flow rate reaching around 3 kg/s. Before the steam enters the test section (6), precise control over steam pressure and temperature is achieved through a control valve (1) and an additional desuperheater (14). This ensures that the steam conditions match those typically encountered in low-pressure turbine stages. After passing through the test section (6), the steam flows into a condenser (11). A throttling valve (13) is installed between the test section and condenser to regulate the back pressure behind the test section. A bypass pipe (2) and a system of valves (3, 4) ensure the safe operation of the test section. The test facility is capable of varying a wide range of inlet parameters; the inlet total pressure can range from 70 to 150 kPa, and the inlet total temperature from 70 to 150°C.
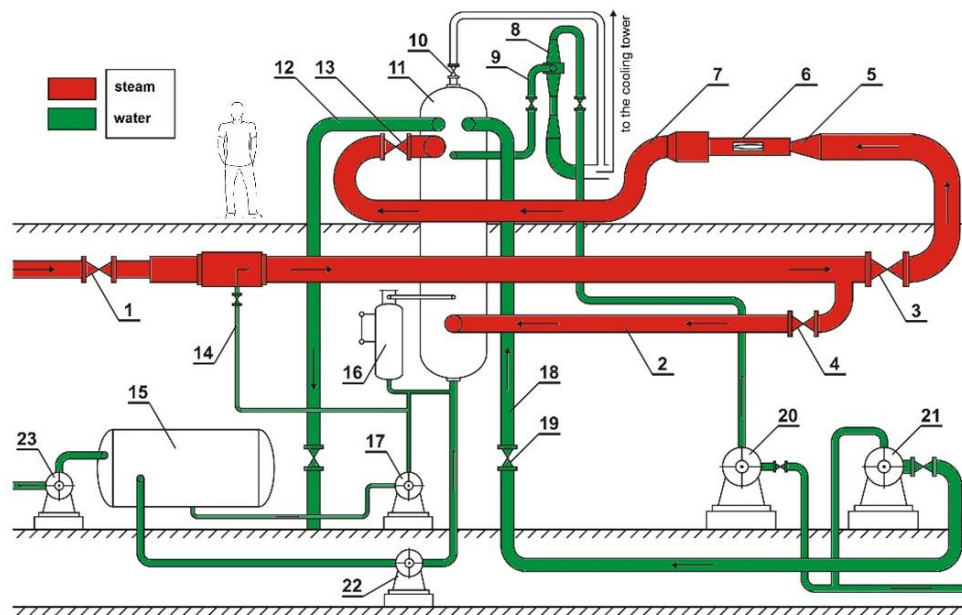
1 – control valve; 2 – by-pass; 3 – stop gate valve; 4 – stop gate valve at by-pass; 5 – inlet nozzle; 6 – test section; 7 – outlet elbow; 8 – water injector; 9 – pipe; 10 – safety valve; 11 – condenser; 12 – suction line; 13 – throttle valve; 14 –desuperheater; 15 – condensate tank; 16 – control system of the condensate level; 17 – condensate pump; 18 – discharge line; 19 – stop valve; 20 – water injector pump; 21 – cooling water pump; 22 – condensate pump; 23 – pump

Fig. 2.1. Steam tunnel facility

2.2 Mesearement Techniques

2.2.1. Light extinction method (LEM)

There are currently many measuring methods available for determining the wetness mass fraction of water vapor. Each technique has its advantages and disadvantages and is useful in a specific application field. Moreover, different techniques usually have different temporal and spatial resolutions, and some techniques may require wide optical access, making the practical implementation of such measurement in industrial settings difficult. Among the methods examined so far, techniques based on the phenomenon of light extinction are of particular interest, attractive due to their relative simplicity of implementation and data interpretation, the possibility of continuous measurement with fast response, as well as very limited optical requirements in terms of access to the measurement area. The experimental studies presented in this chapter are intended to significantly enhance the usefulness of the analytical results due to the distinct lack of such studies, particularly those focusing on the determination of particle size and number, in the widely available scientific literature. Therefore, in the further part of

the thesis, great attention was given to the development of the probe and to improving its accuracy and repeatability. Light is part of the electromagnetic spectrum that propagates at a constant speed in a vacuum. Light scattering is defined as the interaction of light and matter leading to a partial change in the direction of light propagation. Scattering is related to the inhomogeneities of the system, and its nature and method of impact depend largely on the size of the scattering particles. In wet steam flows, droplets primarily form through homogeneous or heterogeneous condensation. These droplets—both primary and secondary—typically range in size from 1 μm to 100 μm. As illustrated in Fig. 2.2, as the radius of the scattering particles increases, there is a shift in scattering symmetry, resulting in more forward scattering. Over a broad range of wavelengths, from 0.1 μm to 10 μm, the Mie scattering effect dominates. The key parameters influencing this scattering are:

- The wavelength of the incident radiation (λ)

- The size of the scattering particles, commonly expressed by the dimensionless parameter $X = 2\pi r/\lambda$, where r is the particle radius

- The refractive index, which accounts for the optical properties of the material.
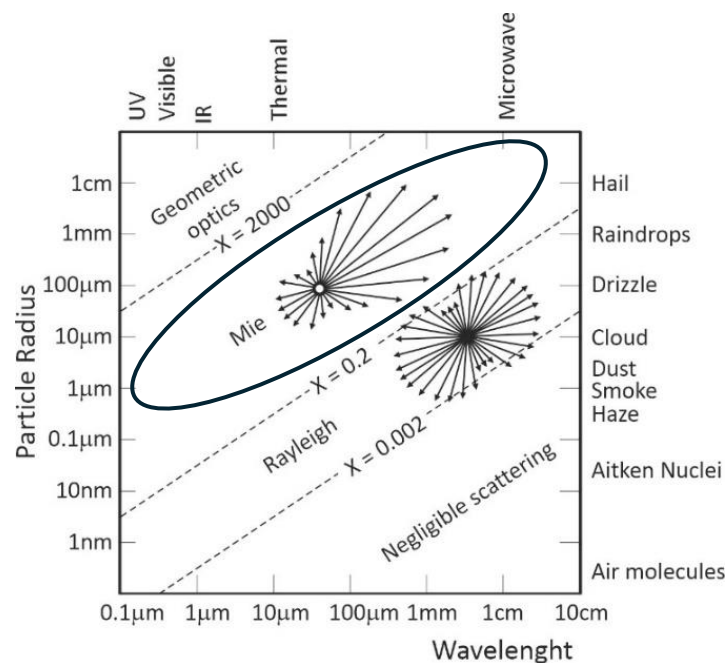
Fig. 2.2. Light scattering regimes [68]

In the literature on droplet size measurement methods, the light scattering method is often called the light absorption (extinction) method. In this method, a wave with length λ and original intensity $I_0(\lambda)$, after passing a distance L through the medium of homogeneous particles, is weakened to intensity $I(\lambda)$ (Fig. 2.3).
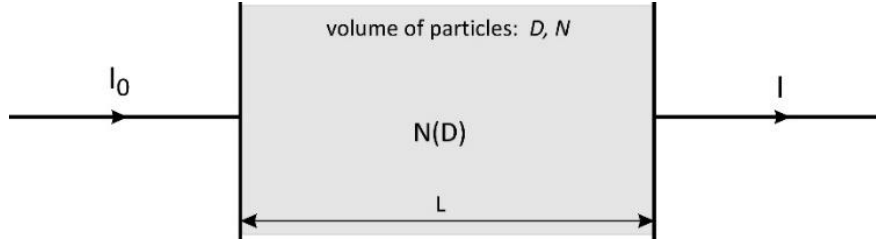
Fig. 2.3. Scheme of attenuation of the primary intensity I_0 after crossing distance L in the light extinction method

In the proposed method, taking into account the dependence of both intensities on the wavelength and defining the optical thickness as ξ, it can be expressed as:

$$I(\lambda) = I_0(\lambda) \exp[-\xi(\lambda)]. \tag{2.1}$$

The developed in-house calculation procedure involves determining the variables of the Bouguer-Lambert-Beer law across the entire measured wavelength range of light. Figure 2.4 illustrates this principle graphically, showing a curve that represents the relationship between the extinction coefficient and the wavelength, based on the measurements. The acquisition of the measurement system was based on the Modbus communication protocol programmed in the LabView environment. Figure 2.5 shows the user panel in the measurement data processing mode.

By applying Mie's law and using the Q_{ext} coefficient, the final form of the equation can be derived as:

$$\frac{1}{L} ln\left(\frac{I_o}{I}\right) = \int_{D_{min}}^{D_{max}} \frac{\pi}{4} D^2 \cdot Q_{ext}(D, \lambda, n) \cdot N(D) \, dD. \tag{2.2}$$

On the right side of the equation, we can identify a term that accounts for the droplet dimensions and their numerical distribution. On the left side, there is a vector determined through direct measurement using a spectrometer. The critical problem with LEM is the determination of

particle size distribution from the measured extinction spectrum, caused mainly by the oscillation behavior of the kernel function versus particle size, namely the extinction coefficient Q_{ext} versus the size parameter X, which often leads to ill-posed equations. To solve the equation, we need to compute the inverse matrix and address the inverse problem. Several methods exist for solving this problem, with the most widely used being the classic NNLS (non-negative least squares) approach, as outlined by Philips and Twomey in [69]. The NNLS method is a regression technique that ensures the coefficients obtained are non-negative (or zero). In the calculation procedure developed over several years at the Department of Power Machines and Turbomachinery [70], due to the significant impact of the analysis on the accuracy of the obtained results, several methods for solving the inverse matrix were used. In addition to the mentioned standard NNLS method, commonly found in applications of typical Matlab or C++-type program libraries, the new iterative INNLS method [71] and the approximation method based on smoothing of the NNLS results (TEOR), were also employed. The NNLS algorithm performs well in terms of computational speed, however, the inversion accuracy is not so satisfactory. On the other hand, the accuracy of the INNLS is highly dependent on the initial value. Therefore, the inversion result of the NNLS algorithm is used as the initial value of the iteration of INNLS. The results obtained from all three methods used are usually quite similar, however they differ in how they determine the distribution of diameter sizes around the maximum value. In the final stage of the calculations, the standard NNLS method typically produces diameter distributions with multiple peak maxima, concentrating the number of particles only at these diameters. For Gaussian size distributions, this often leads to a significant overestimation of the average number of particles in the solution. The remaining methods provide interpolated type distributions over the obtained diameter range, resulting in maximum and average values of the number of particles that are much closer to the actual known sizes of calibration particles. While for single standard calibration particle diameters, all methods yield similar results, in the case of actual steam flows, the INNLS and TEOR methods are closer to the expected values.
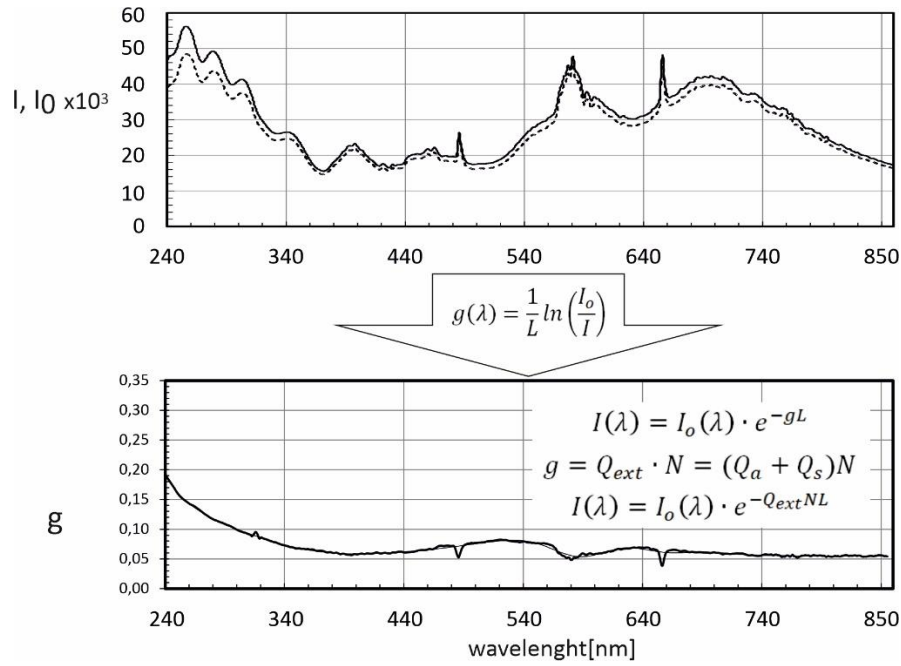
Fig. 2.4. Light intensity curves I and I_o (SUT system - experimental measurement) and the curve of the extinction coefficient (g) as a function of the wavelength of light

The equations shown in the figure:

$$g(\lambda) = \frac{1}{L} \ln\left(\frac{I_o}{I}\right)$$

$$I(\lambda) = I_o(\lambda) \cdot e^{-gL}$$
$$g = Q_{ext} \cdot N = (Q_a + Q_s)N$$
$$I(\lambda) = I_o(\lambda) \cdot e^{-Q_{ext}NL}$$
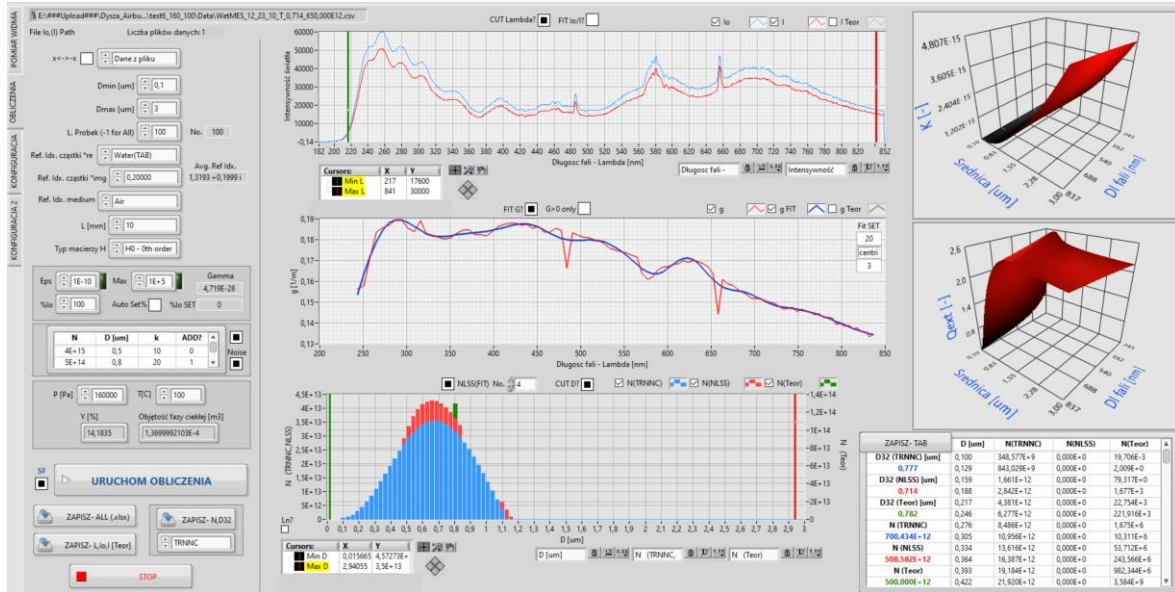
Fig. 2.5. WetMES Application (measurement and analysis)

The LEM system consists of components including a deuterium-halogen light source, a spectrometer, and a traverse system. The use of deuterium light in the system extends the range of particle size determination accuracy, particularly for particles approaching the smallest sizes (~0.1-0.2 μm). Theoretically, the Mie parameter for the smallest particles recorded at the lowest applied UV light wavelength (240nm), with an acceptable extinction efficiency ($Q_{ext} > 0.5$), is

X > 1.75. When converted to the minimum droplet size for this method, this results in D>134nm.

For measurements of the liquid phase, different configurations of the light extinction measuring systems were proposed. One method, previously used, involves the use of a NIOP-X probe in the form of a cylinder, immersed inside the steam flow channel, and the other involves the probe optics being placed on the external walls of the channel, not interfering with the flow inside the tunnel. Both types of probes are equipped with software designed to automate the measurement process and perform real-time signal analysis. The NIOP-X probe features a three-hole design, allowing it to measure multiple temperatures and pressures, as well as to determine the flow angle relative to the measurement area (Fig. 2.6).
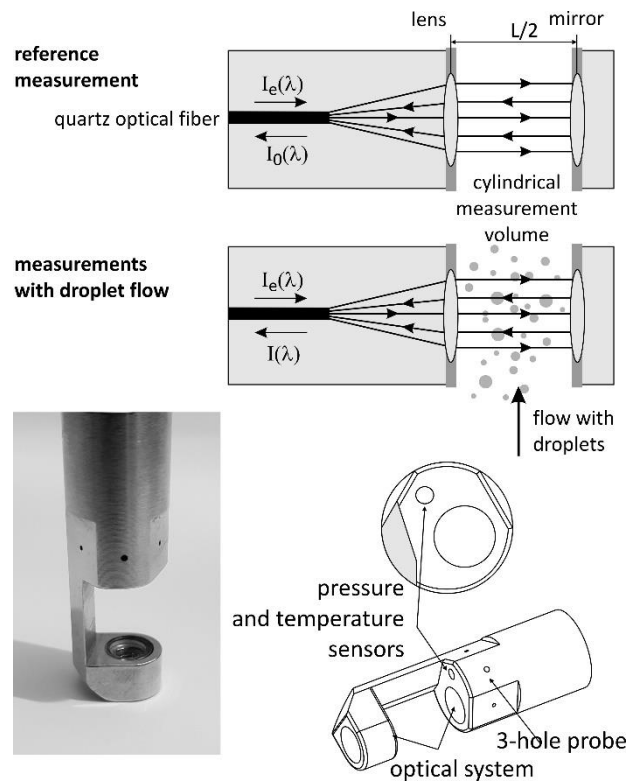
Fig. 2.6. The view of the NIOP-X probe (Determination of light extinction coefficient by measurement of reference intensity and attenuated intensity)

In this system, the external lens is mounted on the traverse structure, which is positioned entirely outside the flow channel of the steam tunnel. The light from the deuterium-halogen illuminator is first expanded by a quartz lens to create a measurement area with a diameter of approximately 7 mm. After passing through the measurement space, the light is focused by another lens on the

opposite side of the tunnel and directed through a fiber optic cable to the spectrometer. However, such a configuration does not guarantee the absence of disturbances in the flow field. Due to the large required external diameter of the probe (~15 mm), it is not exactly suitable for use in narrow channels of convergent-divergent nozzles, used in the tests presented in the thesis, but only in typical wide steam tunnels with a large mass flow of the medium. Such tunnels are, however, expensive to operate and difficult to use also in tests of the research method itself. For this purpose, the second type of measuring probe with an optical system placed outside the tunnel was mainly used. This made it easier to use this method also in flows through nozzle channels with smaller throat dimensions. It is also much easier to correctly calibrate the measurement system itself. Fig. 2.7 shows the X probe measurement system used in the SUT steam tunnel.

Fig. 2.7. View of the X probe measurement system during tests in the steam tunnel

Before starting the experimental tests and using them in numerical validation, the LEM system was calibrated under different test conditions and with an additional measurement system operating on the principle of laser diffraction. The system was tested in several different cases:

- tests for known particle diameters in the calibration chamber,

- comparative tests using LEM and laser diffraction (Sprytec) for known particle sizes in the calibration chamber,

- benchmarking of the calculation procedure itself for identical input data,

- comparative tests under real flow conditions using two different methods (LEM and laser diffraction methods).

Figures 2.8-2.11 present the measurement results from subsequent tests for selected particle diameters and measurement methods.

The results of static tests carried out in a specially constructed calibration chamber gave satisfactory results. The tests were performed for several diameters and numbers of particles (D $\cong$ 0.2; 0.5; 0.6; 0.8; 2 μm, N= ~$1.2e^{11}$ m^{-3}). Examples of results are shown in Fig. 2.8 for a diameter of 2 μm. For all cases, accuracies within the maximum deviations of ±6% for the particle diameter and ±12% for their number were achieved. The lower accuracy in determining the number of particles is mainly due to challenges in determining the actual number of reference particles for all diameters using the microscopic method.
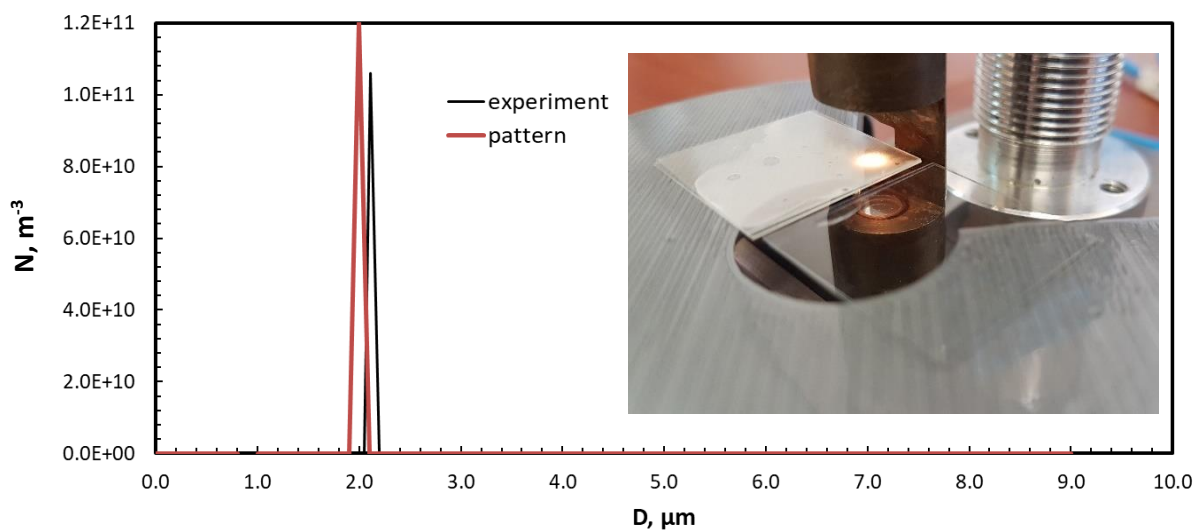
Fig. 2.8. Distribution of particle diameter and their number, view of X probe during tests

The second test method involved analyzing the results obtained using an in-house computational procedure. For this purpose, it was compared with another procedure using the same input data D=0.6 μm. The test was conducted in collaboration with Shanghai University, comparing the results of LEM KMiUE with a program developed by Prof. X. Cai's research group (Fig. 2.9). The tests showed a very good agreement between the computational procedures used in both cases. Both the numerical tests, performed using the prepared numerical input data and the real data obtained from the first type of tests in the calibration chamber for different types of particles, gave very satisfactory results. The accuracy of diameter D32=±0.3% and N=± 1.7% was achieved, confirming the correctness of the calculation method itself.
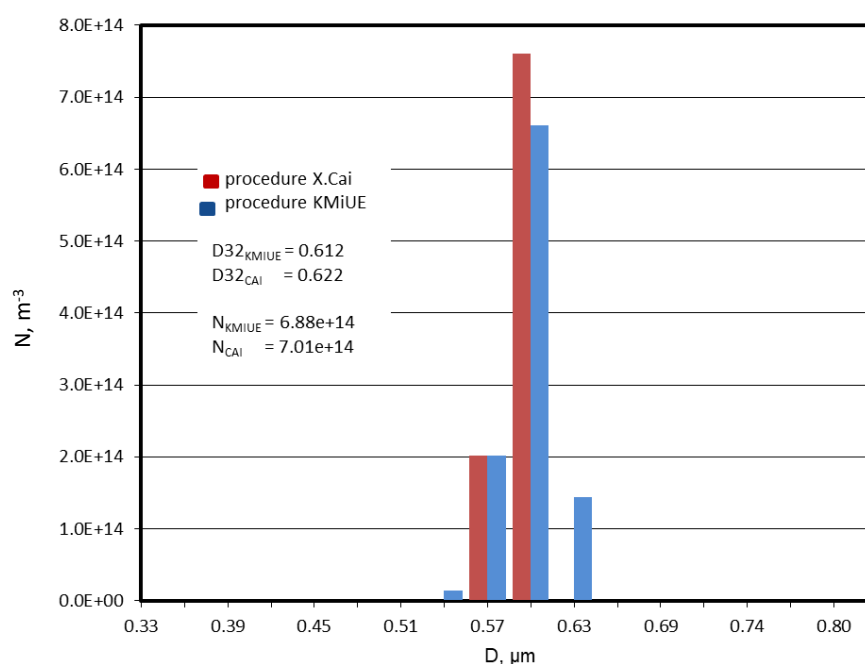
Fig. 2.9. Distribution of particle diameter and their number, comparing the results of LEM KMiUE with Prof. X. Cai's research group

From the perspective of the possibility of practical application, tests carried out in real wet steam flow conditions in a steam tunnel provide the most comprehensive evaluation of the measurement capabilities of the presented method. It is also valuable to combine and compare experimental measurements with advanced numerical fluid dynamics simulations conducted in parallel. Tests are typically performed under ideal conditions of calibration chambers, which are usually equipped with very thin glass walls of a well-known refractive index, as well as an ideal, contaminant-free, particle carrier medium. These conditions are difficult to achieve in real flow, and even more so in a steam tunnel with a large cross section. It is also difficult to

generate a flow with parameters similar to those of the steam flow, but with a precisely known particle size distribution. For this reason, additional comparative studies were conducted using a different measurement technique. Therefore, the commercial Sprytec measuring system by Malvern Panalytical (Fig. 2.10), which employs the laser diffraction method, was used. In contrast to the LEM method, the laser diffraction method uses one wavelength of light and determines the light scattering based on several angles of wave deflection after passing through the particles. However, this device offers a fairly large measuring range from 0.1 to 2000μm, and while the manufacturer declares 1% accuracy across the entire range, the accuracy of diameter determination decreases for smaller particles. For real flow comparison purposes, this method was the only available option. However, the laser diffraction method does not allow for determining the number of particles N but only provides volume distribution.
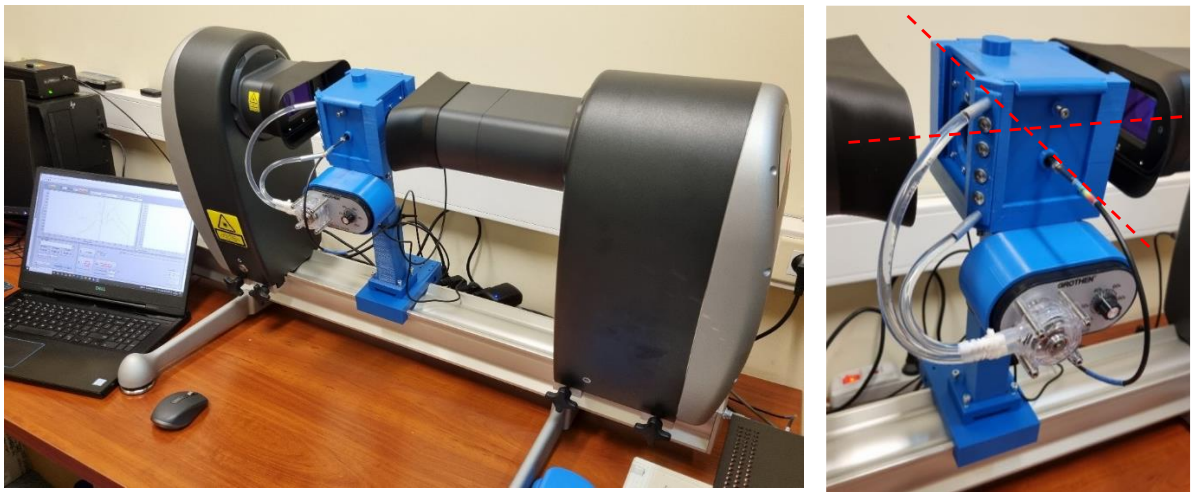
Fig. 2.10. The commercial Sprytec measuring system by Malvern Panalytical

Under the conditions of a specially constructed cross-calibration chamber (Fig. 2.10), both methods showed high agreement in their measurement capabilities. Figure 2.11 presents sample results for diameters of 0.5 and 0.8 μm. Tests conducted for several different diameters allowed for fine-tuning the corresponding correlations. Deviations in droplet diameter D32 did not exceed 3% when using identical input data.
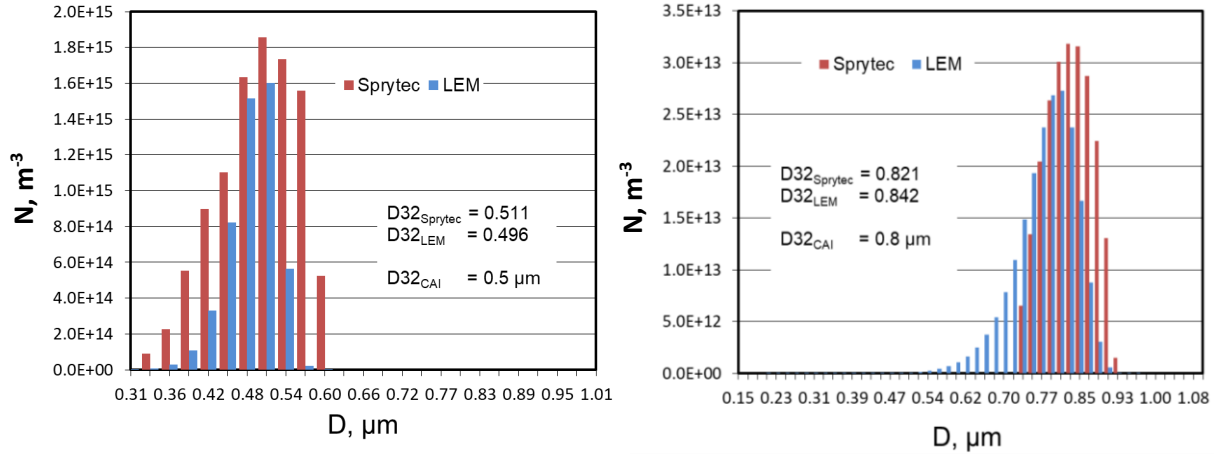
Fig. 2.11. Comparison between two methods of Sprytec and LEM for diameters of 0.5 and 0.8 μm

In the next phase, both methods were used to conduct tests under the flow conditions of moist air with known input parameters. In measurements carried out in the converging-diverging nozzle, good agreement between both methods was achieved (Fig. 2.12). The accuracy for the diameter was about ±10%. This level of accuracy was also adopted in the subsequent analysis and validation methods presented in this thesis.
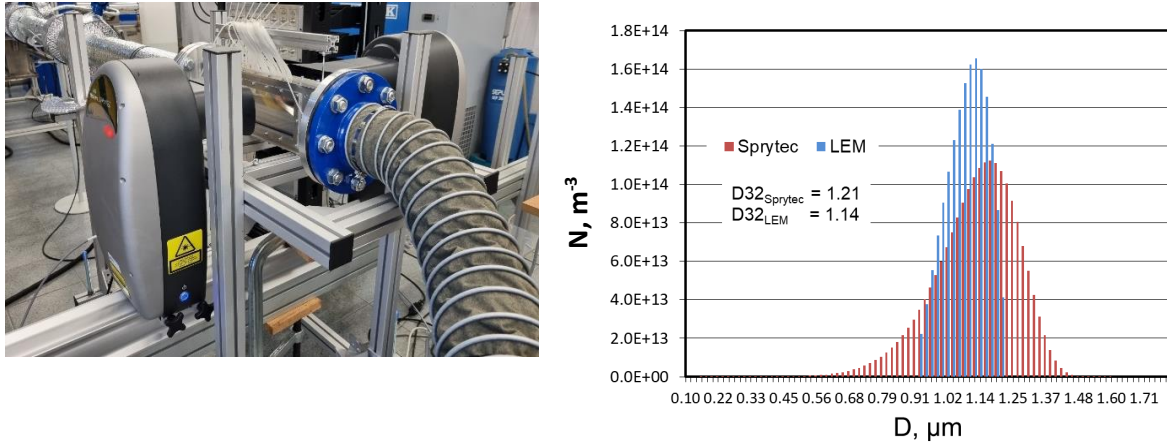
Fig. 2.12. Sprytec and LEM methods under moist air flow conditions

The difficulties and complex measurement issues of the LEM method were also confirmed, highlighting the need to calibrate the method in real flow conditions. This is particularly true for glass refractive indexes, glass wall angles and predicting the quality of the working medium. Slightly better results were obtained with the first method, using a NIOP-probe, mainly because it is not affected by the walls limiting the channel and is directly inserted into the flow with a

small optical geometry (~10 mm). However, this also had its bad effect, as the large diameter (~20mm) of the probe disturbed the flow. Therefore, in the subsequent studies, it was decided to use the second type of methods, with sensors and optics located outside the channel. This type of work was carried out in previous years and also as part of a project commissioned by the National Science Centre (NCN) concerning real gas effects identification in two-phase, transonic flows of wet steam, with the project number 2020/37/B/ST8/02369. Such a prepared and calibrated method was used to validate numerical methods both in nozzles and stator channels in the steam tunnel.

2.2.2. Methods of static pressure measurement

The measurement chamber was equipped with pulse tubes connected to high-speed pressure sensors. Data was collected using Honeywell 243PC15M high-speed pressure transducers. Each measurement series lasted 3 seconds, during which static pressure was recorded at a frequency of 400 Hz, resulting in 1200 data points per series. In order to remove condensed water from the system's impulse tubes, the pressure measuring lines are equipped with special automatic valves that allow for the temporary creation of a vacuum in the lines, which allows for the impulse tubes to be quickly emptied. After each series, the pressure tubes were purged to remove any potential influence of water droplets on the results, and a new set of measurements was taken. Typical nonlinearity and therefore also inaccuracy of the used transducers is quite large and amounts to >1kPa (1.5% FS), however, in the used measurement system, additional section calibration was applied using higher class calibrators. This allowed to obtain accuracy of <250Pa in the interesting from the point of view of measurement research perimeter [71].

2.2.3. Schlieren system visualisation

The general principle of visualization with this method is that the light beams, after leaving a point source, pass through an optical system consisting of lenses or mirrors that create a measurement space in which they are deflected by the density gradient, and then hit the edge of the knife, where the main light source is cut off. The remaining shadow of the observed phenomenon is registered as an image on the screen or camera.

Fig. 2.13 is a used configuration of a single-axis system, enabling the registration of flow phenomena occurring in nozzles and inter-blade channels, through the use of high-frequency illuminators and, accordingly, a short light pulse, as well as a camera with a higher frames per second. The measurement system constructed and used consists of:

• HardSoft IL-105/6X Illuminator with calibrated pinhole,

• two plano-convex lenses,

• knife with positioning system,

• fast camera Phantom Evo,

• optical bench.
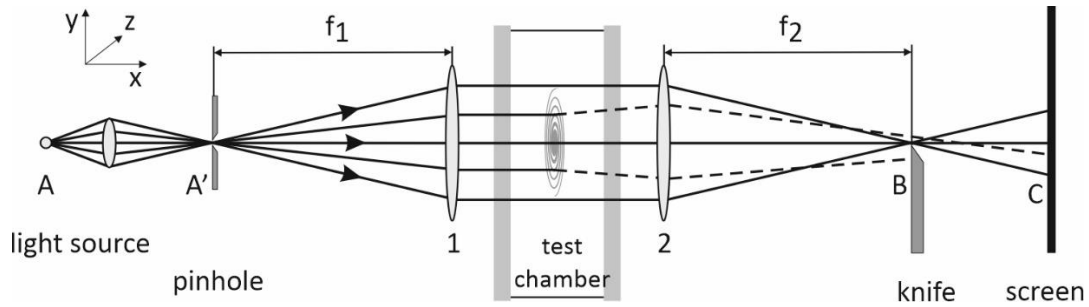
Fig. 2.13. Diagram of the configuration of the Schlieren system with one optical axis

2.3 Measurement results

The experimental results of wet steam flow are obtained from tests on the IWSEP nozzle and a linear blade cascade. Pressure measurements, flow visualization, and the LEM method are applied in different configurations depending on the type of analysis performed.

2.3.1. IWSEP nozzle

The first investigated geometry is the IWSEP nozzle which was proposed by Jörg Starzmann [19]. It is a converging-diverging nozzle with the expansion rate of $3000s^{-1}$ and the total throat height 40mm. The test section dimension is 1000x110x400mm (L*W*H). The measurement system consists of 40 pressure sensors, used to record static pressure distributions on both the top and bottom walls (Fig. 2.14). Measurements were taken at 10 mm intervals along the nozzle, starting from x = -0.06 m. In addition, the light extinction method (LEM) was employed to determine the droplet Sauter diameter (D_{32}) along the nozzle's centerline. Table 2.1 provides the obtained experimental data for two cases and Fig. 2.15 shows the nozzle profile shape. Fig. 2.16 and Fig. 2.17 show the measurement results of static pressure and droplet diameter for two cases, respectively. Figure 2.18 represents the Schlieren images of experiments.

Fig. 2.14. View of IWSEP nozzle in the test section
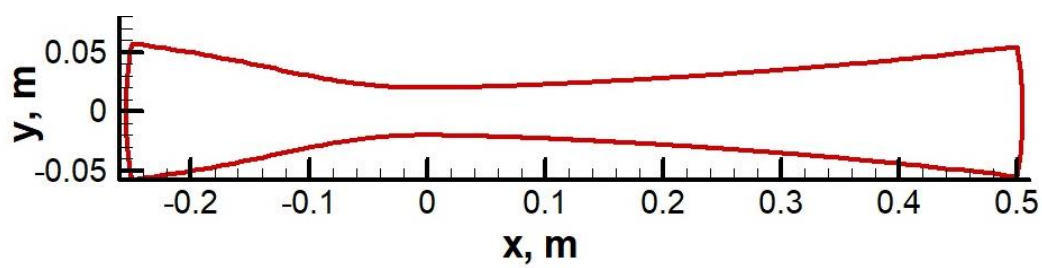
Fig. 2.15. IWSEP nozzle profile shape

Table 2.1. Experimental data

| x, m | Case 1 | | Case 2 | |
| | p₀=105.8 kPa, T₀=111.2 °C | | p₀=77.8 kPa, T₀=101 °C | |
	p, kPa	D_{32}, nm	p, kPa	D_{32}, nm
-0.06	82.36	---	---	---
-0.04	74.08	---	---	---
-0.02	65.28	---	---	---
0	56.16	---	43.51	---
0.01	52.77	---	40.46	---
0.02	51.20	---	38.42	---
0.03	51.87	---	39.34	---
0.04	54.90	---	44.15	---
0.05	53.42	---	41.21	---
0.06	49.42	---	38.35	---
0.07	47.05	---	35.98	---
0.08	44.12	---	33.99	---
0.09	42.42	---	32.48	---
0.1	39.47	---	30.83	---
0.11	37.43	---	29.38	---
0.12	35.28	---	27.98	---
0.13	33.85	---	26.82	---
0.14	33.20	---	25.50	---
0.15	32.11	---	24.47	350
0.16	30.53	---	23.42	---
0.17	29.03	---	22.43	---
0.18	28.22	---	21.64	---
0.19	27.14	---	20.74	---
0.2	26.13	183	---	370
0.21	25.15	---	---	---
0.22	24.07	---	---	---
0.23	23.02	---	---	---
0.24	22.71	---	---	---
0.25	21.88	194	---	385
0.26	20.56	---	---	---
0.27	19.56	---	---	---
0.28	19.29	---	---	---
0.29	18.53	---	---	---
0.3	18.05	196	---	---
0.31	17.03	---	---	---
0.32	16.51	---	---	---
0.33	15.58	---	---	---
0.34	15.12	---	---	---
0.35	15.05	---	---	---
0.36	14.52	---	---	---
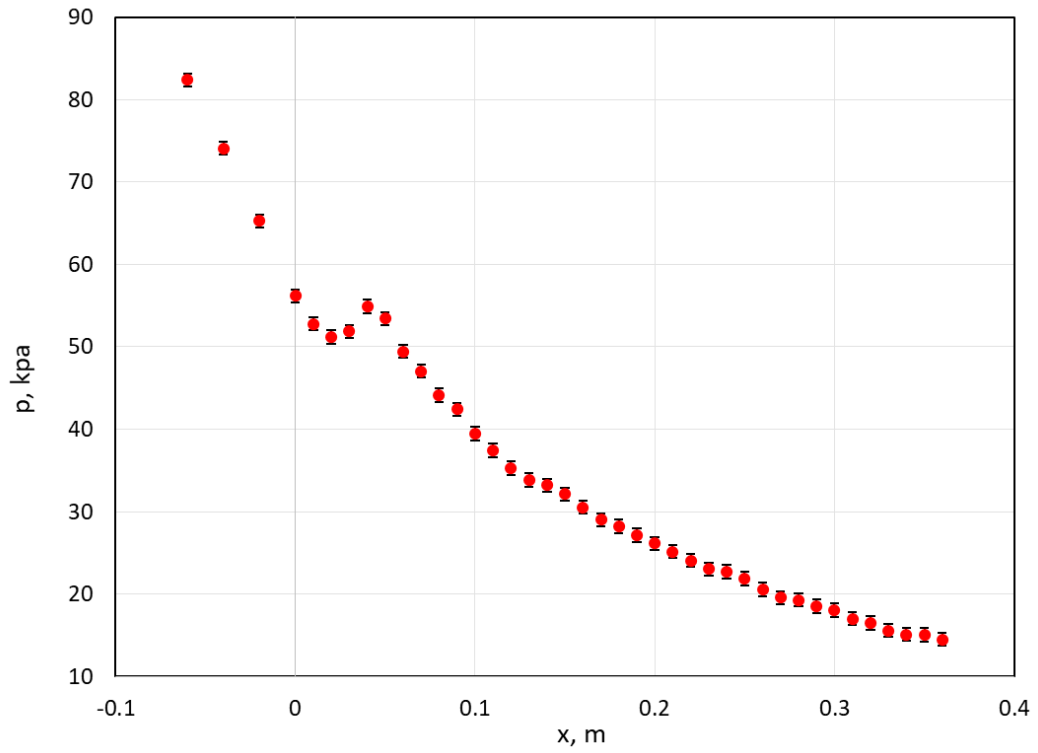
Case 1: p_0=105.8 kPa, T_0=111.2 ^{0}C
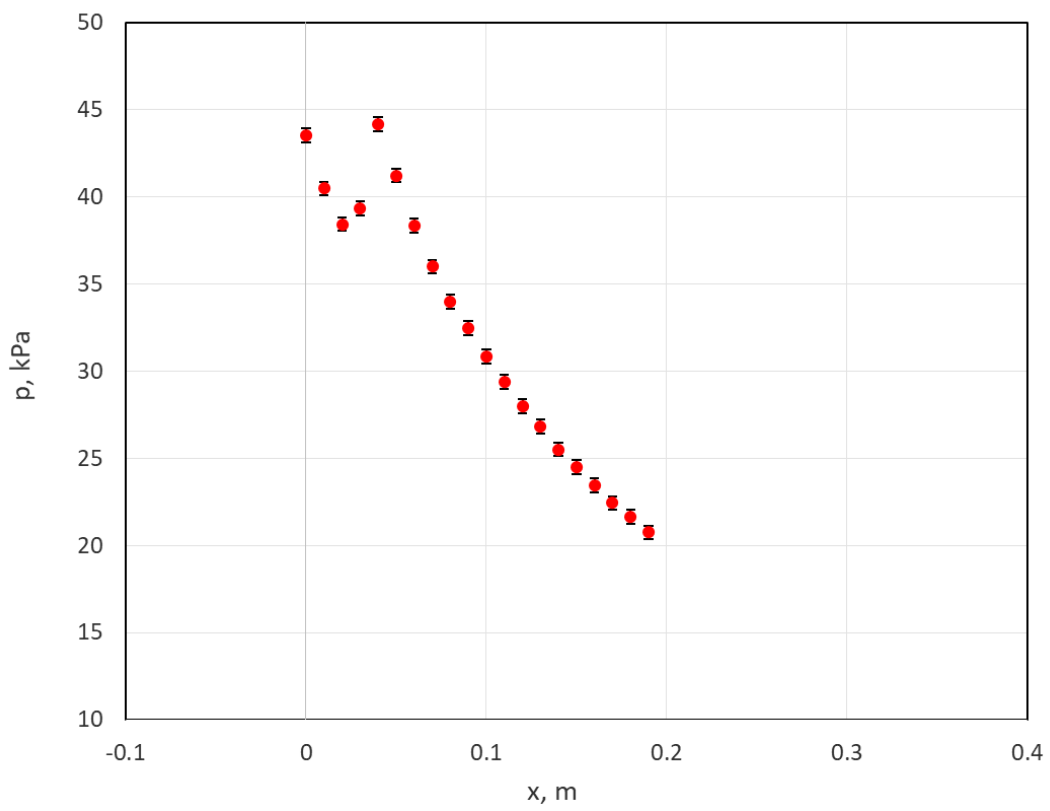
Case 2: p_0=77.8 kPa, T_0=101 ^{0}C

Fig. 2.16. Static pressure distribution along the IWSEP nozzle wall for cases 1 and 2
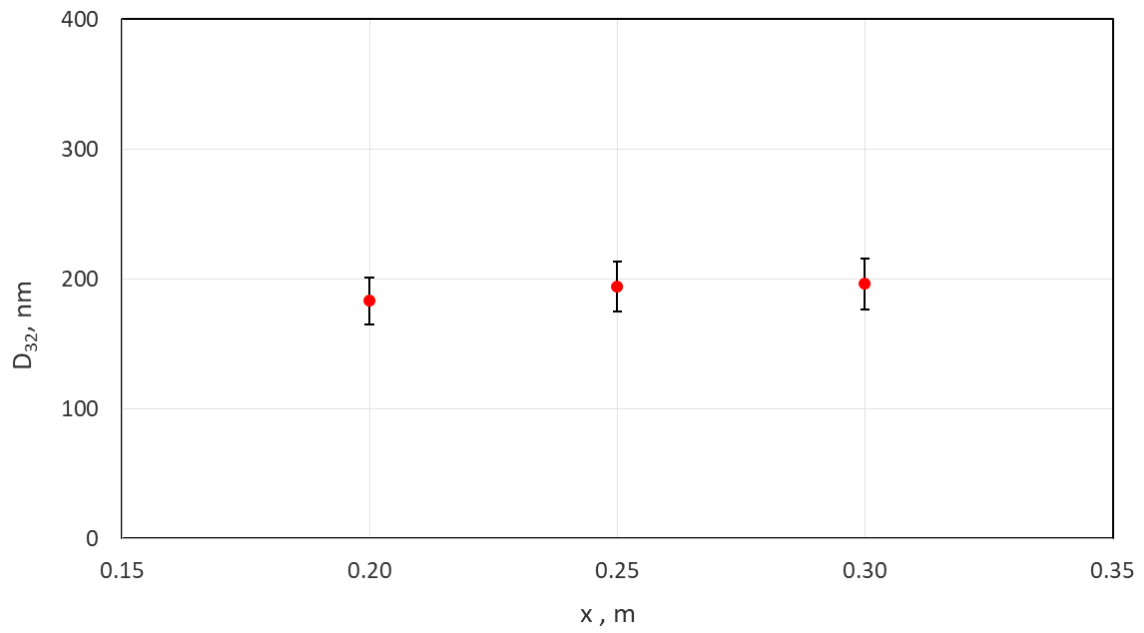
Case 1: p_0=105.8 kPa, T_0=111.2 ^{0}C
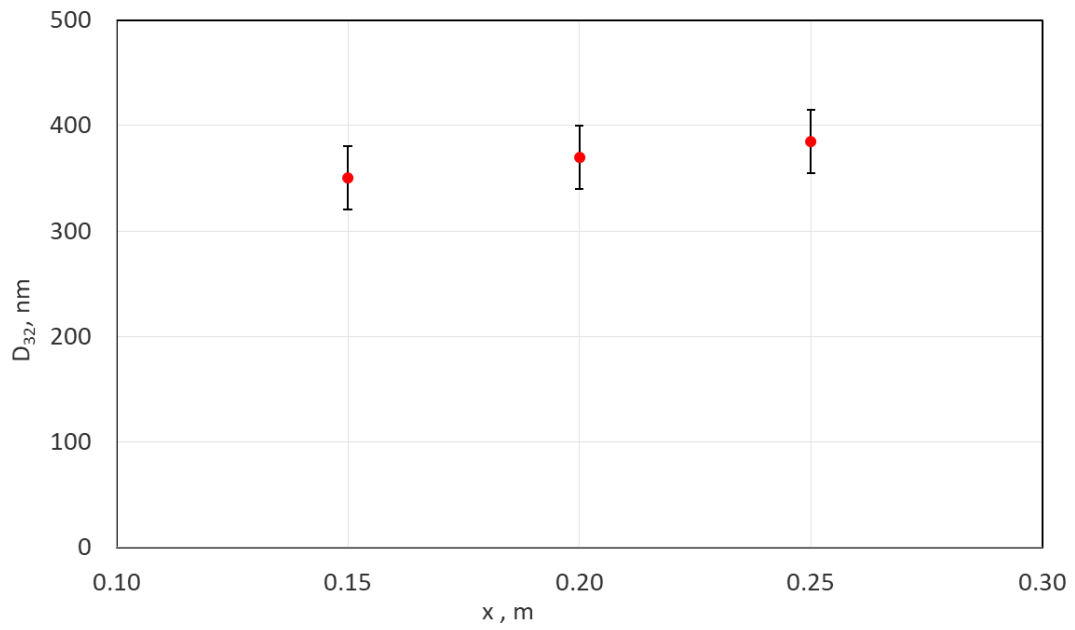
Case 2: p_0=77.8 kPa, T_0=101 ^{0}C

Fig. 2.17. Droplet diameter distribution through the nozzle midline for cases 1 and 2

Case 1: p_0=105.8 kPa, T_0=111.2 ^{0}C   Case 2: p_0=77.8 kPa, T_0=101 ^{0}C
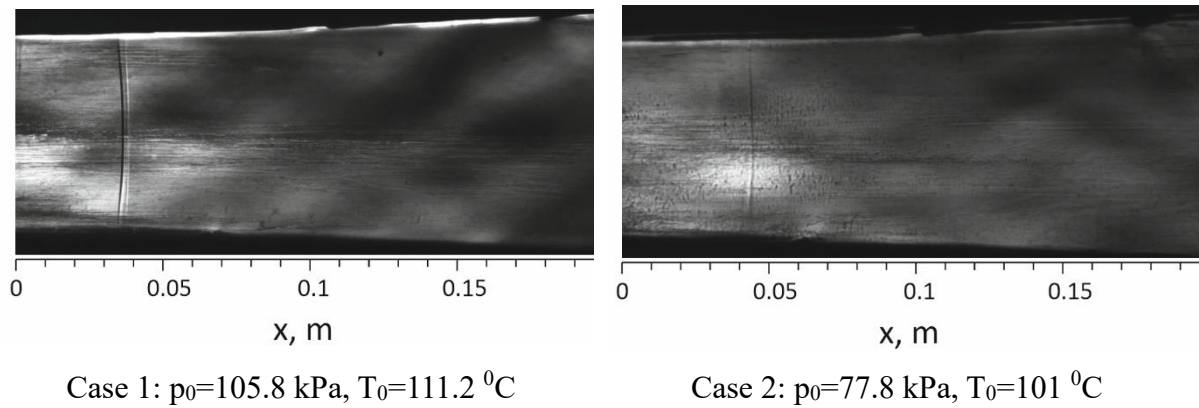
Fig. 2.18. Schlieren images of experiments for case 1 and 2

2.3.2. Linear stator cascade

The blade geometry chosen for this study is representative of the last stage stator in the low-pressure section of a real ~200 MW turbine. This specific geometry was selected to replicate the flow conditions and performance characteristics found in industrial turbines, making the results directly applicable to real-world scenarios.

The test section consists of four blades, creating three blade-to-blade channels (Fig. 2.19). This setup allows for a detailed examination of the flow dynamics within the blade passage, which is crucial for understanding losses, efficiency, and the overall behavior of the turbine under operating conditions.

The key dimensions of the cascade are as follows:

- Blade chord in axial direction: 173.97 mm

- Pitch: 91.74 mm

- Inflow angle: 0.0^o

- Test section width: 110 mm

For the blade-to-blade channel under investigation, 20 static pressure measurement points were placed on each blade to provide a comprehensive pressure profile along the blade surface. The positions of the pressure taps are shown in Fig. 2.20. The measurement results of static pressure on the stator blade for two cases, are presented in Fig. 2.21. Figure 2.22 shows the Schlieren images of experiments for two cases.

Fig. 2.19. Stator blade cascade in the SUT test rig and the measuring equipment
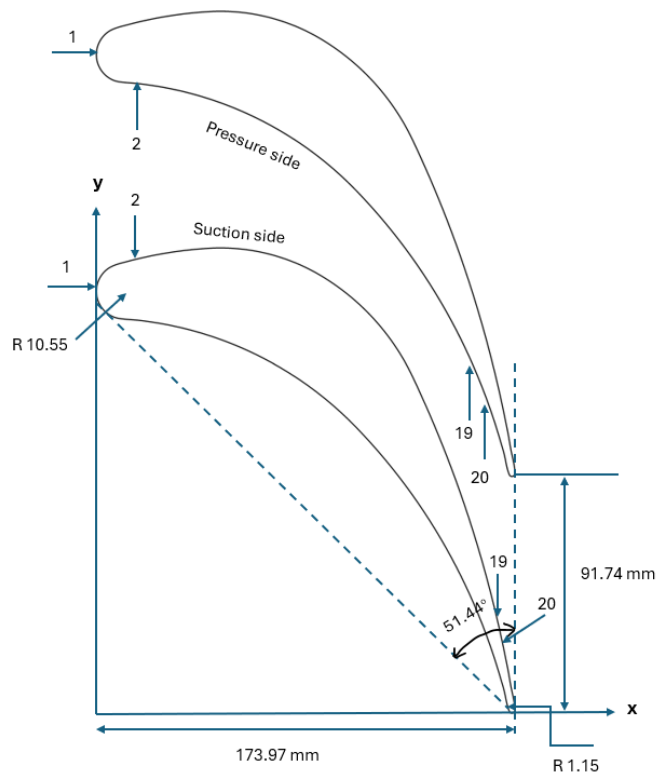
| No.	Pressure side		Suction side	
	x, mm	y, mm	x, mm	y, mm
1	0	143.45	0	143.45
2	14.10	132.95	14.47	156.15
3	28.30	132.30	30.55	160.71
4	42.38	130.19	47.36	163.46
5	56.16	126.65	64.59	162.75
6	69.52	121.72	81.21	158.12
7	82.28	115.45	96.36	150.05
8	94.35	107.91	109.68	139.29
9	105.63	99.14	120.74	126.24
10	116.23	89.50	129.50	111.89
11	126.24	79.17	137.49	97.34
12	135.57	68.23	144.97	82.50
13	140.01	62.51	148.52	74.95
14	144.22	56.70	151.91	67.40
15	148.25	50.76	155.19	59.74
16	152.05	44.76	158.29	52.10
17	155.66	38.65	161.28	44.37
18	159.08	32.43	164.10	36.66
19	162.36	26.00	166.80	28.85
20	165.45	19.41	169.36	20.99

Fig. 2.20. Positions of the pressure taps for investigated blade-to- blade channel
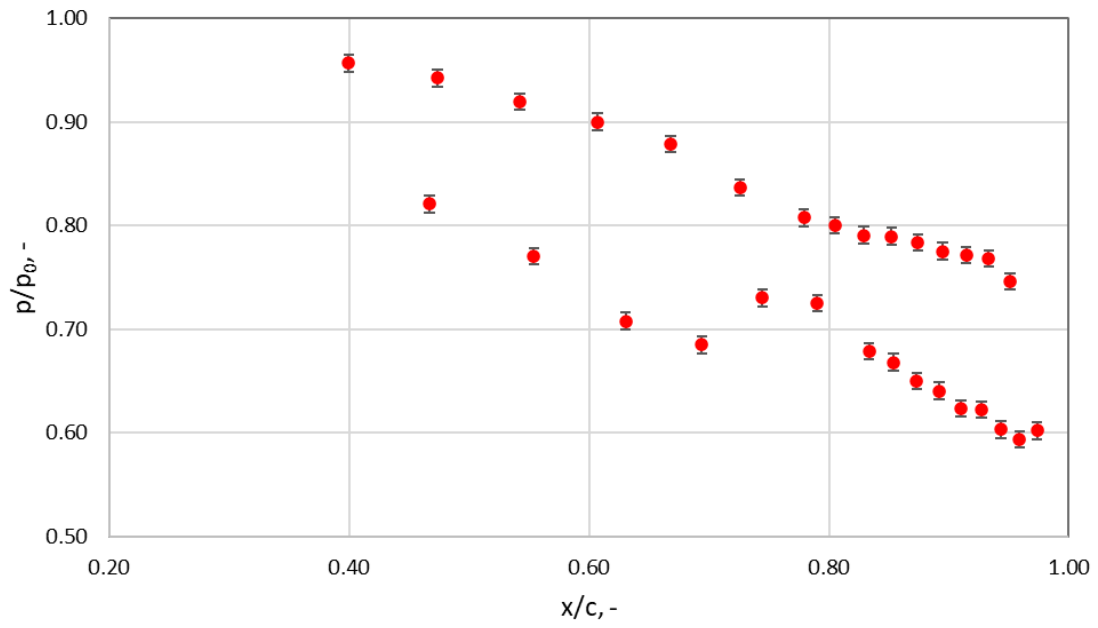
Case 1: p_0=105 kPa, T_0=95.85^{0}C, p_{out}=66 kPa
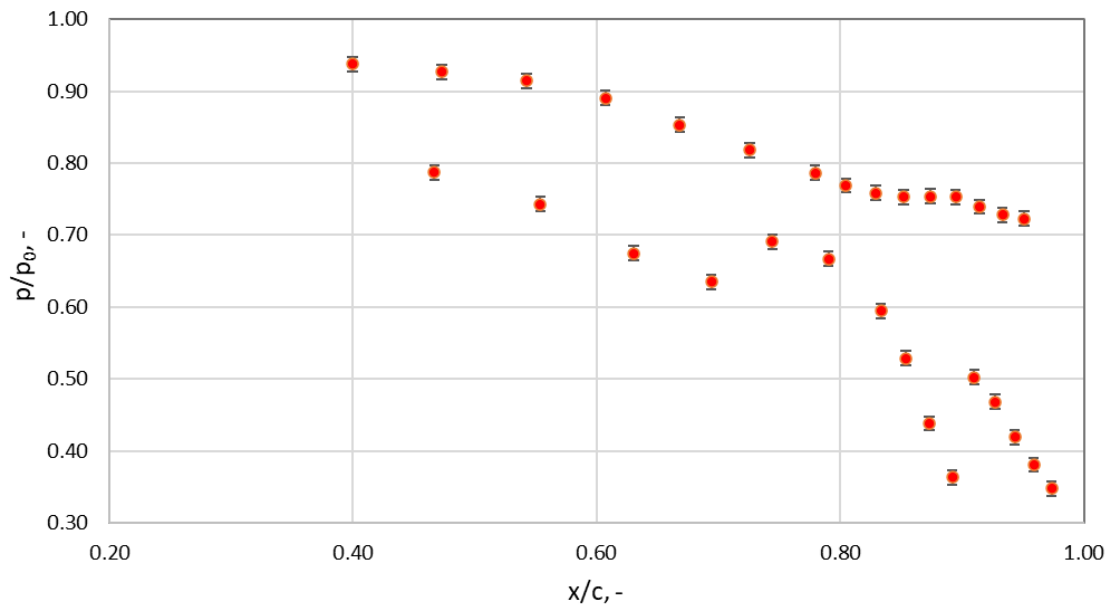
Case 2: p_0=103 kPa, T_0=105.85^{0}C, p_{out}=42 kPa

Fig. 2.21. Static pressure on the stator blade for cases 1 and 2

Case 1: p_0=105 kPa, T_0=95.85^{0}C, p_{out}=66 kPa   Case 2: p_0=103 kPa, T_0=105.85^{0}C, p_{out}=42 kPa
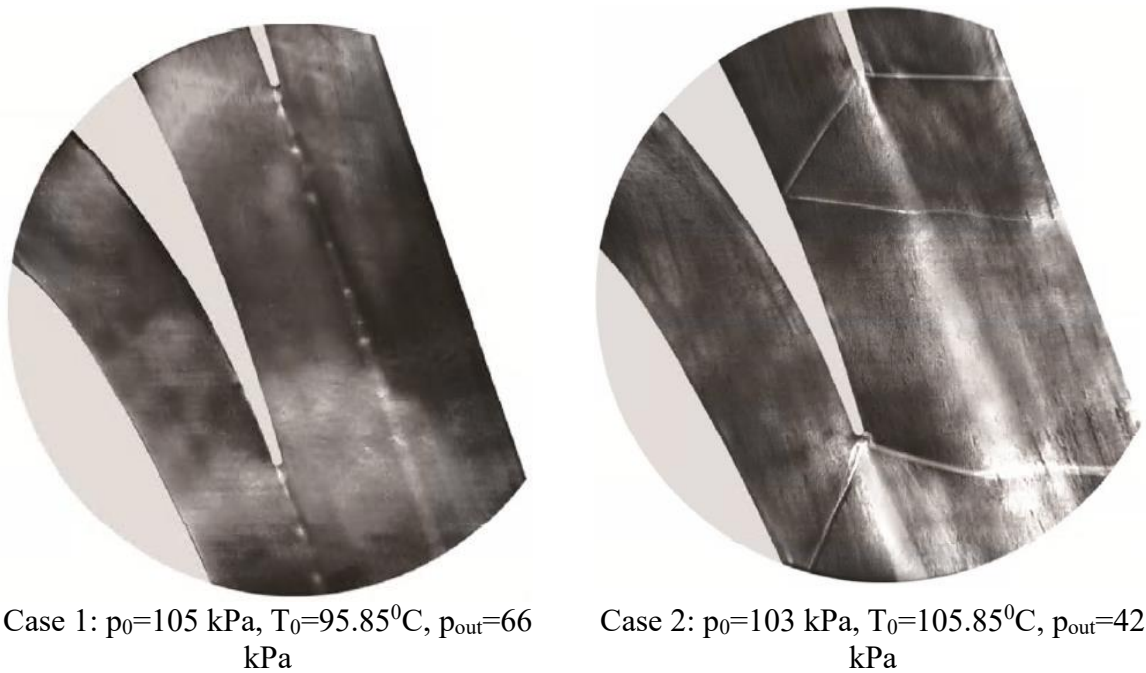
Fig. 2.22. Schlieren images of experiments for cases 1 and 2

2.3.3. Linear rotor cascade

The measurement chamber illustrated in Fig. 2.23 features rotor blades installed to replicate the tip rotor geometry of the last stage of a 200 MW turbine. This specific profile was selected to study the characteristics of the rotor at the critical tip region, where complex flow phenomena such as tip leakage and secondary flows occur. To facilitate precise static pressure measurements on the blade surface and to accommodate the blade cascade within the measuring chamber, the rotor profile was scaled up by a factor of 2.5 from its original size. The cascade consists of five blades, forming four blade-to-blade channels. The key dimensions of the cascade are as follows:

- Blade chord in the axial direction: 240.17 mm

- Pitch: 180 mm

- Inflow angle: 0.0°

- Test section width: 110 mm

In the blade-to-blade channel under study, fifteen static pressure measurement points were placed on each blade to capture the pressure distribution along the surface, as shown in Fig.

2.24. The measurement results of static pressure for two cases are shown in Fig. 2.25, and the Schlieren images of experiments for two cases are presented in Fig. 2.26.

Fig. 2.23. Rotor blade cascade in the SUT test rig and the measuring equipment
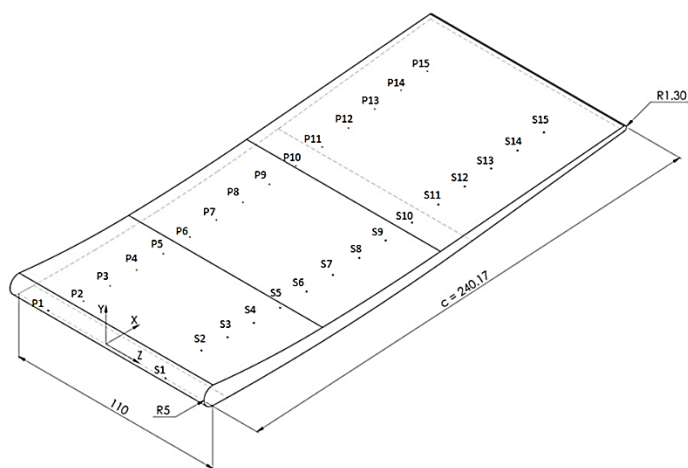
No.	Pressure side (P)		Suction side (S)	
	x, mm	y, mm	x, mm	y, mm
1	0	0	0	0
2	19.97	-5.32	20.36	3.52
3	35.06	-5.34	35.22	2.58
4	50.14	-5.13	50.11	2.13
5	65.22	-4.70	65.02	2.17
6	80.28	-4.04	79.99	2.61
7	95.34	-3.15	94.96	3.27
8	110.37	-2.03	109.92	4.15
9	125.39	0.69	124.86	5.25
10	140.38	0.88	139.80	6.57
11	155.34	2.66	154.77	7.94
12	170.26	4.52	169.74	9.31
13	185.17	6.37	184.70	10.68
14	200.09	8.22	199.67	12.05
15	215.00	10.07	214.64	13.43

Fig. 2.24. Positions of the pressure taps for investigated blade-to-blade channel
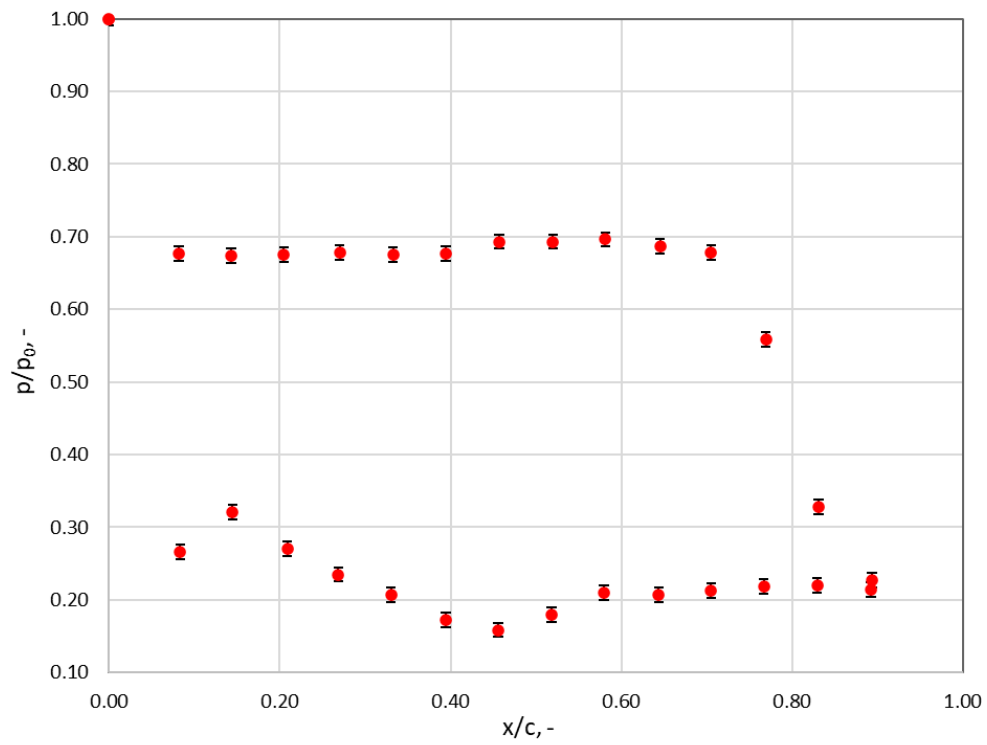
Case 1: p_0=57.5 kPa, T_0=87.5 ^{0}C, p_{out}=11 kPa
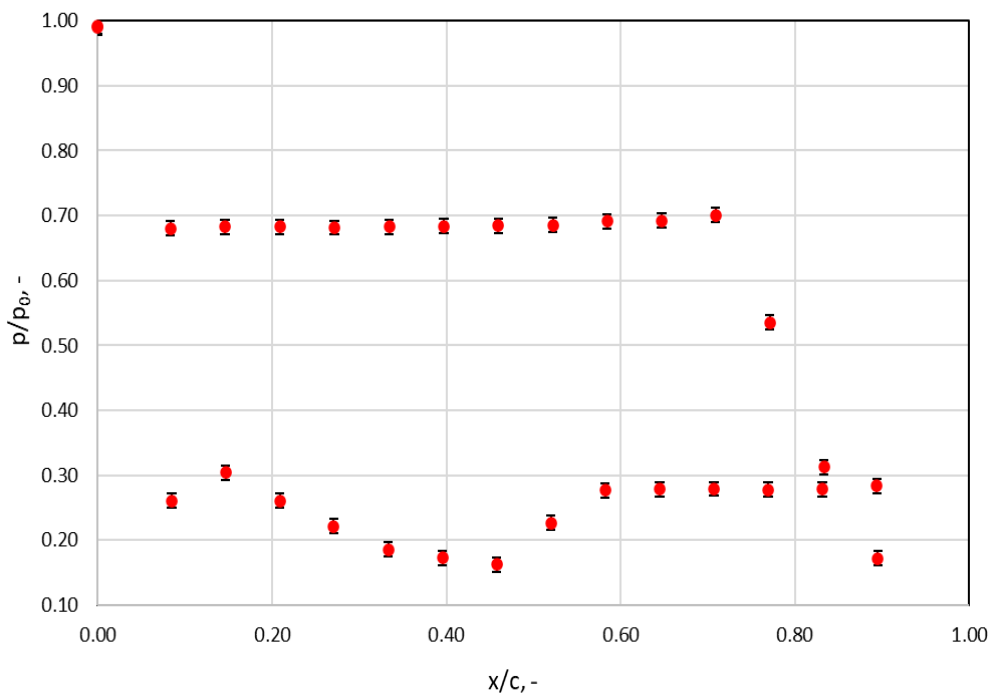
Case 2: p_0=65 kPa, T_0=130.5 ^{0}C, p_{out}=14 kPa

Fig. 2.25. Static pressure on the rotor blade for cases 1 and 2
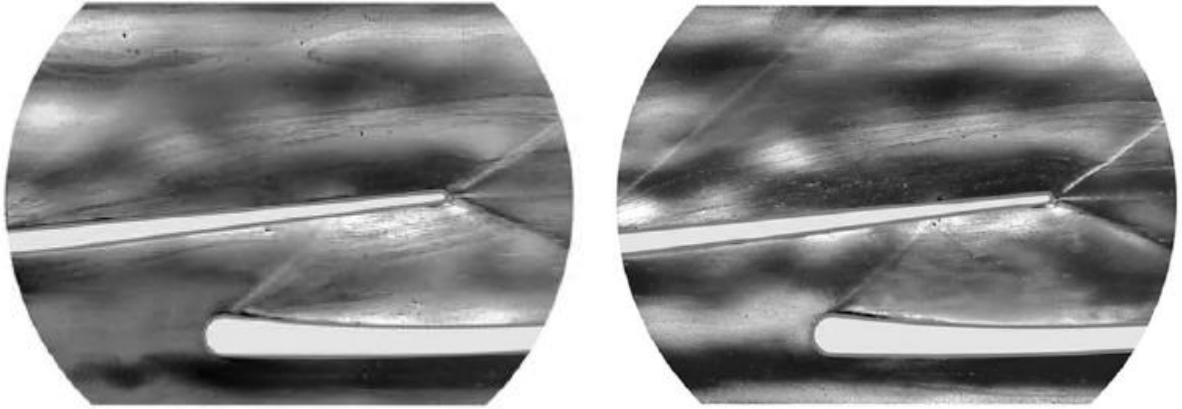
Case 1: p_0=57.5 kPa, T_0=87.5 ^{0}C, p_{out}=11 kPa   Case 2: p_0=65 kPa, T_0=130.5 ^{0}C, p_{out}=14 kPa

Fig. 2.26. Schlieren images of experiments for cases 1 and 2

3. Searching for the Proper CFD Simulation Tools

As discussed in Chapter 1, although various studies have been conducted on the numerical analysis of wet steam flow, a significant lack of agreement remains among many of them, highlighting the need for further investigation. One of the key challenges in this area is the absence of a universally optimal numerical method for all cases. While some approaches have shown reasonable agreement with experimental data, noticeable discrepancies persist across different studies [72, 73]. These inconsistencies primarily arise from variations in condensation models, their specific implementations, and the characteristics of the numerical solvers employed.

The substantial differences observed in existing research emphasize the importance of evaluating and comparing different numerical methods at the initial stage of each new study, as the specific conditions of each case play a crucial role in determining the most suitable approach. In particular, nucleation and droplet growth models, along with the equation of state, play a crucial role in the accuracy of predictions. Therefore, selecting an appropriate condensation model and equation of state for the case under consideration is a key step in the research process. The aim of this chapter is to simulate wet steam flows, with the objective of identifying the most appropriate computational fluid dynamics (CFD) tools for accurately predicting such flows. Using the options and capabilities within CFD software, multiple models are developed and applied to simulate the flow behavior in both a Laval nozzle and a linear rotor cascade. Ultimately, to determine the optimal model, the outcomes of these simulations are evaluated and compared against in-house experimental data for validation. Precisely simulating wet steam flows is essential for gaining detailed insights into the thermodynamic behavior of these flows. This valuable information can then be applied to the design and optimization of highly efficient steam turbine stages.

3.1 Numerical model and governing equations

While in-house academic codes [13-18] demonstrate strong simulation capabilities and potential for further development, their institution-specific nature limits their general applicability. Therefore, this chapter aims to examine commercially available codes that are widely accessible and applicable. Among these, ANSYS CFX and ANSYS Fluent are the most widely used commercial solvers in research and are extensively employed in industrial applications. In the following sections, the wet steam flow is simulated using ANSYS Fluent

and ANSYS CFX software, and the governing equations are explained in detail. For modelling wet steam two-phase flow in ANSYS Fluent, there are two options available:

- Activate the built-in Wet Steam Model: The first method is to enable the wet steam flow model that is available within the software. This model is pre-configured to simulate the behaviour of wet steam, including phase transitions between vapor and liquid.
- Use UDFs (User-Defined Functions): The second method involves disabling the built-in wet steam model and using in-house UDFs to define specific behaviours and interactions for the wet steam flow. This approach offers greater flexibility but requires more advanced user input and customization.

In the following sections, seven test cases are generated using the available tools within the software. The primary distinction among these cases lies in the selection of condensation models and equations of state. Cases 1 and 2 are simulated using the built-in Wet Steam Model in ANSYS Fluent. Cases 3, 4, and 5 utilize in-house UDFs within ANSYS Fluent. Meanwhile, cases 6 and 7 are modeled using ANSYS CFX.

3.1.1. Built-in Wet Steam Model

In this model, the conservation equations (RANS equations) are formulated for the mixture.

Mass conservation equation:

The conservation of mass in wet steam flow is governed by the continuity equation, which in differential form is written as:

$$\frac{\partial}{\partial t} \rho_m + \nabla . (\rho_m \vec{u}) = 0 \tag{3.1}$$

Here, ρ_m denotes the mixture density, which accounts for the presence of both vapor and liquid phases in the flow. In wet steam conditions, this density varies not only due to changes in pressure and temperature, but also as a result of phase change processes such as condensation or evaporation. The mixture density can be expressed as:

$$\rho_m = (1 - \alpha) . \rho_v + \alpha . \rho_l \tag{3.2}$$

This equation (eq. 3.1) states that the rate of change of mass inside a control volume is exactly balanced by the net mass flux across its boundaries. In other words, the increase or decrease of mass in a given region is solely due to mass entering or leaving that region, ensuring that no

mass is lost or created in the system. Even though wet steam involves complex two-phase interactions, the continuity equation remains valid as long as ρ_m properly reflects the local composition of the flow. Phase changes are implicitly captured in the spatial and temporal variations of ρ_m.

Momentum conservation equation:

The conservation of momentum for wet steam flow is described by the Navier–Stokes equation in its compressible form:

$$\frac{\partial}{\partial t}\rho_m\vec{u} + \nabla.(\rho_m\vec{u}\vec{u}) = -\nabla p + \nabla.\tau \tag{3.3}$$

This equation states that the rate of change of momentum in a control volume is equal to the net force acting on it. The left-hand side represents the temporal and convective changes in momentum, while the right-hand side accounts for pressure forces and viscous stresses.

Energy conservation equation:

The energy conservation equation governs the thermal behavior of wet steam flow and is given by:

$$\frac{\partial}{\partial t}\rho_m E_m + \nabla.(\rho_m\vec{u}E_m) = -\nabla.(\vec{u}p) + \nabla.(\vec{u}\tau) + \nabla.(\lambda_m\nabla T_m) \tag{3.4}$$

This equation describes the first law of thermodynamics for a moving control volume: the rate of change of energy is equal to the net work and heat transfer to the system. The energy conservation equation for wet steam flow states that the rate of energy change within the fluid and its transport by convection (left-hand side terms) is balanced by the effects of pressure work, viscous work, and heat conduction (right-hand side terms).

In wet steam, all terms are evaluated using mixture-averaged properties. The specific energy E_m includes both internal and kinetic energy, as follows. Effects of phase change, such as condensation, influence e_m through the release or absorption of latent heat, and are implicitly captured in the energy balance.

$$E_m = e_m + \frac{u^2}{2} = h_m - \frac{p}{\rho_m} + \frac{u^2}{2} \tag{3.5}$$

To model wet steam, two additional transport equations are needed. The first transport equation governs the mass fraction of the condensed liquid phase (y):

$$\frac{\partial}{\partial t}\rho_m y + \nabla.\,(\rho_m \vec{u} y) = \Gamma \tag{3.6}$$

where Γ is the mass generation rate due to condensation and evaporation (kg per unit volume per second).

$$\Gamma = \frac{4}{3}\pi\rho_l r^{*3} J + 4\pi\rho_l N r^2 \frac{dr}{dt} \tag{3.7}$$

The second transport equation models the evolution of the number of the droplets per unit volume (N):

$$\frac{\partial}{\partial t}\rho_m N + \nabla.\,(\rho_m \vec{u} N) = \rho_m J \tag{3.8}$$

where J is the nucleation rate (number of new droplets per unit volume per second), and calculated using the classical nucleation theory [27].

$$J = \frac{\alpha_c}{1+C}\sqrt{\frac{2\sigma}{\pi m_v^3}\frac{\rho_v^2}{\rho_l}}\exp\left(-\frac{4\pi\beta_c r^{*2}\sigma}{3k_B T_v}\right) \tag{3.9}$$

C is the non-isothermal correction factor, which was proposed by Kantrowitz [26] in order to consider the temperature difference between the two phases:

$$C = 2\frac{\gamma_v - 1}{\gamma_v + 1}\frac{L}{RT_v}\left(\frac{L}{RT_v} - 0.5\right) \tag{3.10}$$

α_c, β_c are the condensation coefficient and an empirical correction factor:

$$\alpha_c = 1, \beta_c = 1$$

It is also important to estimate the droplet growth rate ($\frac{dr}{dt}$), as after nucleation process, the existed nuclei tend to growth. The following equation is the general form of droplet growth rate.

$$\frac{dr}{dt} = f(Kn)\frac{\lambda_v}{r}\frac{1}{\rho_l}\left(1 - \frac{r^*}{r}\right)\left(\frac{RT_v^2}{L^2}\right)ln\left(\frac{p_v}{p_s(T_v)}\right) \tag{3.11}$$

Several researchers like Gyarmathy [33], Fuchs-Sutugin [74], and Young [31] proposed their own correction functions ($f(Kn)$). These models are suitable for a wide range of droplet growth behaviors by utilizing the Knudsen number in their formulations. However, in ANSYS Fluent using built-in Wet Steam Model, only the Young droplet growth model is available, which is as follows:

$$f(Kn)_{YO} = \frac{1}{\frac{1}{1 + 2\beta_{Yo}Kn} + 3.78(1 - v)\frac{Kn}{Pr}} \tag{3.12}$$

$$v = \frac{RT_s}{L}\left(\alpha_{Yo} - 0.5 - \left(\frac{2 - q_{Yo}}{2q_{Yo}}\right)\left(\frac{\gamma_v + 1}{2\gamma_v}\right)\left(\frac{C_{pv}T_s}{L}\right)\right) \tag{3.13}$$

q_{Yo} is Young condensation coefficient, α_{Yo} and β_{Yo} are two modelling parameters:

$$q_{Yo}=1,\ \alpha_{Yo}=9,\ \beta_{Yo}=0$$

In ANSYS Fluent using built-in Wet Steam Model, for estimating the thermodynamic properties of the phases, there are the Virial equations developed by Vukalovich and the other by Young. For case 1 Vukalovich equation of state and for case 2 Young equation of state is used:

For case 1, Vukalovich: $p = \rho_v RT_v(1 + B\rho_v + C\rho_v^2 + D\rho_v^3)$

$$\tag{3.14}$$

For case 2, Young: $p = \rho_v RT_v(1 + B\rho_v + C\rho_v^2)$ $\qquad$ (3.15)

Where B, C and D are the second, third and fourth virial coefficients, which depend only on temperature.

3.1.2. Wet steam model using in-house UDFs

In case of using UDFs in ANSYS Fluent, the conservation equations are written specifically for the vapor phase, with the effects of the liquid phase accounted for through a source term in the energy conservation equation.

Mass conservation equation:

$$\frac{\partial}{\partial t}\rho_v + \nabla.(\rho_v \vec{u}) = 0 \tag{3.16}$$

Momentum conservation equation:

$$\frac{\partial}{\partial t}\rho_v \vec{u} + \nabla.(\rho_v \vec{u}\vec{u}) = -\nabla p + \nabla.\tau \tag{3.17}$$

Energy conservation equation:

$$\frac{\partial}{\partial t}\rho_v E_v + \nabla.(\rho_v \vec{u} E_v) = -\nabla.(\vec{u}p) + \nabla.(\vec{u}\tau) + \nabla.(\lambda_v \nabla T_v) + S_E \tag{3.18}$$

$$E_v = h_v - \frac{p}{\rho_v} + \frac{u^2}{2} \tag{3.19}$$

$$S_E = \left(\frac{4}{3}\pi\rho_l r^{*3}J + 4\pi\rho_l N r^2 \frac{dr}{dt}\right).L \tag{3.20}$$

In these cases, the two transport equations (eq. (3.6) and (3.8)) are used. For calculating nucleation rate, the classical nucleation theory is employed (eq. (3.9)). For the droplet growth rate, the general form (eq. (3.11)) is used and the Gyarmathy [33], Fuchs-Sutugin [74] , and Young [31] correction functions ($f(Kn)$) are applied:

For case 3, Gyarmathy model: $f(Kn)_{GY} = \frac{1}{1+3.18Kn}$ $\qquad$ (3.21)

For case 4, Fuchs-Sutugin model: $f(Kn)_{FS} = \frac{1+2.0Kn}{1+3.42Kn+5.32Kn^2}$ $\qquad$ (3.22)

For case 5, Young model: $f(Kn)_{YO} = \frac{1}{\frac{1}{1+2\beta_{YO}Kn}+3.78(1-\nu)\frac{Kn}{Pr}}$ $\qquad$ (3.23)

In these cases, for estimating wet steam thermodynamic properties, the NIST [43] real gas models are employed. To assess the thermodynamic and transport characteristics of around 125 fluids, the NIST real gas models employ REFPROP v9.1 database. When one of the NIST real gas models is enabled, the solver dynamically loads the REFPROP - shared library.

3.1.3. Wet steam model within ANSYS CFX

In ANSYS CFX, the conservation equations are written and solved separately for each phase. The continuous phase is the vapour, and the dispersed phase is tiny liquid droplets.

Mass conservation equations for vapor and liquid phases:

$$\frac{\partial(1-\alpha_l)\rho_v}{\partial t} + \nabla.\left((1-\alpha_l)\rho_v\vec{u}\right) = -\rho_l\frac{3\alpha_l}{r}\frac{dr}{dt} - (1-\alpha_l)m_lJ \tag{3.24}$$

$$\frac{\partial\alpha_l\rho_l}{\partial t} + \nabla.(\alpha_l\rho_l\vec{u}) = \rho_l\frac{3\alpha_l}{r}\frac{dr}{dt} + \alpha_l m_lJ \tag{3.25}$$

However, since equal velocity is assumed for both phases, a single momentum conservation equation is utilized for both:

$$\frac{\partial}{\partial t}\rho_m\vec{u} + \nabla.(\rho_m\vec{u}\vec{u}) = -\nabla p + \nabla.\tau \tag{3.26}$$

Energy conservation equations for vapor and liquid phases:

$$\frac{\partial(1-\alpha_l)\rho_vH_v}{\partial t} - (1-\alpha_l)\frac{\partial p}{\partial t} + \nabla.\left((1-\alpha_l)\rho_v\vec{u}H_v\right)$$
$$= \nabla.\left((1-\alpha_l)\lambda_v\nabla T_v\right) + S_H \tag{3.27}$$

$$\frac{\partial\alpha_l\rho_lH_l}{\partial t} - \alpha_l\frac{\partial p}{\partial t} + \nabla.(\alpha_l\rho_l\vec{u}H_l) = \nabla.(\alpha_l\lambda_l\nabla T_l) - S_H \tag{3.28}$$

$$S_H = -\left(\rho_l\frac{3\alpha_l}{r}\frac{dr}{dt}\right)H_u + \frac{3\alpha_l}{r}Q \tag{3.29}$$

Where α_l is the liquid volume fraction. H_u is upwinded total enthalpy, and Q is heat transfer between the phases [42].

In these cases, one transport equation is employed to determine the number of droplets:

$$\frac{\partial\rho_lN}{\partial t} + \nabla.(\rho_l\vec{u}N) = (1-\alpha_l)\rho_lJ \tag{3.30}$$

For calculating nucleation rate, the classical nucleation theory is employed (eq. (3.9)). In ANSYS CFX, for estimating the droplet growth rate, Gyarmathy (eq. (3.21)) and Young (eq. (3.23)) correction functions are available. In case 6 the Gyarmathy, and in case 7 Young correction function is applied. In these cases, IAPWS-IF97 formulations are used for calculating the thermodynamic properties of wet steam [42]. These tabular data are available in ANSYS CFX and very popular among researchers for estimation of wet steam properties.

3.2 Numerical Method

Selecting an appropriate numerical method is the first and most crucial step in simulation. Various software programs are available for simulating wet steam flows. In this study, we use ANSYS Fluent and ANSYS CFX. These software packages offer a variety of CFD tools and options for simulation, which can differ depending on the specific problem. Each problem, based on its physical and thermodynamic conditions, utilizes different tools. In this research, seven cases are created by using and combining these options. The most notable distinction between the cases lies in the use of different droplet growth models and EOS. The cases are visible in Table 3.1. Ultimately, by comparing them with our in-house experimental results, the selected cases, that can be used for simulating wet steam flows in the continuation of the project, will be presented.

Table 3.1. Different cases used in the current study to model wet steam flows

Case	Droplet growth model	Thermodynamic properties	Abbreviation
1	Young	Vukalovich EOS	Yo-Vu
2	Young	Young EOS	Yo-Yo
3	Gyarmathy	NIST real gas models	Gy-NIST
4	Fuch-Sutugin	NIST real gas models	FS-NIST
5	Young	NIST real gas models	Yo-NIST
6	Gyarmathy	IAPWS-IF97	Gy-IAPWS
7	Young	IAPWS-IF97	Yo-IAPWS

These software packages utilize the Finite Volume Method (FVM) to solve fluid flow equations. FVM is a widely used numerical technique in CFD. In this method, the governing partial differential equations (PDEs) of physical phenomena are transformed into algebraic equations, which are then solved over discrete control volumes. In this study, the implicit method is used to solve PDEs. In the implicit approach, variable values at future time steps are computed implicitly, meaning that the effects of the future time step are considered during the calculations. This requires solving a set of simultaneous equations, typically involving a system of linear equations. The implicit method is generally more stable than the explicit method because it accounts for future effects in the computations. However, each time step demands more computation due to the need to solve the system of equations, making the process more time-consuming. This method is well-suited for complex problems and simulations requiring high accuracy or long-term simulations.

The RANS (Reynolds Averaged Navier Stokes) equations, transport equations and two equations of the k-ω SST model form the set of PDEs for this study. In this study, the RANS equations are used to model the wet steam flow. The primary reason for this choice is the extremely high computational cost of solving the full Navier–Stokes equations directly (DNS) in complex and turbulent flows, such as those occurring in nozzles and blade passages. The RANS approach, by applying time-averaging, allows for the simulation of the mean flow behavior while accounting for the effects of turbulence through appropriate turbulence models. This method provides a practical balance between physical accuracy and computational efficiency, making it well-suited for industrial and thermal engineering applications.

The following assumptions are utilized to form and simplify the flow governing equations:

- Numerical simulation of two-phase flow, the continuous phase (steam) and dispersed phase (tiny liquid droplets)

- The flow is characterized by steady-state, compressible, turbulent, and viscous behavior.

- Slip velocity between liquid and vapor phases are neglected, implying equal velocities for both phases. In wet steam flows in the last stages of a steam turbine, due to the high flow velocity (supersonic flow) and the low mass fraction of the liquid phase compared to the steam, the velocity difference between the phases is negligible and can be ignored.

- The mixture pressure is considered equal to the steam phase pressure.

- The turbine blades are assumed to possess a smooth surface.

- No heat exchange occurs between the computational volume and its surroundings.

- Interactions among droplets are ignored.

- The condensation is homogeneous (that is, no impurities present to form nuclei).

- The droplet is assumed to be spherical, and the droplet growth is based on average representative mean radii.

The k-ω SST model is employed with the default values of constants, to consider the turbulent flow effects. The k−ω SST model is suitable for wet steam flows because:

- High accuracy in near-wall regions: The last stage of a steam turbine has complex boundary layer conditions with rapid changes in pressure and velocity. The k−ω SST model performs very well in these regions and can accurately simulate the flow behavior.

- Phase interaction: This model can effectively handle complex conditions such as flow separation and the presence of liquid droplets.

- Combination of k−ε and k−ω advantages: Due to its hybrid nature, this model performs well both in regions far from the wall and near the wall, which is crucial for two-phase flows in turbines.

In all cases, the pressure-based solver is employed. In cases 1 to 5, the spatial discretization of pressure and momentum was carried out using the upwind second-order scheme. On the other hand, the MUSCL third-order discretization was utilized for density, turbulent kinetic energy, energy, and dissipation rate. Furthermore, for the wet steam parameters, the second-order upwind discretization was applied. In cases 6 and 7, a high-resolution technique was used to discretize the convective part of the Navier-Stokes equations.

3.3 Computational domain and boundary conditions

In this study, two distinct configurations are analyzed. The first is the IWSEP nozzle and the second is the linear rotor-blade cascade, mentioned in chapter 2. The computational mesh and boundary conditions for the geometries are illustrated in Fig. 3.1 and 3.2. Additional details regarding the experimental setup were provided in chapter 2.
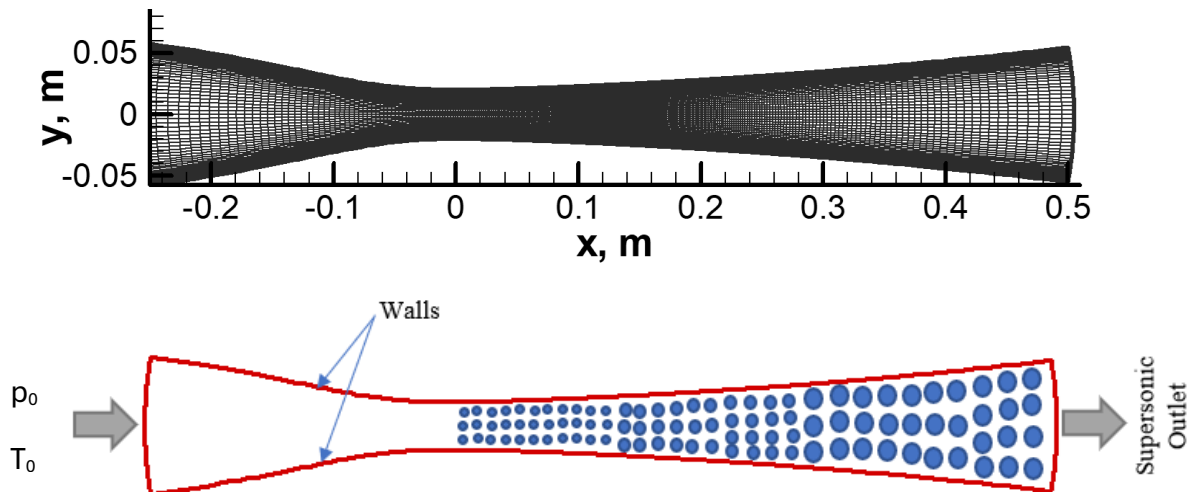
Fig. 3.1. Computational mesh and boundary conditions for IWSEP nozzle
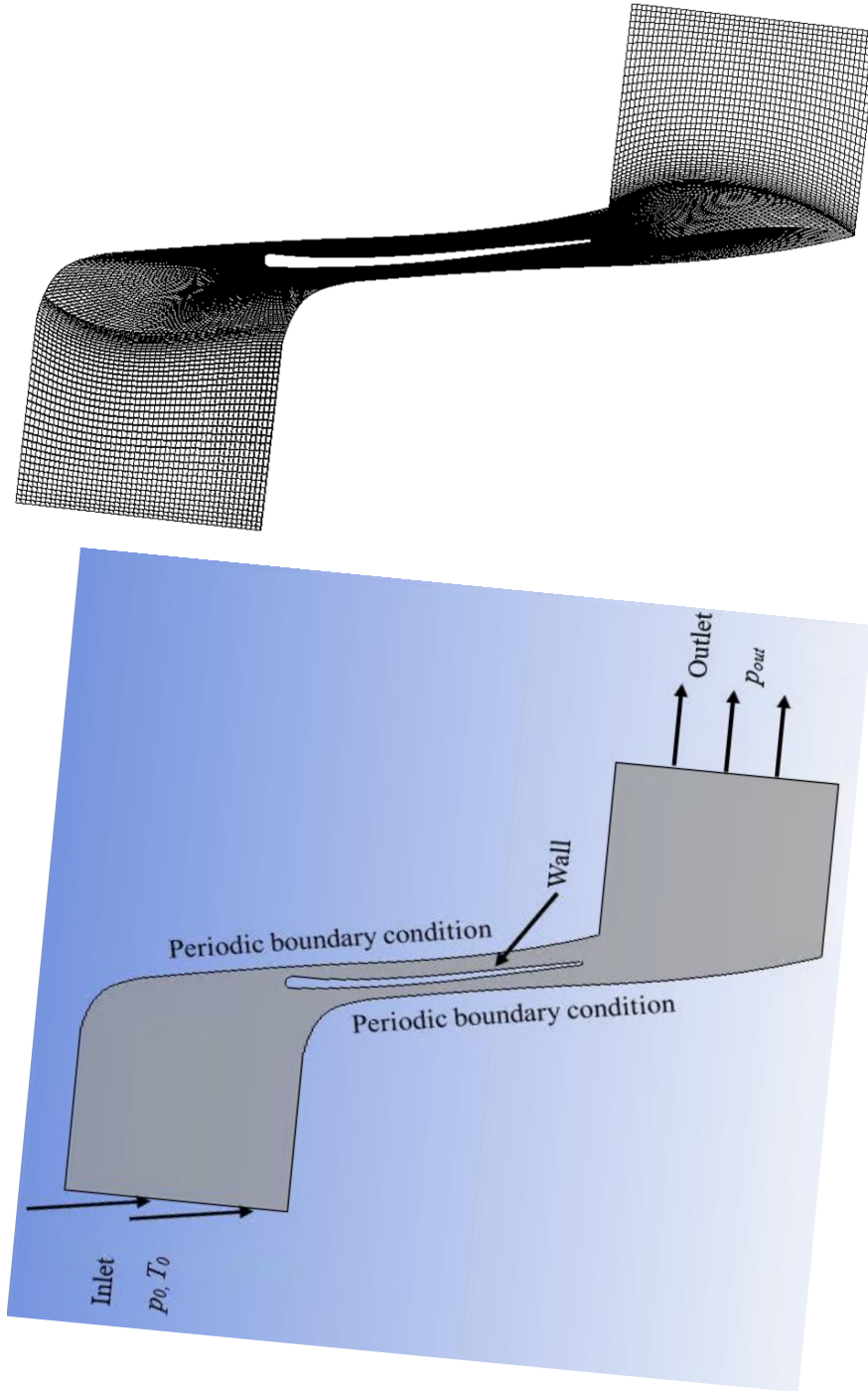
Fig. 3.2. Computational mesh and boundary conditions for the linear rotor cascade

Table 3.2 provides the inlet and outlet conditions for the investigated geometries. At the inlet, a total pressure and temperature, and at the outlet, the average value of static pressure has been considered. An inlet turbulence intensity of 5% was taken into account. The same numerical grid is used for the nozzle and linear cascades across all CFD methods considered in this study.

Table 3.2. Inlet and outlet conditions for the investigated geometries

	p_0, kPa	T_0, °C	p_{out}, kPa	Inlet flow angle, °
IWSEP nozzle	77.80	101	Supersonic	0
Rotor cascade	65.00	130.5	14.00	6.5

3.4 Results and discussion

3.4.1. Searching for the optimal case within the IWSEP nozzle

Figures 3.3, 3.4, and 3.5 compare the numerical results of the cases with experimental data measured in the SUT laboratory. Figure 3.3 shows the static pressure distribution along the nozzle. As observed, cases 3 and 4 predict the location of the condensation shock well, and cases 5 and 6 predict the intensity of the condensation shock well. Since predicting the condensation shock is a critical issue, it is concluded that the results of cases 3, 4, 5, and 6 are more suitable compared to other cases, while the results of cases 1, 2, and 7 are not acceptable.

Figure 3.4 compares the numerical results of the mean droplet diameter for the cases with experimental data. As observed, case 7 shows the best agreement with the experimental results compared to the other cases. Cases using the Young droplet growth model (cases 1, 2, 5, and 7) have results that are closer to the experimental data. However, cases using the Gyarmathy or Fuchs-Sutugin droplet growth models (cases 3, 4, and 6) do not provide acceptable results for the droplet diameter.

Figure 3.5 compares the distribution of the liquid mass fraction along the nozzle for the cases with experimental data. As observed, there is good agreement between the experimental and numerical results, and the results of all cases fall within the same range. This is because, according to the following relationship, liquid mass depends on both droplet diameter and number of droplets. As a consequence, a case with larger droplets has fewer number of droplets, and conversely, a case with smaller droplets has more droplets. Therefore, despite significant differences in droplet diameter results among the cases (Fig. 3.4), the liquid mass fraction remains within the same range for all cases. In Table 3.3, the percentage differences between the experimental and numerical results for the various cases are presented, providing a summary of the results obtained above. It was calculated by comparing the experimental data values and the numerical values at the defined point in the table.

$$y = \frac{m_l}{m_m}, m_l = \frac{4}{3}\pi r^3 \rho_l \times N \qquad (3.31)$$
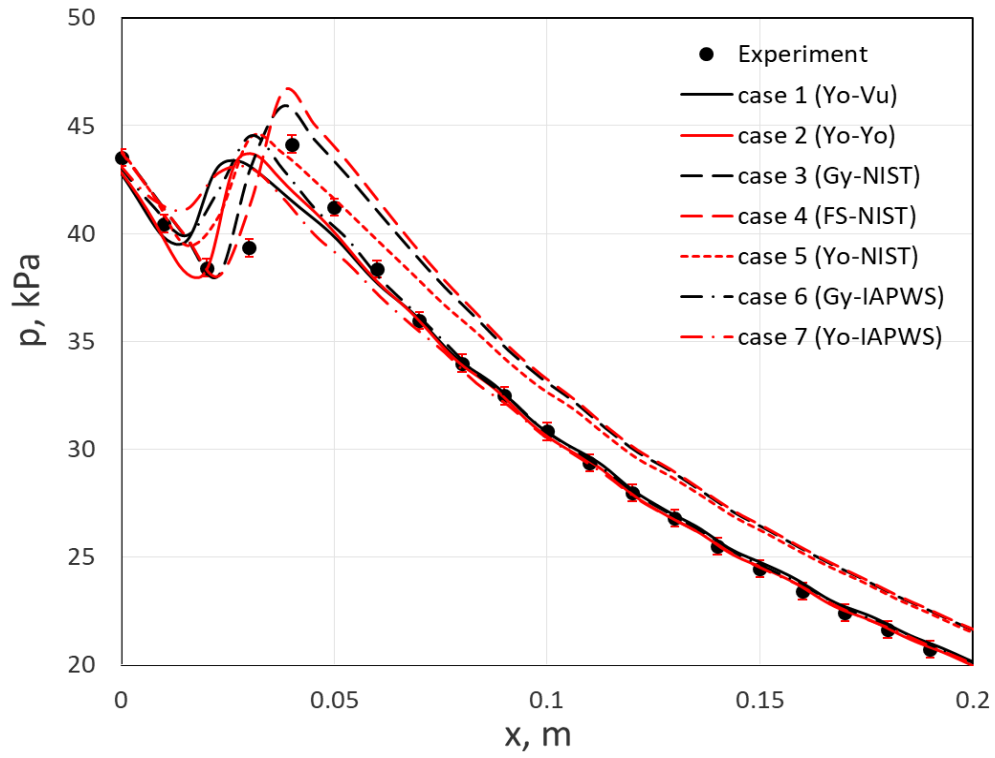
Fig. 3.3. Distribution of the static pressure across the IWSEP nozzle for different cases and comparison with experimental data
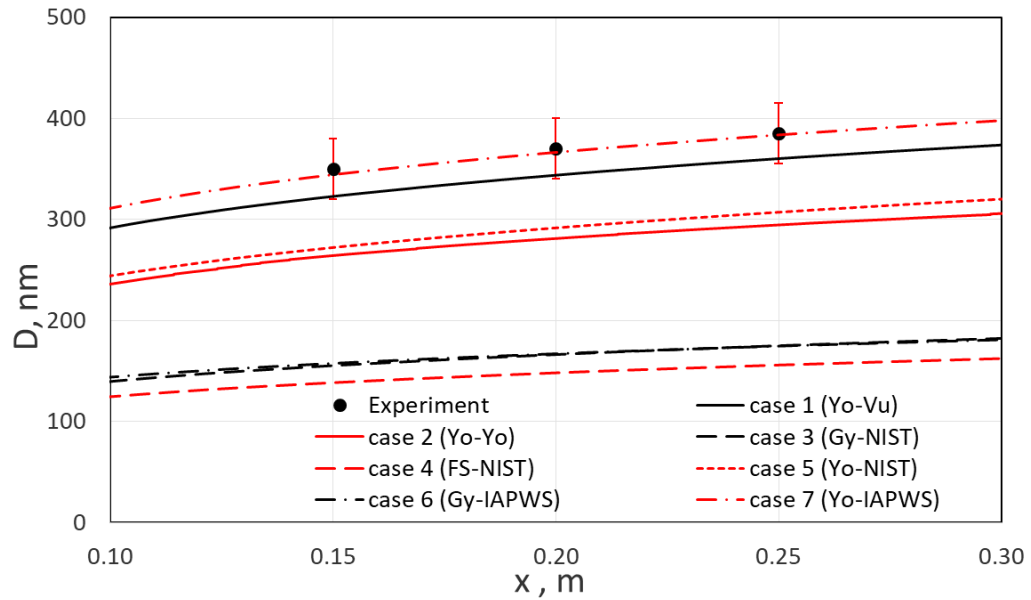
Fig. 3.4. Distribution of the droplet average diameter through the IWSEP nozzle for different cases and comparison with experimental data
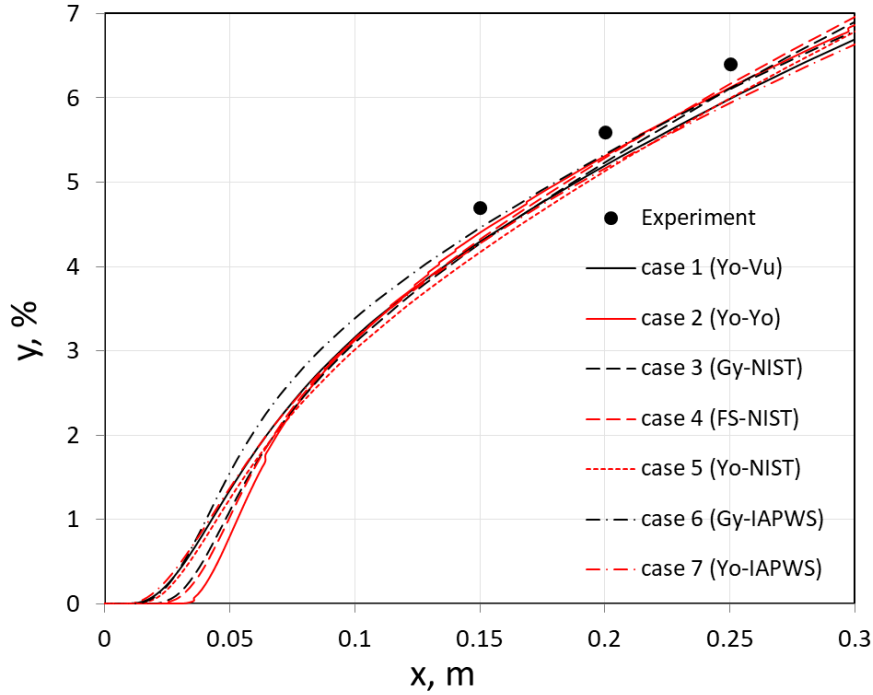
Fig. 3.5. Liquid mass fraction through the IWSEP nozzle for different cases and comparison with experimental data

Table 3.3. The percentage variance between computational results and experiments (%)

Test case	Condensation shock (x=0.04 m)		Droplet average diameter, at x=0.2 m	Liquid mass fraction, at x=0.2 m
	Location	Intensity		
Case 1 (Yo-Vu)	35	1.8	7.5	7.5
Case 2 (Yo-Yo)	27.5	1	24	5.5
Case 3 (Gy-NIST)	0	4	55	6.5
Case 4 (FS-NIST)	0	5.5	60	5.5
Case 5 (Yo-NIST)	25	0	21.5	8
Case 6 (Gy- IAPWS)	25	0	55	4.5
Case 7 (Yo- IAPWS)	30	2.5	0	7.5

The aim of this section is to compare the isentropic efficiency results for the cases. Isentropic efficiency is defined by the following equation, which essentially compares the actual performance (a) of a process with the ideal isentropic performance (s) of that process for a machine. In the equation below, subscripts 1 and 2 represent the nozzle inlet and outlet,

respectively. The isentropic efficiency results for all cases are presented in Table 3.4. As can be seen, case 2 shows non-physical results. The reason for this is that in case 2, the Virial equation formulated by Young is used as the equation of state. While this equation is suitable for equilibrium conditions (the dry-steam region), it must be extrapolated into the meta-stable zone to calculate the properties of supercooled vapor (wet steam region), which extends beyond the equation's valid range. Therefore, this case is not recommended for simulating wet steam flows.

$$\eta = \frac{h_1 - h_{2a}}{h_1 - h_{2s}} = \frac{h_1 - h_{2a}}{h_1 - h_{2a} + T_{2a}ds_{2a-1}} \tag{3.32}$$

Table 3.4. Values of isentropic efficiency along the IWSEP nozzle centreline for all cases

Test case	Isentropic efficiency (η)
Case 1 (Yo-Vu)	0.984
Case 2 (Yo-Yo)	1.073 (unphysical value!)
Case 3 (Gy-NIST)	0.972
Case 4 (FS-NIST)	0.972
Case 5 (Yo-NIST)	0.969
Case 6 (Gy- IAPWS)	0.971
Case 7 (Yo- IAPWS)	0.968

Figures 3.6, 3.7 and 3.8 show the contours of Mach number, static pressure, and liquid mass fraction along the IWSEP nozzle for all cases, respectively. As observed in Fig. 3.6, in the converging section of the nozzle, the Mach number is less than one, indicating subsonic flow. At the throat, the Mach number reaches one. Following a rapid expansion in the diverging section, the flow velocity significantly increases, leading to supersonic conditions. In cases 1 and 2, the values and distribution of Mach number at the outlet differs from the other cases. In contrast to the Mach number, as can be seen in Fig. 3.7, the static pressure continuously decreases from the inlet to the outlet. In the diverging section, due to the significant increase in velocity, both pressure and temperature drop sharply. Therefore, in this region, phase change or condensation occurs, and liquid droplets appear in the vapor phase. Fig. 3.8 confirms previous observations. In cases 3 and 4, the value of liquid mass fraction at the outlet is higher compared to the other cases, and 10 percent of the mixture's mass belongs to the liquid phase.

Case 1 (Yo-Vu)

Case 2 (Yo-Yo)

Case 3 (Gy-NIST)

Case 4 (FS-NIST)

Case 5 (Yo-NIST)

Case 6 (Gy-IAPWS)

Case 7 (Yo-IAPWS)
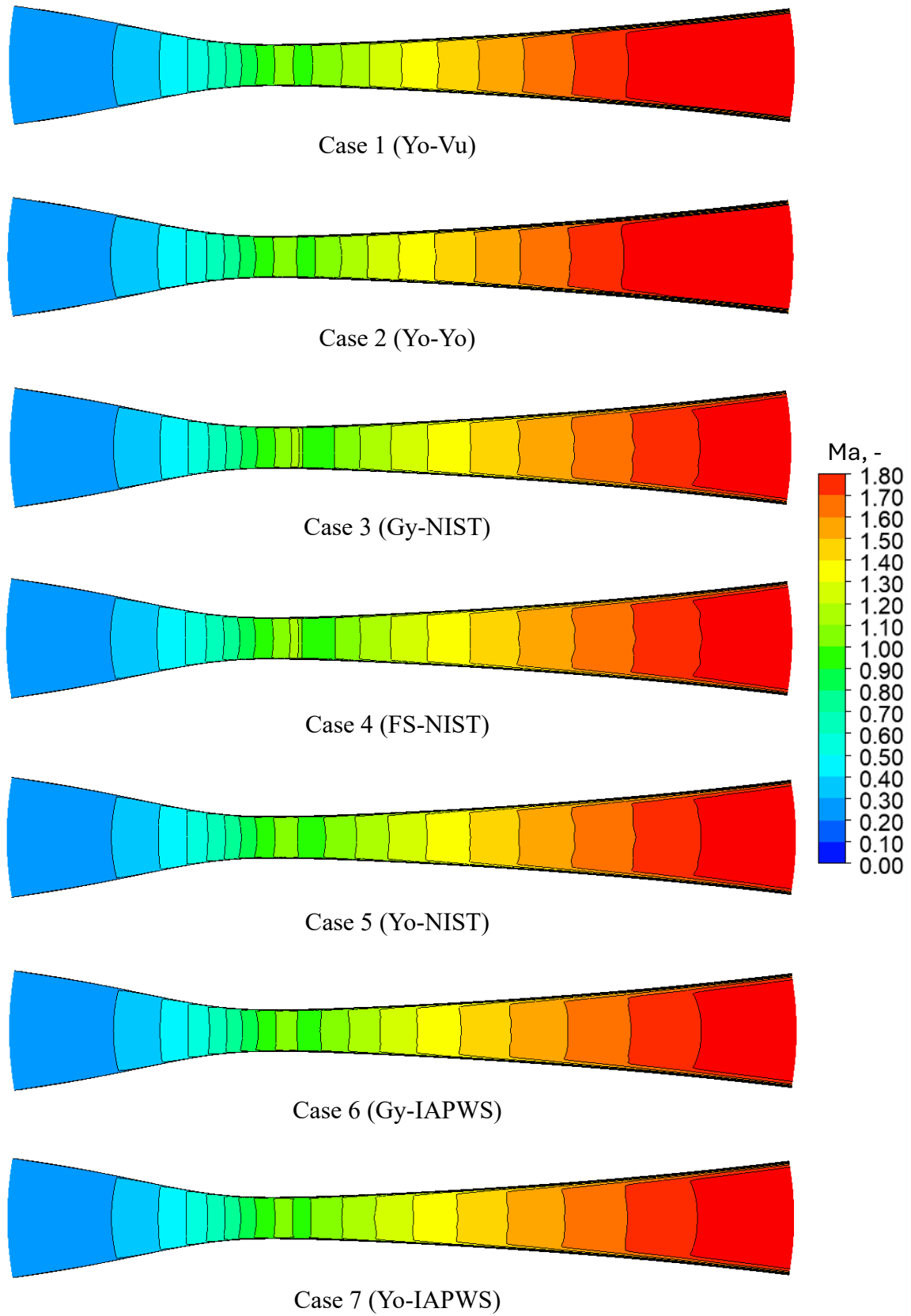
Fig. 3.6. Mach number contours along the IWSEP nozzle for selected cases

Case 1 (Yo-Vu)

Case 2 (Yo-Yo)

Case 3 (Gy-NIST)

Case 4 (FS-NIST)

Case 5 (Yo-NIST)

Case 6 (Gy-IAPWS)

Case 7 (Yo-IAPWS)
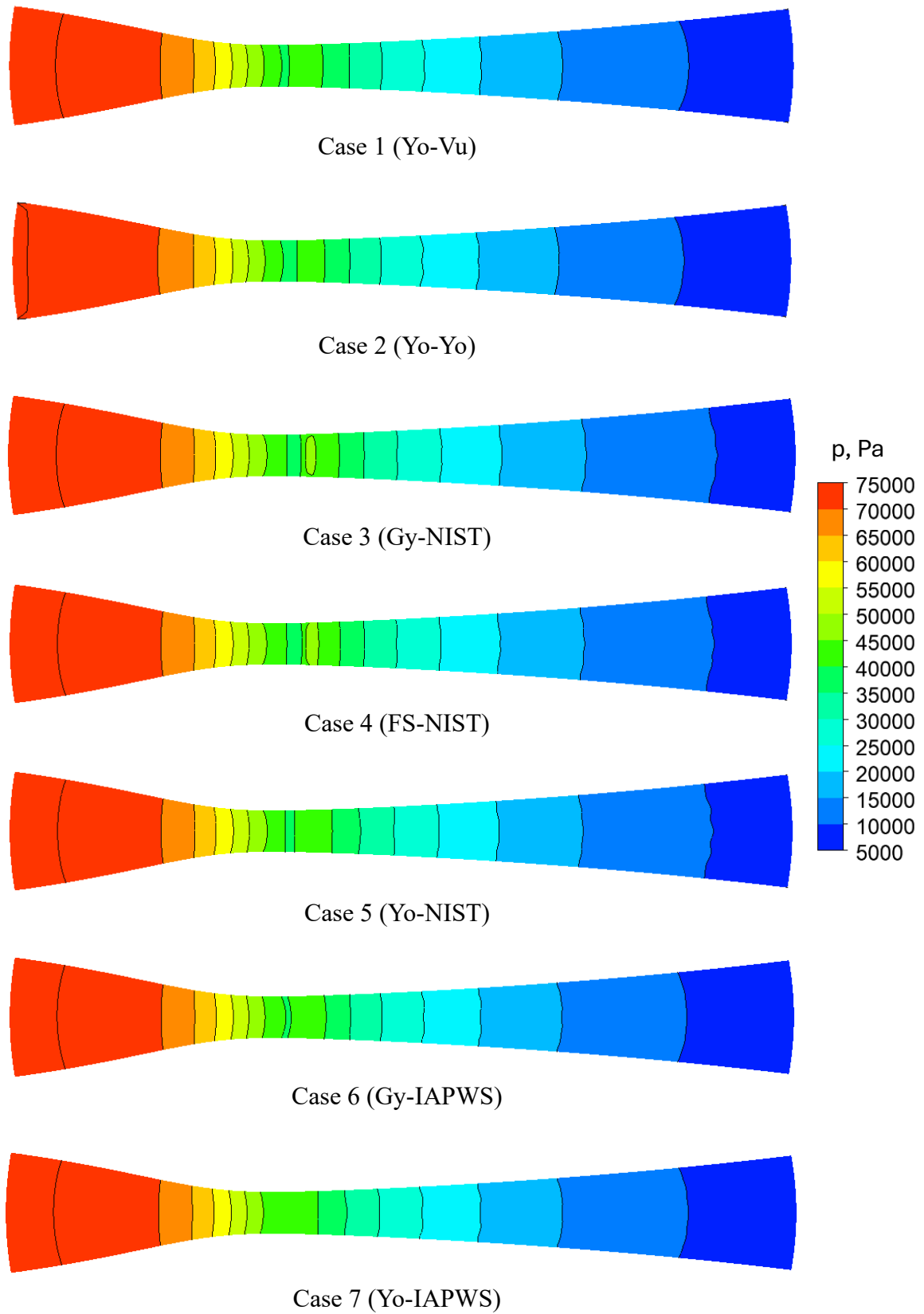
Fig. 3.7. Static pressure contours along the IWSEP nozzle for all cases
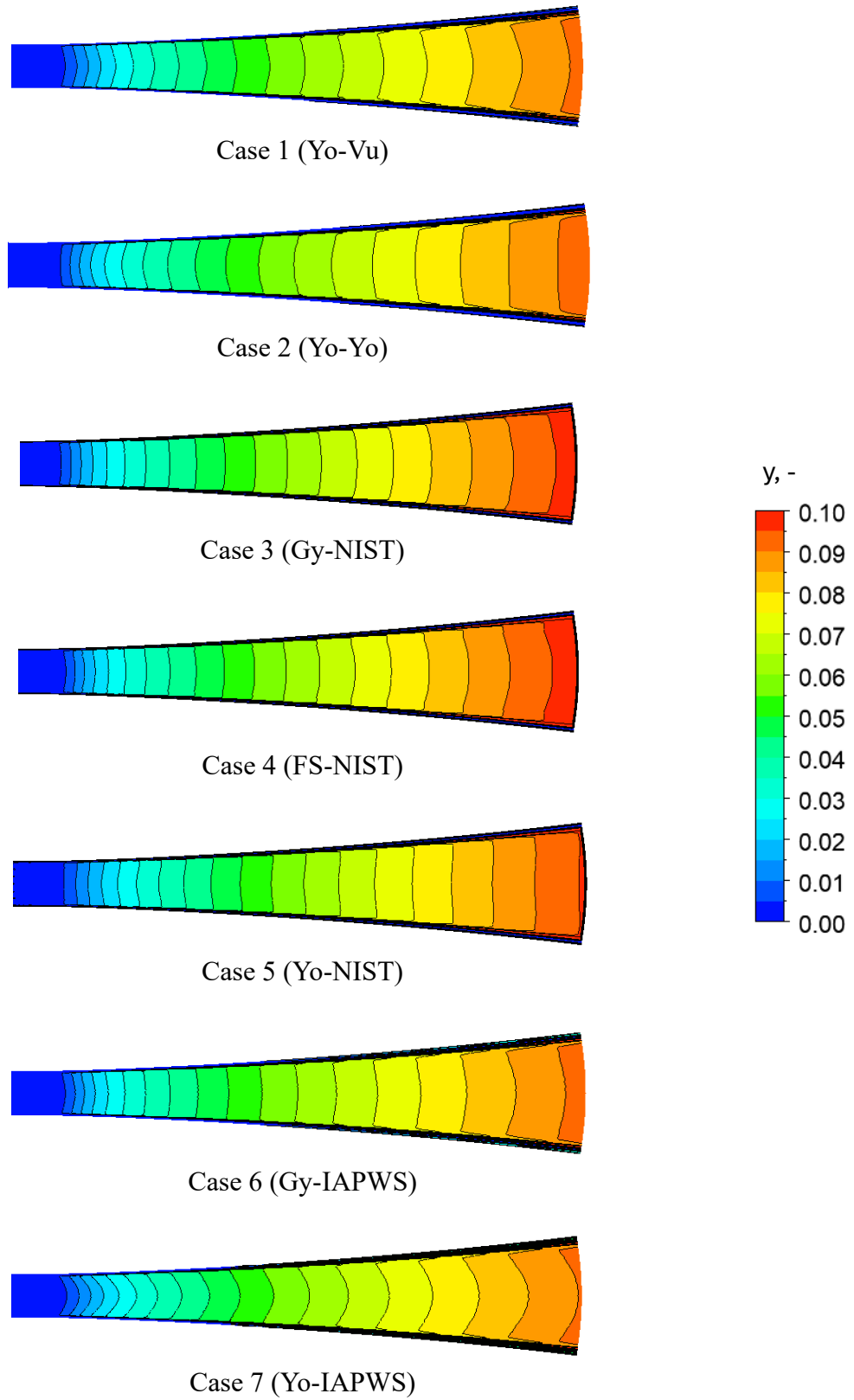
Fig. 3.8. Liquid mass fraction contours along the IWSEP nozzle for all cases

3.4.2. Searching for the optimal case within the linear rotor cascade

Figure 3.9 compares the static pressure distribution on the rotor blade for the cases with experimental data. As can be seen, on the suction side of the blade, cases 3 and 4 are the best cases which predict properly the position of the reflected shock wave interacting with condensation process that occurs between x/c=0.5 and x/c=0.6. On the pressure side of the blade, the results of the cases 3, 4, 5, 6 and 7 are closer to experimental data, while cases 1 and 2 show the worst results. On the pressure side, especially case 6 follows the same trend as the experimental data.

Table 3.5 presents the isentropic efficiency results for the cases, which are obtained based on averaging the enthalpy and entropy values at the rotor's inlet and outlet. As can be seen, cases 1, 2, and 7 provide non-physical results, and therefore, these cases are not recommended for simulating wet steam flows.
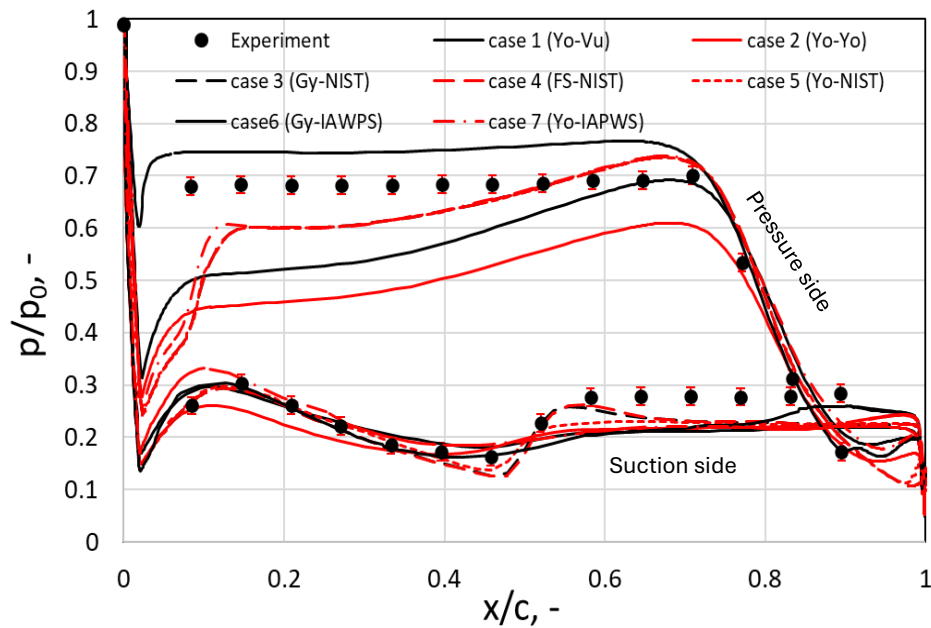
Fig. 3.9. The distribution of the static pressure on the rotor blade for different cases and comparison with experimental data

Table 3.5. Values of isentropic efficiency for the rotor blade

Test case	Isentropic efficiency (η)
Case 1 (Yo-Vu)	2.087 (unphysical value!)
Case 2 (Yo-Yo)	2.735 (unphysical value!)
Case 3 (Gy-NIST)	0.965
Case 4 (FS-NIST)	0.965
Case 5 (Yo-NIST)	0.966
Case 6 (Gy- IAPWS)	0.976
Case 7 (Yo- IAPWS)	1.117 (unphysical value!)

Figures 3.10, 3.11 and 3.12 show the contours of Mach number, static pressure, and liquid mass fraction along the rotor cascade for all cases, respectively. As shown in Fig. 3.10, the Mach number increases from the inlet towards the outlet. The highest Mach number occurs at the middle of the blade on the suction side. In this region, the fish tail shock wave interacts with the condensation phenomenon and gets reflected. The Mach number in this region is higher for cases 3, 4, and 5 compared to the other cases. As observed in Fig. 3.11, the static pressure decreases from the inlet towards the outlet. The lowest pressure occurs at the middle of the blade on the suction side, which corresponds to the regions with the highest Mach number. Fig. 3.12 shows the values of the liquid mass in all the sections. The liquid phase appears on the suction side of the blade, precisely where the static pressure is at its lowest. In cases 6 and 7, the liquid phase appears earlier, and the values of the liquid phase fraction are higher than in the other cases.

Case 1 (Yo-Vu)

Case 2 (Yo-Yo)

Case 3 (Gy-NIST)

Case 4 (FS-NIST)

Case 5 (Yo-NIST)

Case 6 (Gy-IAPWS)

Case 7 (Yo-IAPWS)
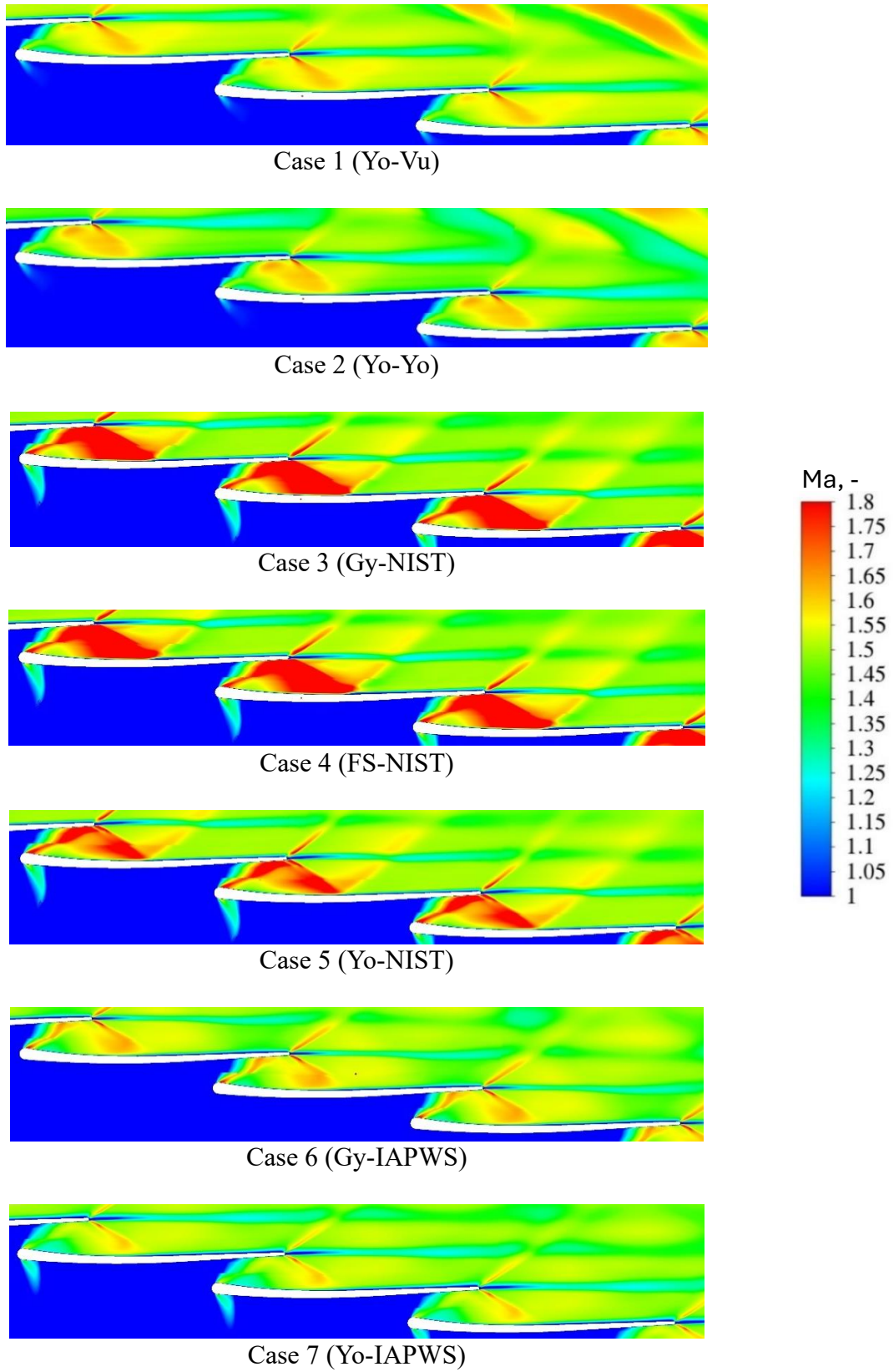
Fig. 3.10. Mach number contours along the rotor cascade for all cases

Case 1 (Yo-Vu)

Case 2 (Yo-Yo)

Case 3 (Gy-NIST)

Case 4 (FS-NIST)

Case 5 (Yo-NIST)

Case 6 (Gy-IAPWS)

Case 7 (Yo-IAPWS)

Fig. 3.11. Static pressure contours along the rotor cascade for all cases

Case 1 (Yo-Vu)

Case 2 (Yo-Yo)

Case 3 (Gy-NIST)

Case 4 (FS-NIST)

Case 5 (Yo-NIST)

Case 6 (Gy-IAPWS)
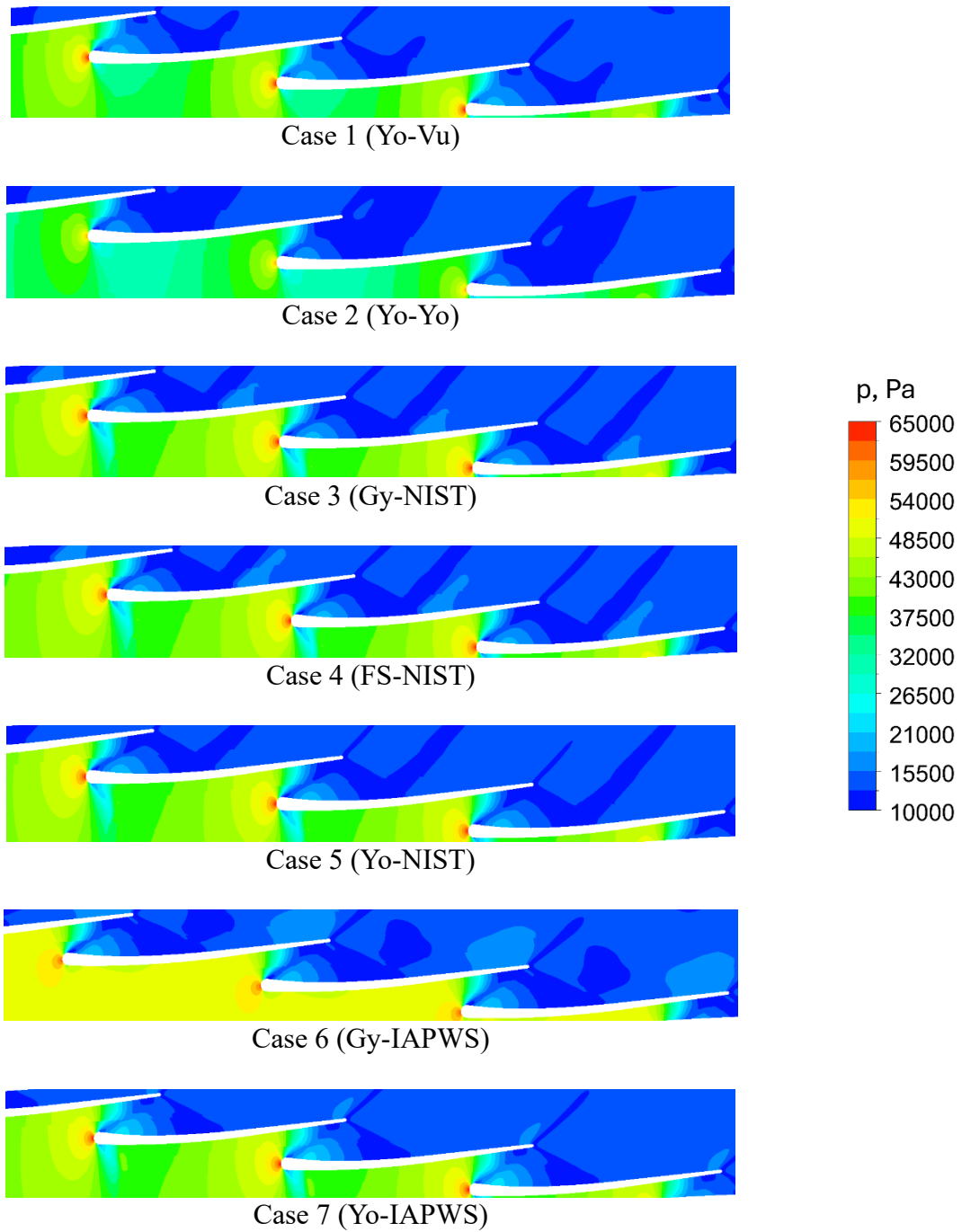
Case 7 (Yo-IAPWS)
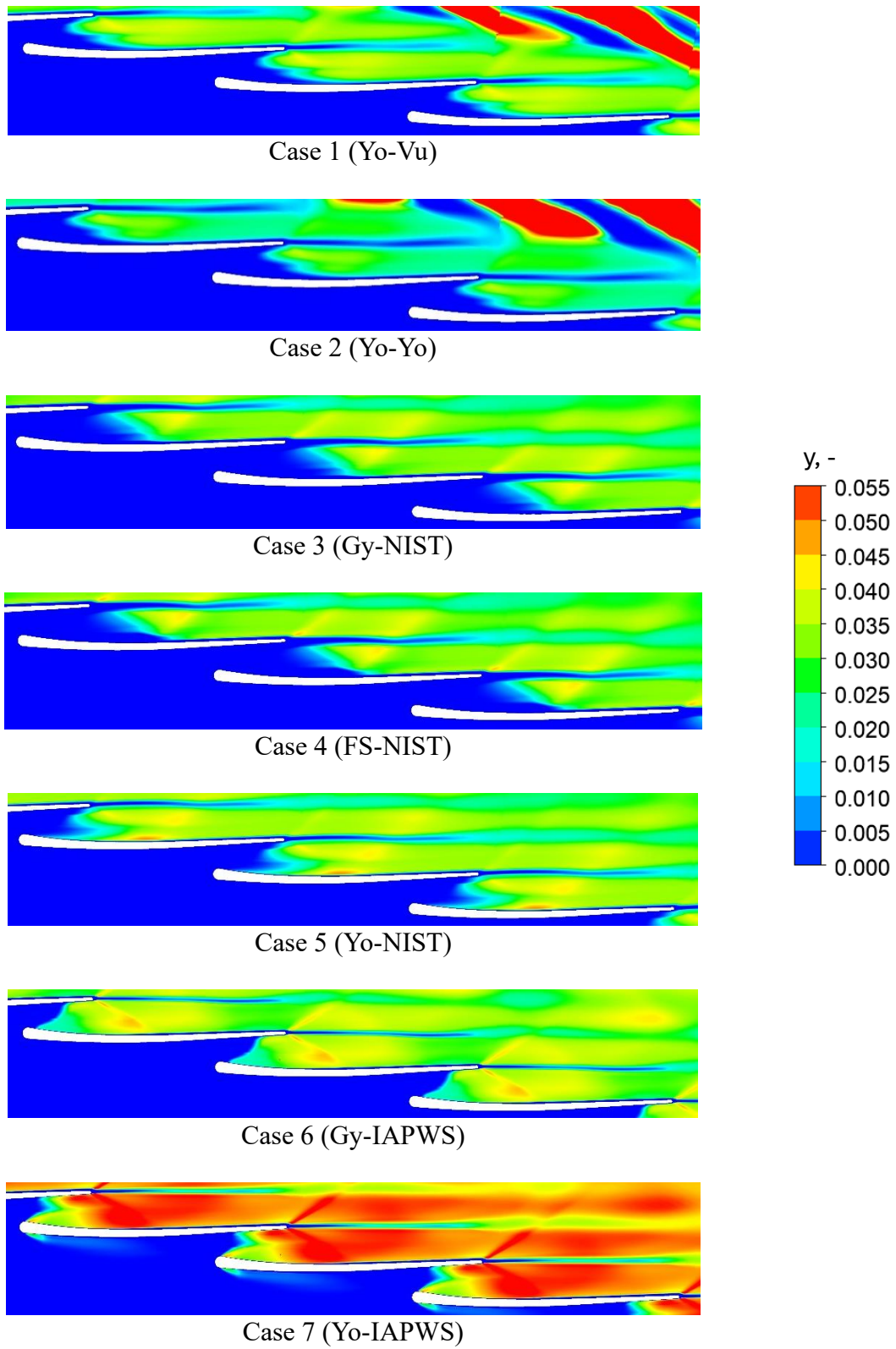
Fig. 3.12. Liquid mass fraction contours along the rotor cascade for all cases

3.5 Conclusions

In this chapter, the wet steam flow through the IWSEP nozzle and a linear rotor-blade cascade was simulated. Seven different cases employing various CFD tools were evaluated. To determine the most appropriate case, the numerical results were compared with SUT's experimental data, leading to the following conclusions.

- Cases 3, 4, and 6 proved to be the most accurate in predicting the static pressure distribution for both geometries, while cases 1 and 2 showed the poorest performance in this regard.

- Cases 1, 2, and 7 are not suitable for modelling wet steam flows, as they produced unrealistic values for isentropic efficiency, making them unreliable for accurate simulations.

- The Gyarmathy and Fuchs-Sutugin droplet growth models (cases 3, 4, and 6) demonstrated superior reliability and accuracy in predicting flow behaviour compared to the Young model (cases 1, 2, 5, and 7). These models provided more consistent results, making them more effective for simulating wet steam flows.

In conclusion, based on the findings, using cases 3 (Gy-NIST), 4 (FS-NIST), and 6 (Gy-IAPWS) for modelling condensation phenomena are recommended. However, both the Gyarmathy and Fuchs-Sutugin droplet growth models require adjustments to improve the accuracy of predicting the average droplet diameter. The results highlight the sensitivity involved in modelling such flows and underscore the importance of carefully selecting the appropriate numerical model to ensure reliable outcomes.

4. 3D Simulation of Wet Steam Flows in a Low Pressure Condensing Steam Turbine

Analyzing and simulating wet steam flows in steam turbines is of critical importance, particularly due to the presence of a liquid phase in the turbine's low-pressure stages, which leads to significant efficiency losses that must be carefully managed. However, this area remains relatively unexplored due to the inherent challenges in accurately modeling and analyzing three-dimensional wet steam flows. One of the primary difficulties lies in the complex blade geometry, which generates vortices, flow separation, and shock waves, making precise CFD simulations highly challenging. Additionally, meshing such intricate structures requires a fine balance between resolution and computational cost. This chapter aims to address these challenges by employing advanced CFD techniques to analyze wet steam behavior within the complex 3D geometry of a 200 MW low-pressure steam turbine.

In addition, the chapter provides practical equations for quantifying losses across the entire turbine stage, offering a valuable framework for assessing performance and guiding design enhancements to minimize these losses. This research addresses a crucial gap by providing quantitative estimates of losses within the actual three-dimensional geometries of turbine blades—a topic that has not been thoroughly investigated in recent studies. By conducting detailed loss assessments based on real blade geometries, this study aims to produce more reliable and precise insights, contributing significantly to the optimization of steam turbine designs.

4.1 Fundamental theory for an axial steam turbine

The passage of steam through the stages of a steam turbine results from the transfer of energy from the steam to the turbine blades, ultimately generating mechanical power. In the following, it will be explained in detail the reasons behind the steam flow through the stages and their operation:

1. Conversion of thermal energy to mechanical energy

- Stator:

- The stator's role is to change the direction of the steam flow and direct it toward the rotor. This change in direction ensures that the steam hits the rotor blades at an optimal angle.

- As the steam passes through the fixed blades of the stator, its velocity increases (expansion process). This increase in velocity is accompanied by a decrease in steam pressure, converting the steam's thermal energy into kinetic energy.

- Rotor:

- The rotor consists of moving blades attached to the turbine shaft. When high-velocity steam strikes the rotor blades, it transfers a portion of its kinetic energy to the rotor.

- This energy transfer causes the rotor to rotate, converting the steam's kinetic energy into mechanical energy in the turbine shaft. This mechanical energy can then be used for electricity generation or other mechanical work.

2. Gradual increase in efficiency and performance

- Steam turbines typically consist of multiple stages to extract the maximum amount of energy from the steam. In each stage, the steam loses some of its energy, but as it passes through successive stages, the energy extraction process becomes more efficient.

- The multi-stage design of a steam turbine ensures that the reduction in steam pressure and temperature occurs gradually and effectively, which contributes to increased efficiency and overall performance of the turbine.

3. Speed control and steam flow regulation:

- Stators play a crucial role in regulating the steam flow rate and directing it toward the rotor at the appropriate angle and orientation. This is particularly important because ensuring that the steam strikes the rotor blades at the right angle maximizes the energy transfer to the rotor.

- By precisely adjusting the angle of the stator blades, the steam flow can be directed in a way that enhances the overall efficiency of the turbine.

4. Improved force distribution and reduction of mechanical stress

The presence of multiple stages ensures that the mechanical force generated by the steam is distributed more evenly across the turbine shaft. This uniform distribution reduces mechanical stress on various turbine components, thereby enhancing their durability and extending the turbine's lifespan.

4.1.1. Velocity diagrams of the axial turbine stage

A turbine stage typically comprises a fixed stator row and a rotating rotor row. The flow progression within the axial turbine stage is analyzed using velocity triangles at the mean diameter of the turbine blade, as depicted in Fig. 4.1. In this study, it is assumed that the flow enters the turbine stator with an absolute velocity c_1 and an angle α_1. After accelerating through the stator, the flow exits with velocity c_2 and angle α_2, which serve as the inlet conditions for the rotor. At the rotor inlet, the relative velocity w_2 and angle β_2 are determined based on the vectorial subtraction of the blade speed u from the absolute velocity c. The flow undergoes further acceleration within the rotor and exits with a relative velocity w_3 and angle β_3. These velocity relationships and assumed parameters form the basis for the subsequent analysis in this thesis.

$$\vec{w} = \vec{c} - \vec{u} \tag{4.1}$$
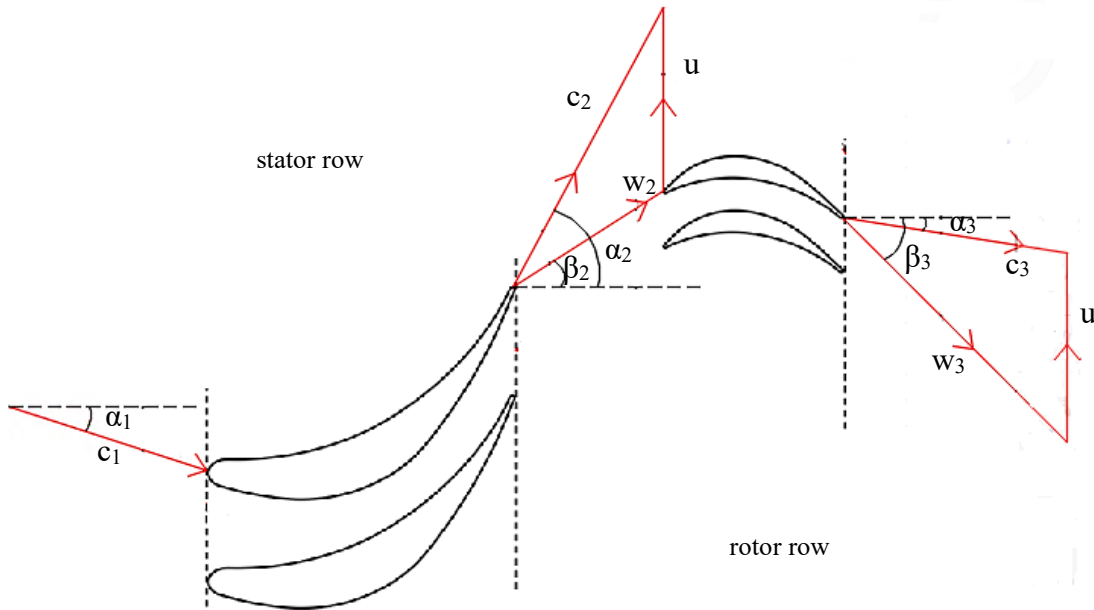
Fig. 4.1. Turbine stage velocity diagrams

4.1.2. Thermodynamics of the axial turbine stage

The expansion process of a fluid element through the final turbine stage is shown in Fig.4.2, and for the entire low-pressure part in Fig.4.3. In the low-pressure part of the steam turbine, two configurations are considered: one with the Baumann rotor and the other with only the last stage without the Baumann rotor. The Baumann stage is designed to enhance turbine power output without increasing the length of the last stage blade by utilizing an additional set of moving blades downstream. This approach helps extract more energy from the expanding steam. However, due to its more complex aerodynamic interactions and mechanical design, the Baumann rotor typically has lower efficiency compared to a free-standing last-stage blade. Additionally, the increased structural complexity can lead to higher manufacturing and maintenance costs. Currently, Baumann stages are mainly used in counter-pressure cogeneration turbines, where increasing power output is more important than efficiency losses. In contrast, a conventional last-stage blade without the Baumann rotor is simpler, more efficient, and commonly used in condensing steam turbines where maximizing overall efficiency is a priority. This study aims to analyze the performance of both configurations to determine their impact on efficiency and overall turbine performance.

To analyze the performance of an axial turbine stage, it is essential to consider the thermodynamic principles governing energy transfer. Applying the first law of thermodynamics to a turbine stage, the energy equation can be expressed as follows:

$$dq - dw = d(h + \frac{1}{2}c^2 + gz) \tag{4.2}$$

Where q is specific heat transfer to the fluid, w is specific work done by the fluid, h is the enthalpy, c is the flow velocity, g is the gravity, and z is the change in potential height in the direction of the resultant of the acting gravity force.

If we assume that the turbine is an adiabatic machine, as the heat exchange (q) with the surrounding is small compared to total enthalpy drop ($q \approx 0$). The same is true for the change of potential height ($z \approx 0$). These assumptions are normally realistic because the heat transfer and change in potential energy gz are small compared to the turbine work. Therefore, the specific work done by the stage, equals the total enthalpy drop incurred by the fluid passing through the stage:

$$l = h_{01} - h_{03} \text{ in Fig. 4.2}, \quad l = h_{01} - h_{04} \text{ in Fig. 4.3} \tag{4.3}$$

And the output power of the turbine can be calculated:

$$P_t = \dot{m}l \tag{4.4}$$

As no work is done in the nozzle row, the total enthalpy across it remains constant:

$$h_{01} = h_{02} \text{ in Fig.4.2,} \quad h_{02} = h_{03} \text{ in Fig.4.3} \tag{4.5}$$

The definition of total enthalpy for stator and rotor is as follows:

For stator:

$$h_0 = h + \frac{1}{2}c^2 \tag{4.6}$$

For rotor:

$$h_{0,rel} = h + \frac{1}{2}w^2 \tag{4.7}$$

The relative total enthalpy, $h_{0,rel}$, remains unchanged through the rotor of the axial turbine, therefore:

$$h_{02,rel} = h_{03,rel} \text{ in Fig. 4.2, } h_{01,rel} = h_{02,rel} \text{ and } h_{03,rel} = h_{04,rel} \text{ in Fig. 4.3} \tag{4.8}$$
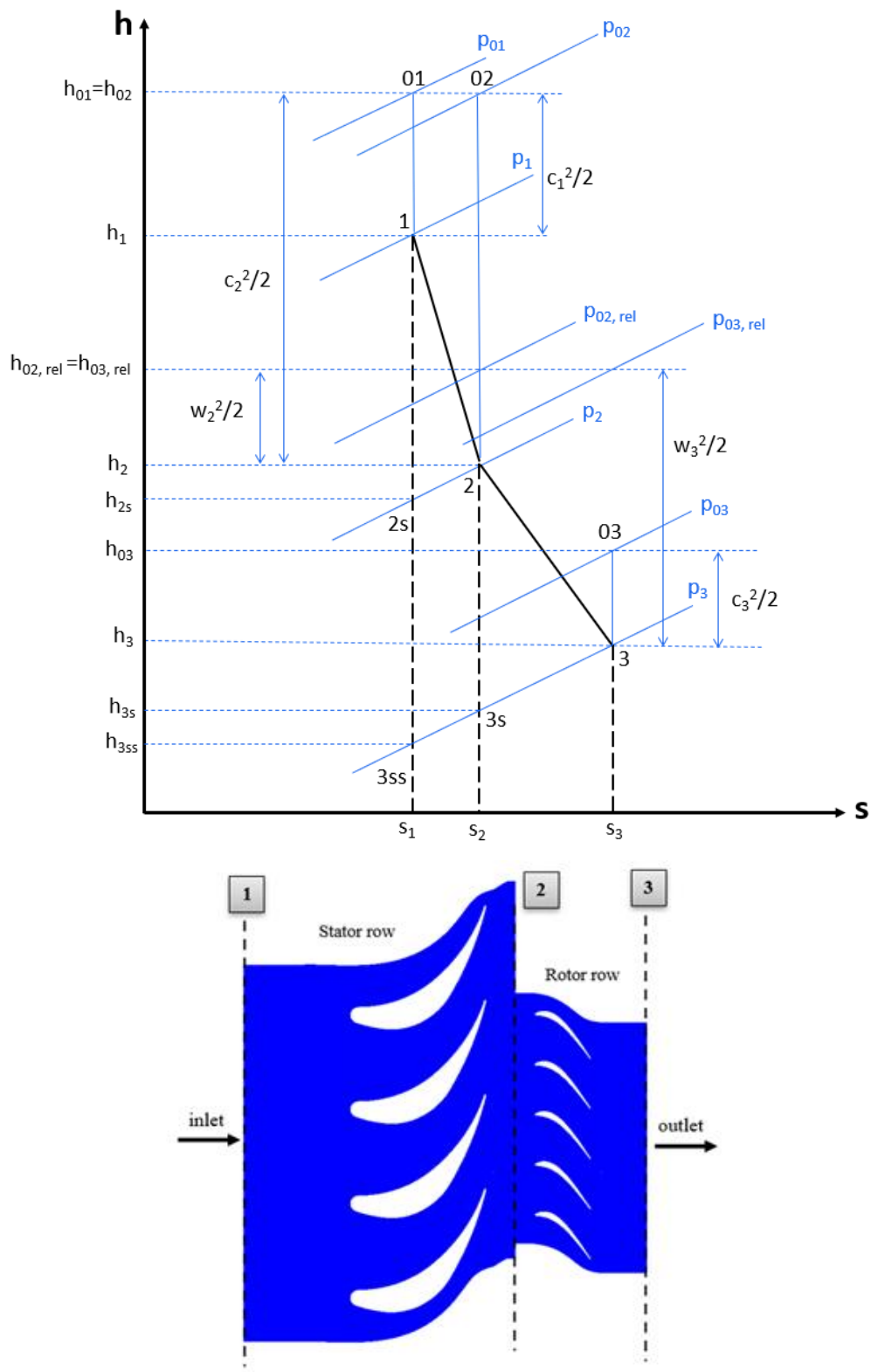
Fig. 4.2. Diagram displaying the expansion process within the turbine stage
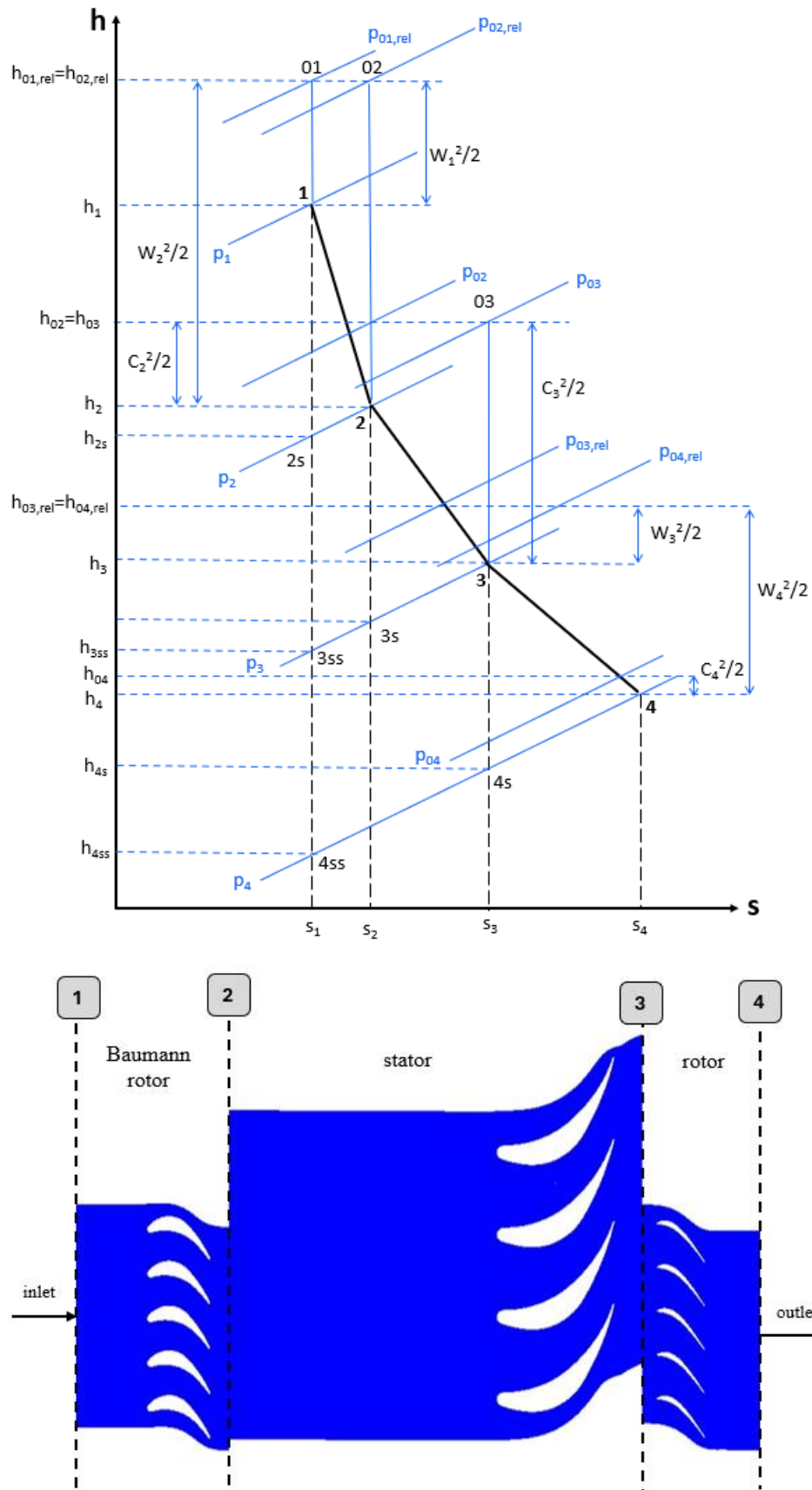
Fig. 4.3. Diagram displaying the expansion process within the LP part

4.1.3. Efficiency and loss coefficients

In any turbine flow process, there is always a discrepancy between the theoretical ideal (isentropic) work output and the actual work achieved during expansion. This difference arises from irreversibility within the expansion, which results in an increase in specific entropy (s). This irreversibility shift the expansion path and the final state point on the constant pressure curve to the right. Consequently, the available enthalpy drops for performing useful work becomes less than in the ideal case, where no entropy is generated ($\Delta s = 0$). In Fig.4.2, the process (1-2-3) is the actual process along the turbine stage, and the process (1-2s-3ss) is an ideal isentropic process. The actual turbine work per unit mass of fluid is determined by the total enthalpy change between the initial state (point 01) and the final state (point 03), which correspond to the total pressures p_{01} and p_{03}, respectively. In contrast, the ideal turbine work per unit mass is calculated based on the enthalpy change that occurs during an isentropic process between these same two pressure levels. To express the efficiency of turbine expansion, three common definitions of isentropic efficiency are often used, each corresponding to different assumptions about the recovery of exit kinetic energy. For a turbine stage, total-to-total efficiency (η_{tt}) is defined as:

$$\eta_{tt} = \frac{h_{01} - h_{03}}{h_{01} - h_{03ss}} \tag{4.9}$$

In total-to-total efficiency, it is assumed that the kinetic energy at the turbine exit can be recovered in a subsequent stage. This measure is primarily applied to the stages before the final one in a multistage turbine system. On the other hand, total-to-static efficiency is defined differently, as follows:

$$\eta_{ts} = \frac{h_{01} - h_{03}}{h_{01} - h_{3ss}} \tag{4.10}$$

The total-to-static efficiency assumes that all of the kinetic energy in the exhaust gas is lost and cannot be recovered. This is often the case in the final stage of a turbine, where the exhaust is released into the surrounding environment. In contrast, static-to-static efficiency evaluates the performance based on static conditions at both the inlet and outlet, and its definition is as follows:

$$\eta_{ss} = \frac{h_1 - h_3}{h_1 - h_{3ss}} \tag{4.11}$$

In this study, to simplify the analysis and better assess the contribution of each component to stage losses, we use the static-to-static efficiency relationship. To define the isentropic efficiency for each component:

For stator:

$$\eta_S = \frac{h_1 - h_2}{h_1 - h_{2s}} \tag{4.12}$$

For rotor:

$$\eta_R = \frac{h_2 - h_3}{h_2 - h_{3s}} \tag{4.13}$$

For stage:

$$\eta_{stage} = \frac{h_1 - h_3}{h_1 - h_{3ss}} \tag{4.14}$$

The relation for the entropy loss coefficient (ξ) is as follows, which can be obtained from the relation of the isentropic efficiency,

$$\xi_S = 1 - \eta_S = 1 - \frac{h_1 - h_2}{h_1 - h_{2s}} = \frac{h_2 - h_{2s}}{h_1 - h_{2s}} \tag{4.15}$$

$$\xi_R = 1 - \eta_R = 1 - \frac{h_2 - h_3}{h_2 - h_{3s}} = \frac{h_3 - h_{3s}}{h_2 - h_{3s}} \tag{4.16}$$

$$\xi_{stage} = 1 - \eta_{stage} = 1 - \frac{h_1 - h_3}{h_1 - h_{3ss}} = \frac{h_3 - h_{3ss}}{h_1 - h_{3ss}} \tag{4.17}$$

The entropy loss coefficient quantifies the amount of work lost due to irreversibility in both the stator and rotor. This is reflected in the differences between the actual and isentropic static enthalpies, (h_2-h_{2s}) for the stator and (h_3-h_{3s}) for the rotor. Essentially, it represents the portion of energy that is not converted into useful work, highlighting inefficiencies in the turbine. According to a thermodynamic principle applied along an isobar (dp = 0), the slope of the isobar line on an h-s (enthalpy-entropy) diagram corresponds to the local temperature T.

$$T ds = dh - v dp \, , dp = 0 \implies T = \frac{dh}{ds} \tag{4.18}$$

Therefore,

$$h_2 - h_{2s} \cong (s_2 - s_1).T_2 \qquad (4.19)$$

$$h_3 - h_{3s} \cong (s_3 - s_2).T_3 \qquad (4.20)$$

$$h_3 - h_{3ss} \cong (s_3 - s_1).T_3 \qquad (4.21)$$

The new equations are

$$\xi_S = \frac{(s_2 - s_1).T_2}{h_1 - h_2 + (s_2 - s_1).T_2} \qquad (4.22)$$

$$\xi_R = \frac{(s_3 - s_2).T_3}{h_2 - h_3 + (s_3 - s_2).T_3} \qquad (4.23)$$

$$\xi_{stage} = \frac{(s_3 - s_1).T_3}{h_1 - h_3 + (s_3 - s_1).T_3} \qquad (4.24)$$

For the LP part, according to Fig. 4.3, the loss coefficient is as follows:

$$\xi_{LP} = \frac{(s_4 - s_1).T_4}{h_1 - h_4 + (s_4 - s_1).T_4} \qquad (4.25)$$

Where **h** and **s** are the enthalpy and entropy of the wet steam mixture, and are calculated using the following equations:

$$h_m = (1 - y).h_v + y.h_l \qquad (4.26)$$

$$s_m = (1 - y).s_v + y.s_l \qquad (4.27)$$

Where y is the liquid mass fraction.

4.2 CFD method

In this study, case 6 in previous chapter is used with the same settings and assumptions, to simulate the compressible steady-state two phase wet steam flow in ANSYS CFX. As shown in the previous chapter, case 6 employs the Gyarmathy droplet growth equation and the IAWPS formulation to estimate the thermodynamic conditions of the phases, providing reliable results. Additionally, since ANSYS CFX is a widely used software among researchers for turbomachinery flow simulations, Case 6 is adopted for the further simulations in this study.

The investigated geometry is the real 3D geometry of low-pressure steam turbine stages. In two-dimensional modeling, only two spatial variables (x and y) are involved in solving the Navier-Stokes equations. In three-dimensional flow, an additional variable (z) is introduced, significantly increasing the computational load. The addition of a third dimension means greater computational complexity in both meshing and equation solving. Modeling three-dimensional flows requires considerably more computational power. The volume of data and the number of equations to be solved grow exponentially, meaning that solving 3D flows demands more memory and longer computational time. This may necessitate the use of parallel processing or high-performance computing (HPC). To sum up, compared to two-dimensional models, three-dimensional flow modeling is more complex due to the added dimension, increased flow field intricacies, higher computational demands, and more challenging meshing requirements. In cases such as wet steam two-phase flow in turbines, which require precise simulations, the use of 3D models is essential.

The Frozen Rotor approach was chosen for the stator-rotor interface in ANSYS CFX due to its computational efficiency and ability to provide steady-state performance predictions. By using a rotating reference frame, this method transforms the inherently transient flow into a steady-state problem, maintaining a consistent relative position between the rotor and stator. This significantly reduces computational cost and allows for a faster, more stable simulation process. Due to its balance between accuracy and efficiency, it remains a widely used method for preliminary design and analysis of turbomachinery flows.

4.3 Computational domain and boundary conditions

The geometry examined in this study is the low-pressure section of a 200 MW turbine, which is simulated in three dimensions (Fig. 4.4). Initially, the last stage is simulated separately. Then, the Baumann rotor (Bottom part) along with the last stage is analyzed, and finally, the results of these two cases are compared. Table 4.1 and Fig. 4.5 show the boundary conditions for the

low-pressure part and the last stage. Where (r) is the radial direction along the span, (θ) is the circumferential direction, and (z) is the axial direction aligned with the flow direction. The RANS equations are typically formulated and solved in the Cartesian coordinate system, but in certain cases, such as when specifying boundary conditions or for visualization purposes, a transformation to the cylindrical coordinate system may be required. Figure 4.6 shows the 3D view of the computational domain and the applied boundary conditions. It should be noted that these blades are 0.67 m away from the center of the shaft in the radial direction.
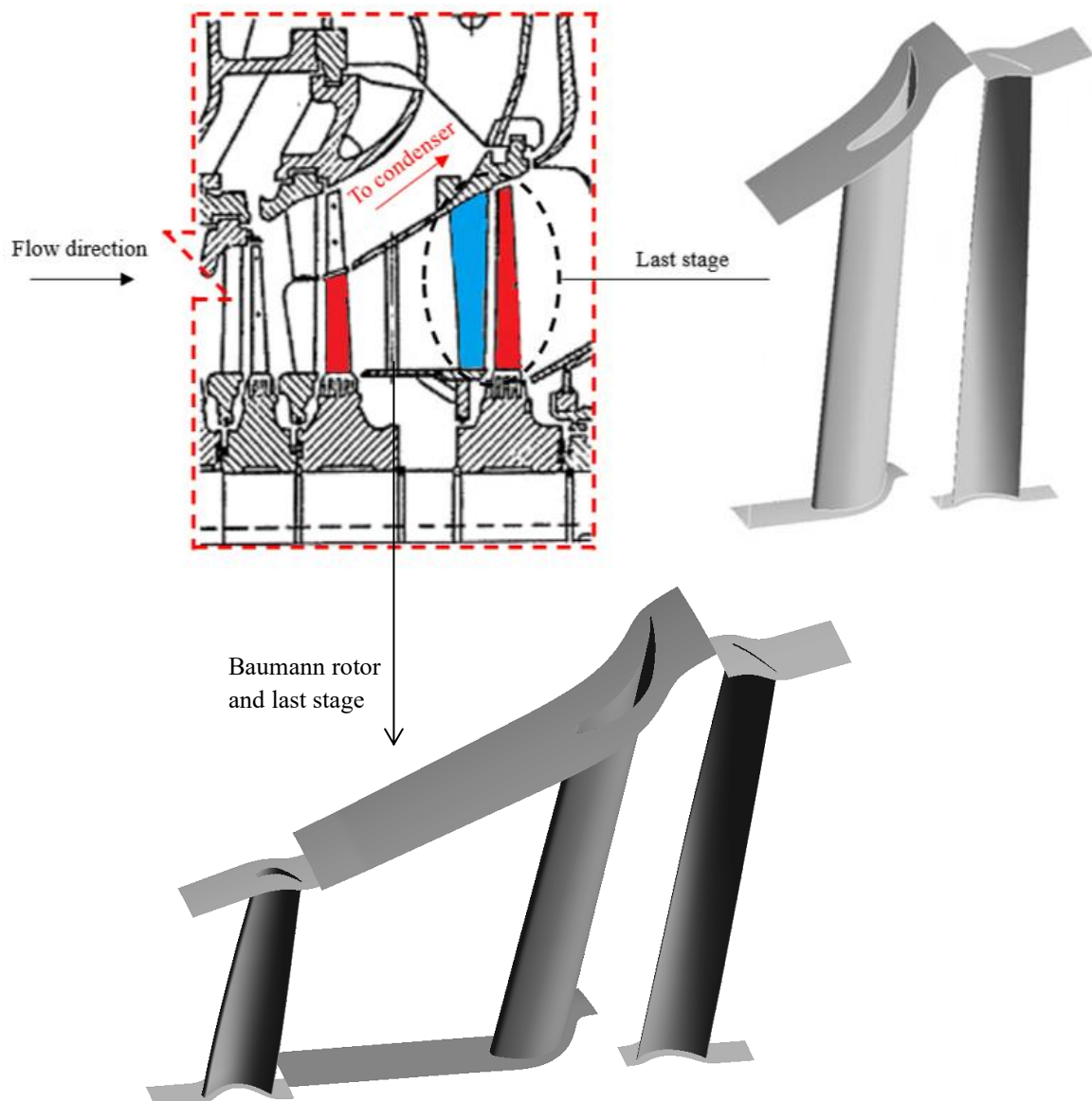
Fig. 4.4. Schematic of low-pressure part of steam turbine

Table 4.1- Boundary conditions for the last stage and low-pressure part

	p_0 (Pa)	p (Pa)	T_0 (K)	Turbulent intensity (%)	Incident angle (º)
Last stage inlet	14400	----	333.15	Zero gradient	0
Last stage outlet	----	5000	----	----	----
LP inlet	Fig. 4	----	Fig. 4	5	Fig. 4
LP outlet	----	5000	----	----	----
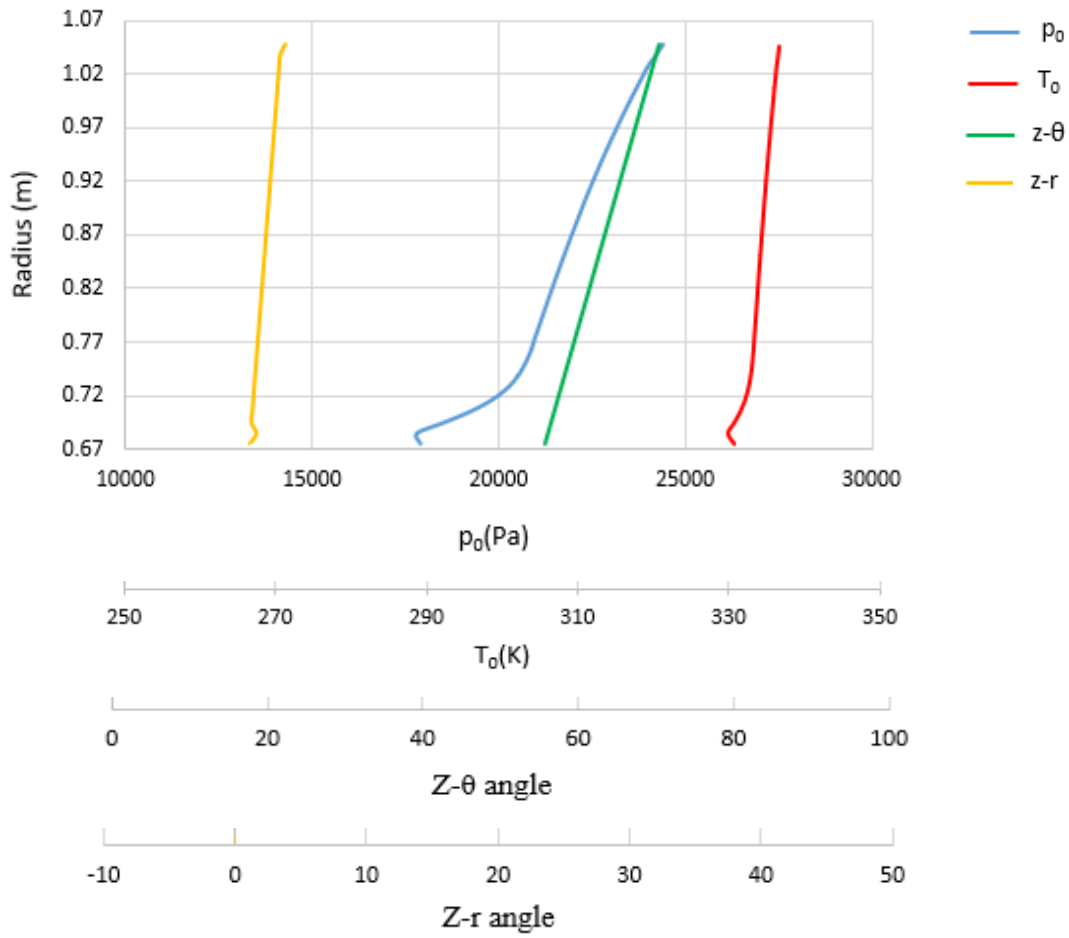
Fig. 4.5. Inlet boundary conditions along the blade length for the low-pressure part

Last stage

Radial direction (r)

Axial direction (z)

Circumferential
direction

Shroud

Rotor

Stator

90% Span

50% Span

Outlet

Inlet

Periodic

Periodic

10% Span

Hub

LP part

Shroud

Rotor

Stator

Baumann rotor

Outlet

Periodic

Inlet

Periodic

Periodic

Hub
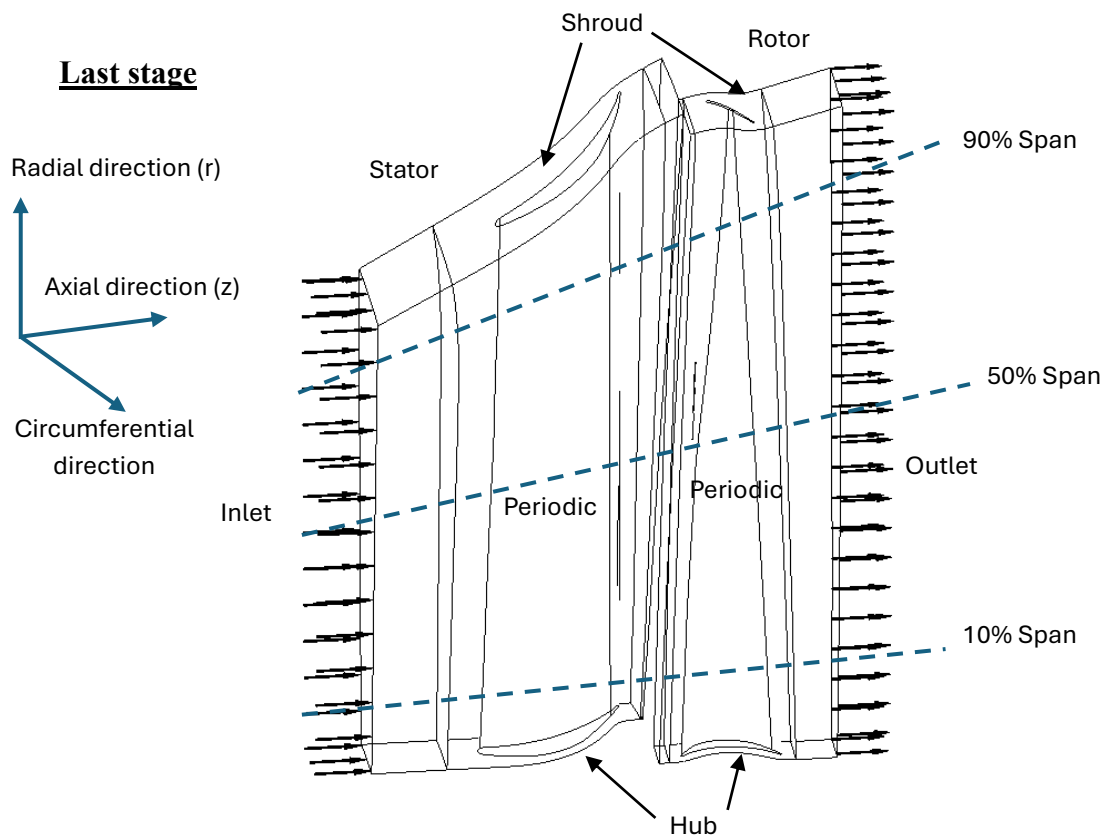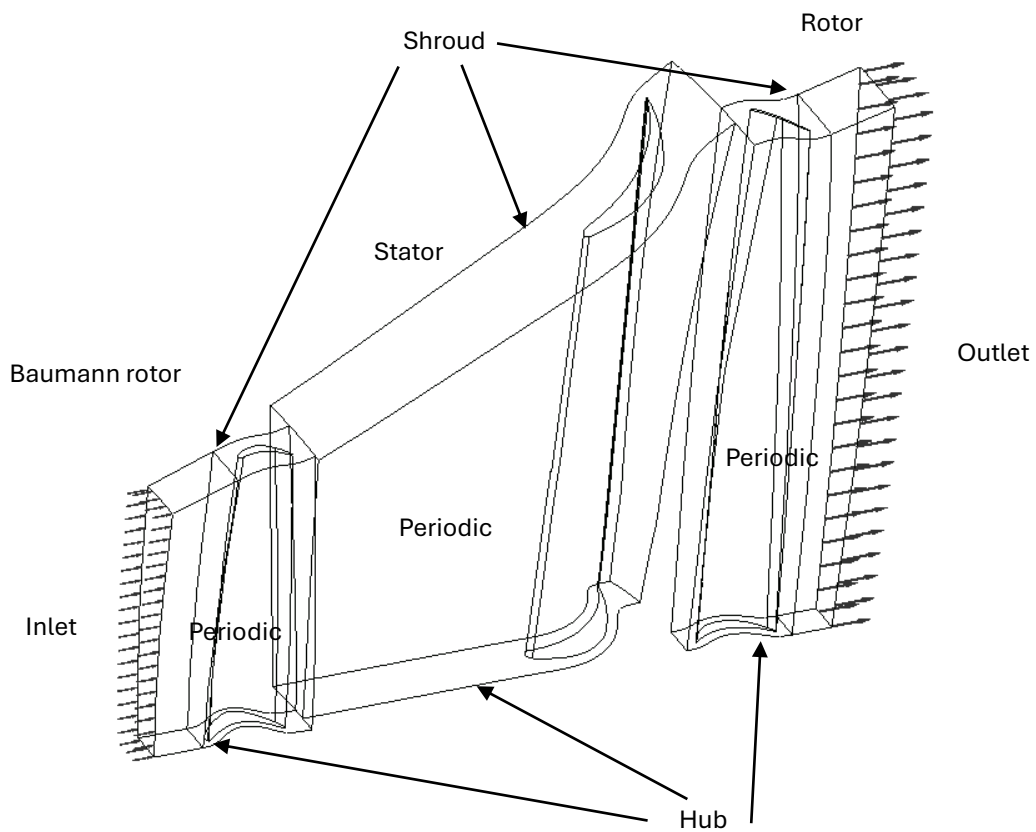
Fig. 4.6. Computational domain and boundary conditions.

4.4 Grid independence analysis

In this section, the grid independence results for the last stage were analyzed. To evaluate the grid independence of the solution, three different grids with varying element counts were selected, with their details provided in Table 4.2. After performing simulations using these three grids, the results at the stage outlet were compared, as shown in Fig. 4.7 and 4.8. The results from the fine and super-fine grids exhibited very close agreement, with only minimal differences. Given this strong consistency and to optimize both computational time and cost, the fine grid was chosen for all further calculations. Figure 4.9 presents the fine grid employed in the simulation for the last stage.

Table 4.2- Specifications of the grids

Grid type	Number of elements
Coarse	615k
Fine	1320k
Super fine	2277k
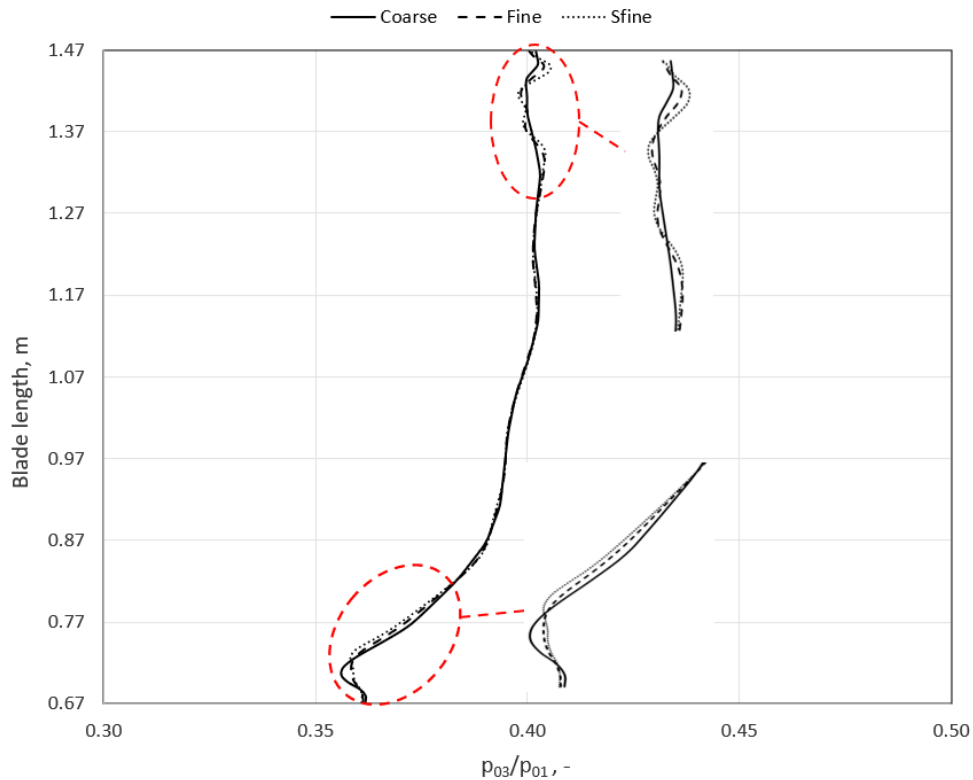
Fig. 4.7. Total pressure distribution at the stage outlet (radial direction)
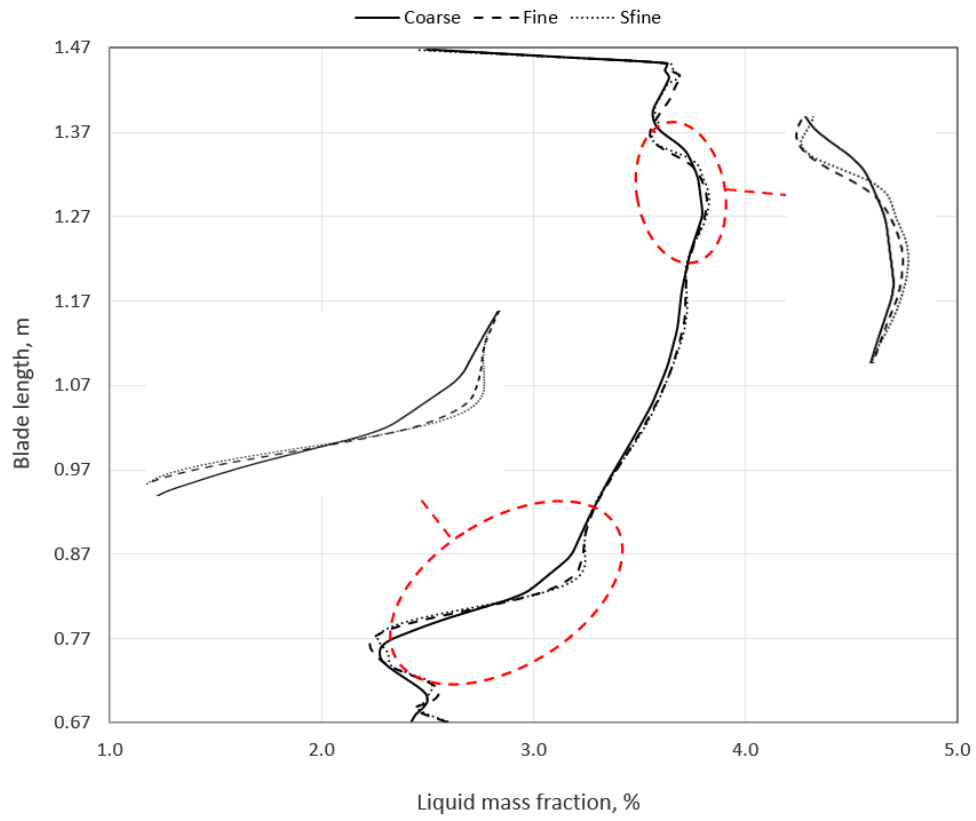
Fig. 4.8. Liquid mass fraction distribution at the stage outlet (radial direction)
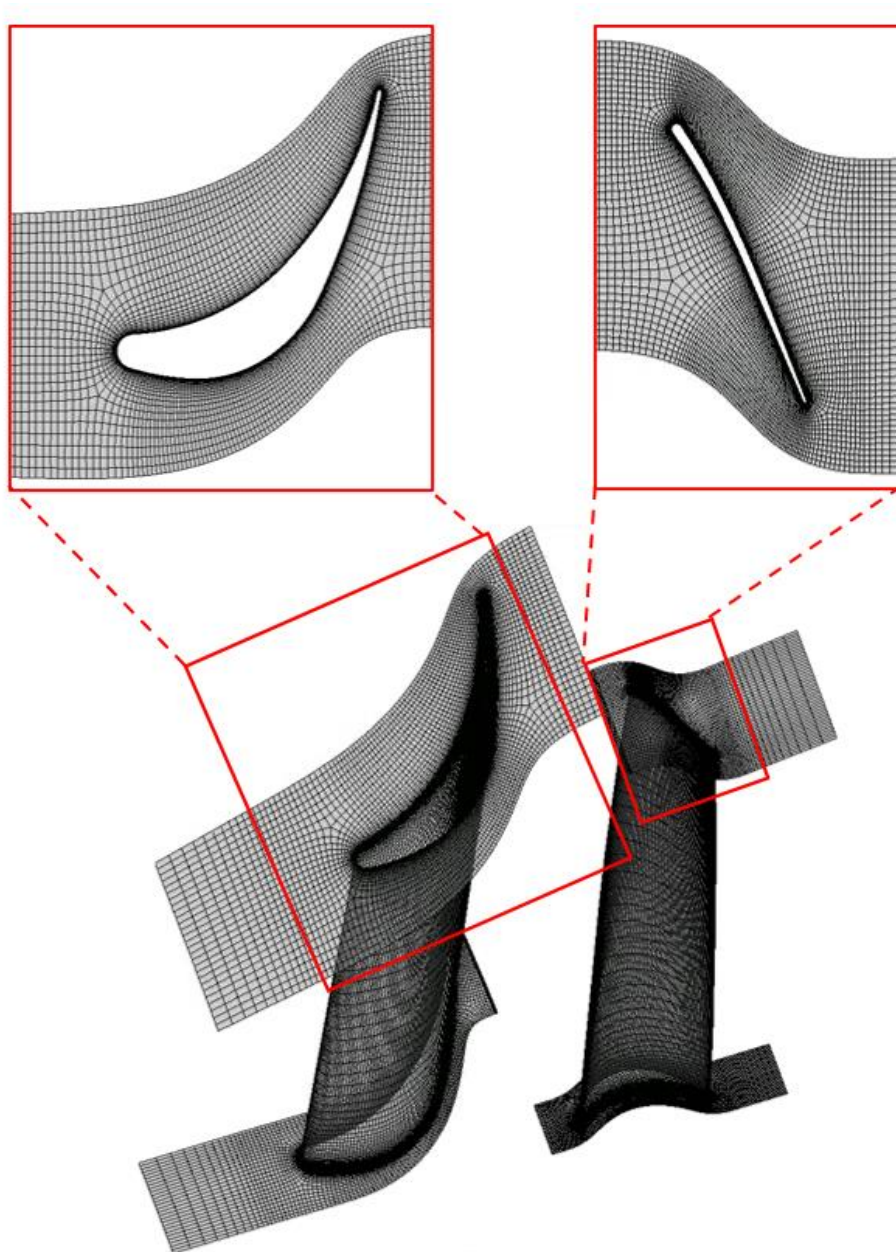
Fig. 4.9. Fine grid for the last stage

4.5 Results and discussion

In this section, the simulation results for the LP part and the last stage, and also the results for the losses are presented. To accurately compute losses, it's essential to account for parameters along the streamlines. However, in the case of 3-D blade-to-blade flow channels, identifying the exact streamlines can be quite challenging. As a result, losses are typically estimated using mass-averaged parameters at the inlet and outlet, instead of directly following streamlines. In condensing steam flows, both aerodynamic and thermodynamic losses occur simultaneously. In blade-to-blade channels, distinguishing between these two types of losses is nearly impossible, as they coexist and interact, with one type potentially amplifying or diminishing the other. Thermodynamic losses arise from phase changes (condensation) and the associated heat transfer. These losses tend to dominate and can lead to a significant increase in entropy. An isentropic flow, where no losses occur and entropy remains constant ($\Delta s=0$), represents an ideal but unattainable scenario. In contrast, diabatic flow includes both aerodynamic and thermodynamic losses, causing an entropy rise ($\Delta s>0$). In adiabatic flow, there is no heat transfer or phase change, so thermodynamic losses are absent, though entropy still increases due to aerodynamic losses alone ($\Delta s>0$).

4.5.1. Last stage of LP steam turbine

Figure 4.10 presents the absolute Mach number distribution along the stage at different span locations, specifically 10%, 50%, and 90% span. In the region between the stator blades, the flow remains subsonic (Mach < 1). As the flow reaches near the trailing edge of the stator, it accelerates, transitioning to supersonic speeds (Mach > 1), with the strongest effect observed near the hub. After entering the rotor passage, the Mach number gradually decreases, and by the time the flow reaches the exit, it returns to subsonic conditions.

Fig. 4.11 and 4.12 show the static pressure and static temperature distribution along the stage for different parts of span including 10%, 50% and 90% span. Comparing Fig. 4.10, 4.11 and 4.12, the following remarks may be concluded. In regions near the hub (10% span), since the stator acts like a converging-diverging nozzle in this area, the rate of flow expansion is greater compared to other regions (50% and 90% span). Due to this rapid expansion at the stator's trailing edge in the hub region, the flow velocity increases significantly, while pressure and temperature drop sharply. As a result, the steam crosses the saturation line and enters the two-phase region, where the temperature falls below the saturation temperature (T_s). In this condition, the liquid phase forms, and a wet steam two-phase flow is generated. For the rotor,

in areas near the shroud and on the suction side of the rotor, where the flow velocity is higher, the pressure and temperature experience a significant decrease, causing the liquid phase to appear in this region.
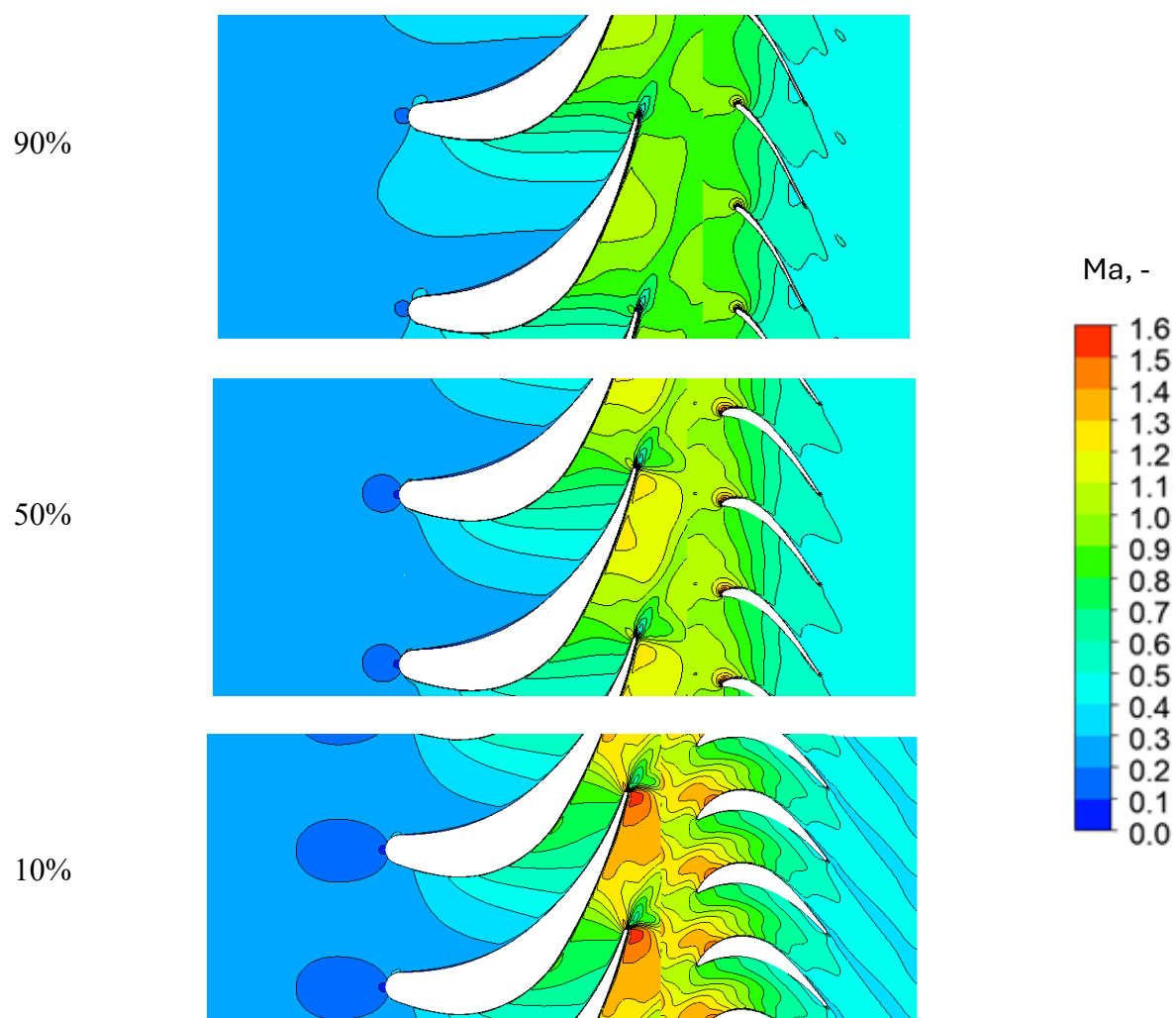
Fig. 4.10. Absolute Mach number distribution along the stage for different parts of span
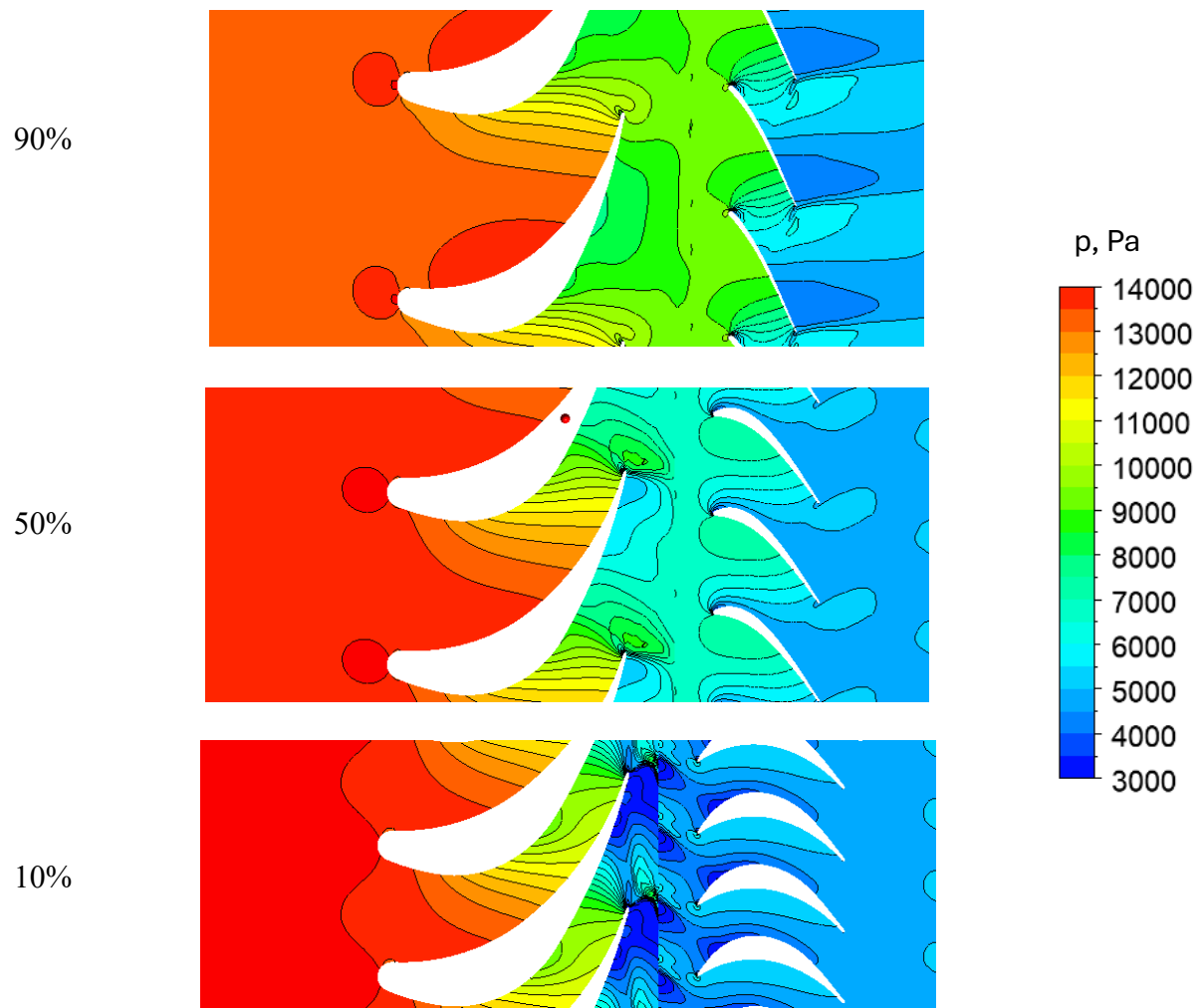
90%

50%

10%

p, Pa

14000
13000
12000
11000
10000
9000
8000
7000
6000
5000
4000
3000

Fig. 4.11. Static pressure distribution along the stage for different parts of span

90%

50%

10%

T, K

330
325
320
315
310
305
300
295
290
285
280
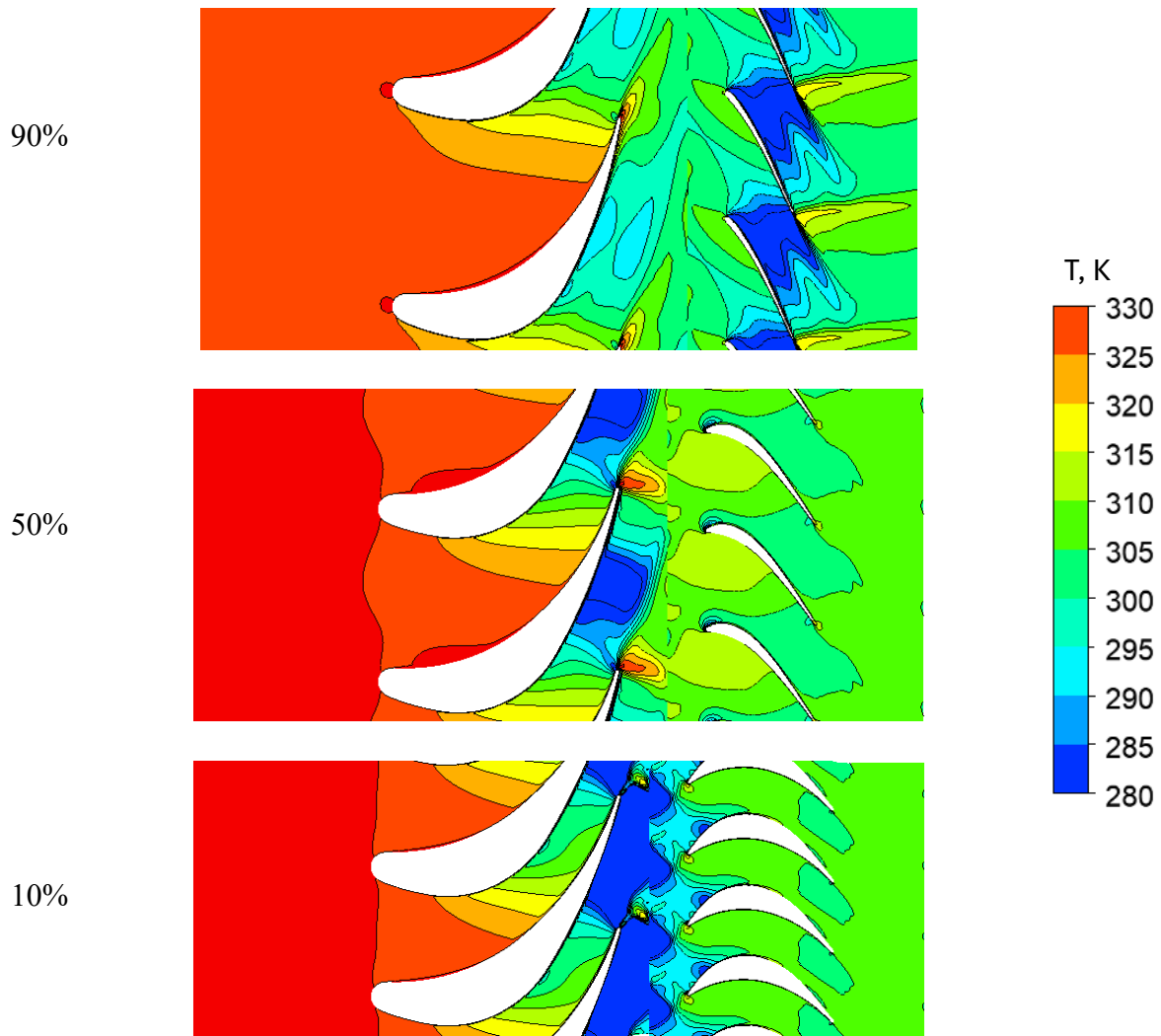
Fig. 4.12. Gas static temperature distribution along the stage for different parts of span

Fig. 4.13 shows the nucleation rate distribution along the stage for different parts of span including 10%, 50% and 90% span. As seen in this figure, and in line with previous explanations, it is expected that nucleation occurs at the stator's trailing edge near the hub and on the rotor's suction side near the shroud. This is clearly confirmed in the figure, highlighting the regions prone to nucleation.
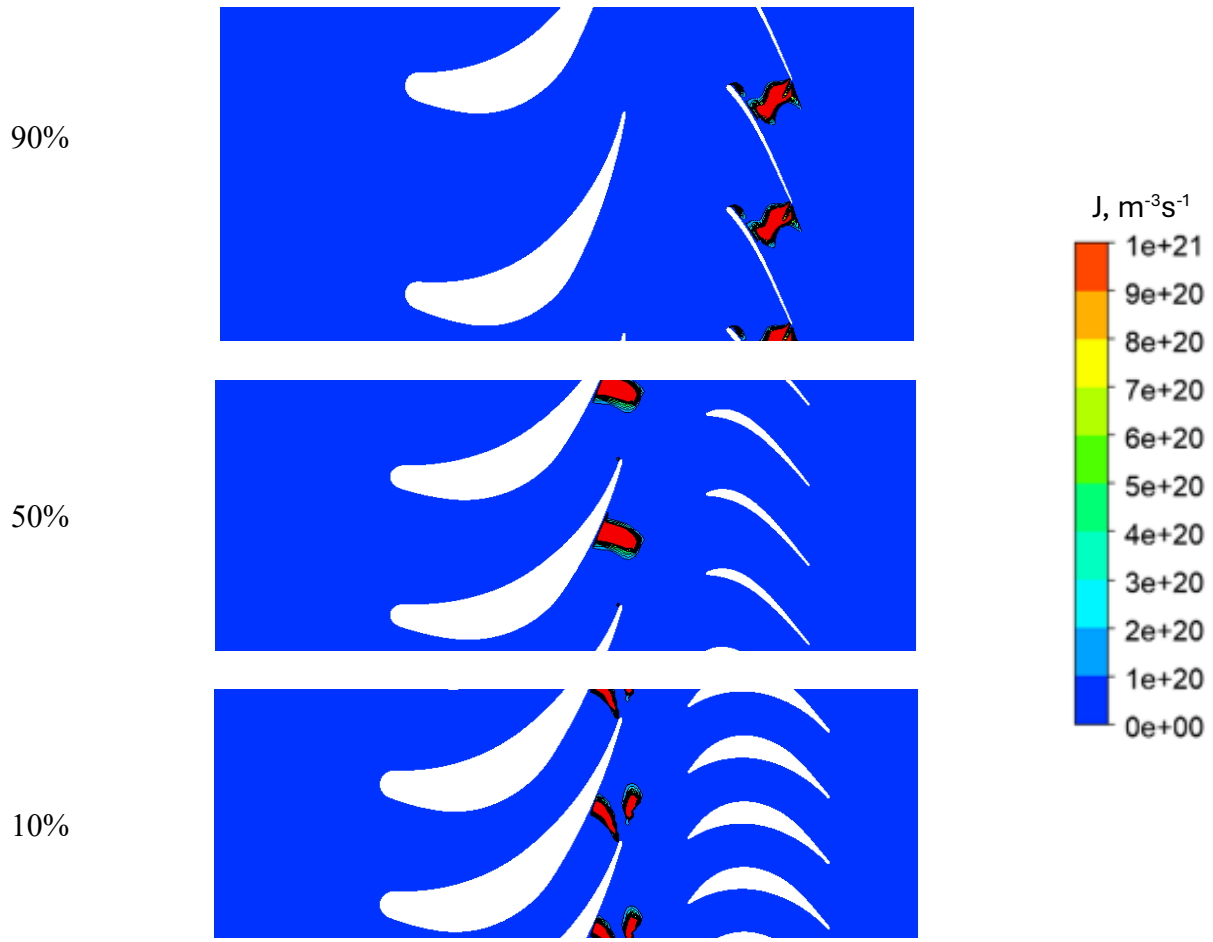
Fig. 4.13. Nucleation rate distribution along the stage for different parts of span

Figure 4.14 illustrates the liquid mass fraction along the stage at various span locations, including 10%, 50%, and 90% span. The liquid phase first appears at the stator's trailing edge, coinciding with the transition from subsonic to supersonic flow, and gradually increases toward the stage outlet. In certain regions at the stator's trailing edge (marked by black circles), a sharp rise followed by a drop in liquid mass fraction is observed. This is caused by the nucleation phenomenon, which significantly increases wetness. Following nucleation, some droplets grow while others evaporate, leading to a temporary decrease in liquid mass fraction due to evaporation. Eventually, when the number of droplets stabilizes, the liquid mass fraction steadily increases toward the stage outlet as the droplets continue to grow.

90%

50%

10%
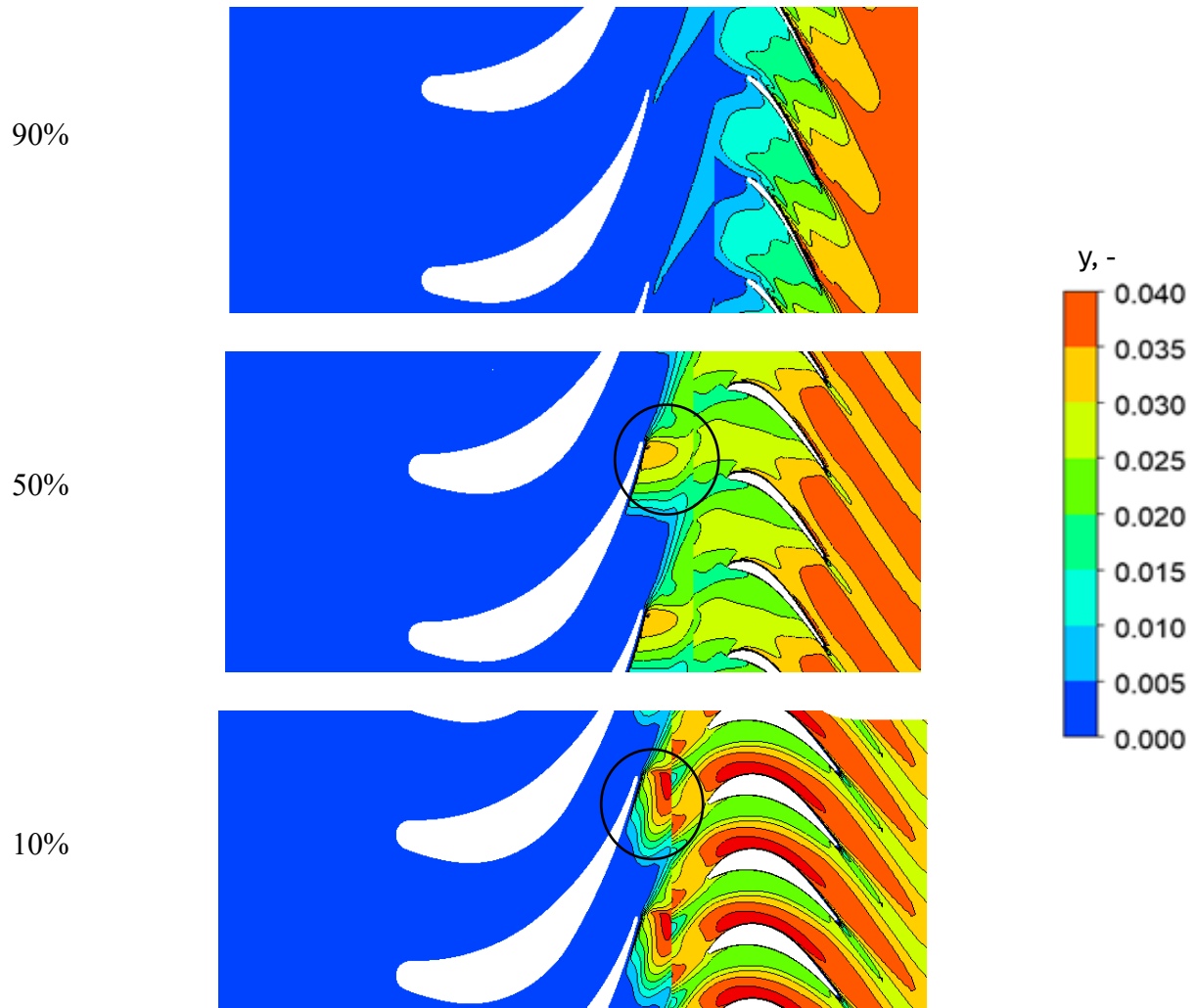
Fig. 4.14. Liquid mass fraction along the stage for different parts of span

Fig. 4.15 shows the average values of wetness generation along each component. As can be seen, the wetness increases by 1.5% along the stator and by 2% across the rotor, resulting in a total rise of 3.5% over the entire stage.

Figure 4.16 illustrates the contribution of each component to entropy generation, while Fig.4.17 presents the average values of entropy generation, entropy loss coefficients and isentropic efficiency in each component. From these two figures, it can be concluded that the highest entropy generation, and consequently the highest losses, occur in the same regions where phase change takes place in the stator and rotor. These regions are located near the hub in the stator and near the shroud in the rotor, as previously explained. Additionally, it is evident that entropy generation in the stator is greater than in the rotor. Therefore, it is expected that the largest portion of losses will occur in the stator, as shown in Fig. 4.17. To sum up, 10% of the losses occur in the stator, 1% in the rotor, and 11% in the entire stage, leading to a calculated stage

efficiency of 89%. Another conclusion that can be drawn is that the stator plays a crucial role in losses and determining stage efficiency, and as shown, the stage efficiency follows the efficiency of the stator.
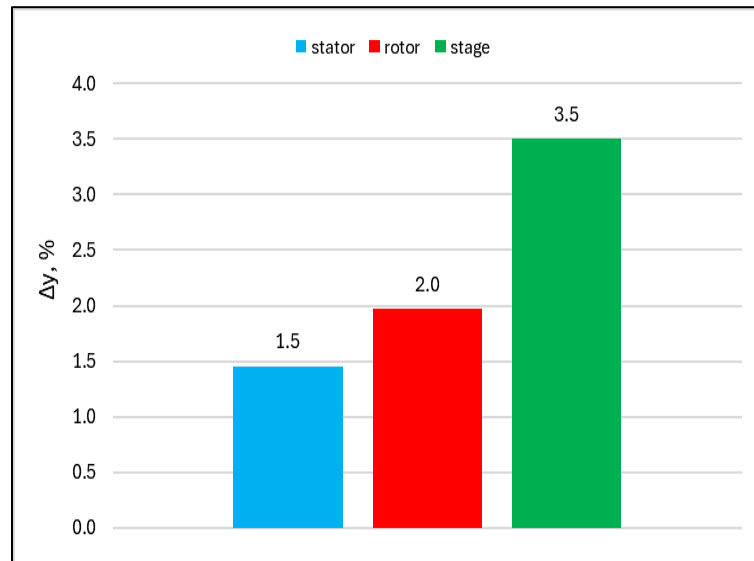
Fig. 4.15. The average values of wetness generation along the stator, rotor, and stage- refer to the mass fraction of water droplets formed as steam expands through these components
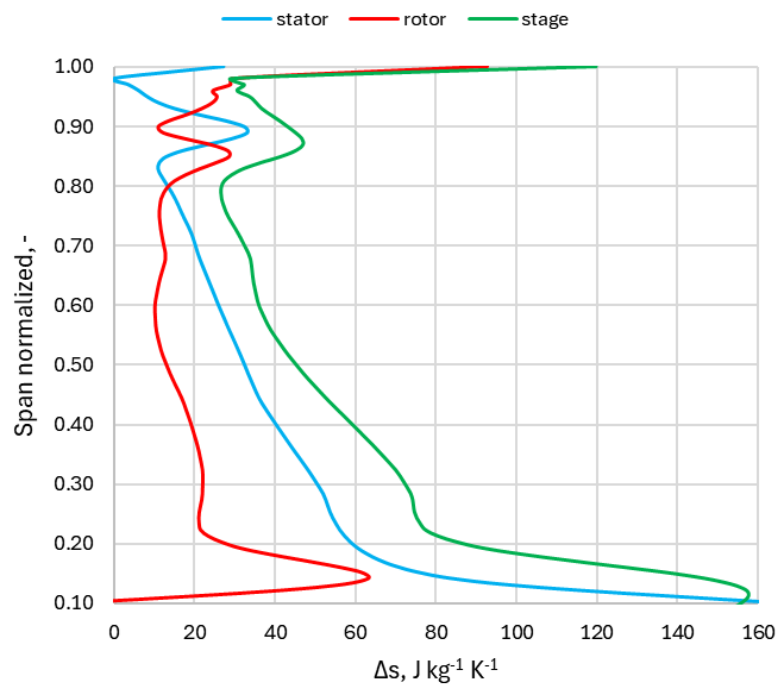
Fig. 4.16. Entropy generation along the stator, rotor, and stage
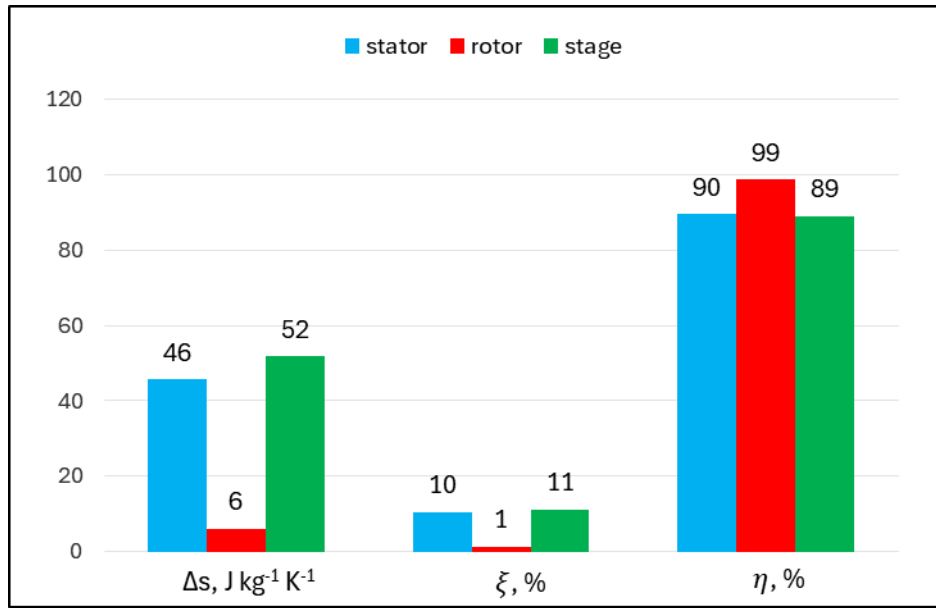
Fig. 4.17. The average values of entropy generation, entropy loss coefficients and
isentropic efficiency along stator, rotor and stage

4.5.2. Diabatic and adiabatic flow comparision

The aim of this section is to compare the results of the diabatic flow simulation with the results of the adiabatic flow, i.e., when no phase change occurs, in order to examine the impact of liquid phase formation on flow parameters. Fig. 4.18 illustrates the expansion process through the turbine stage for both diabatic and adiabatic flows. Point 1 marks the stage inlet, while point 3 indicates the stage outlet. In case of diabatic flow, the outlet temperature falls below the saturation temperature (T_s), causing the steam to enter the two-phase (supercooled) region, where condensation occurs. In contrast, during the adiabatic process, the outlet temperature remains above the saturation temperature.
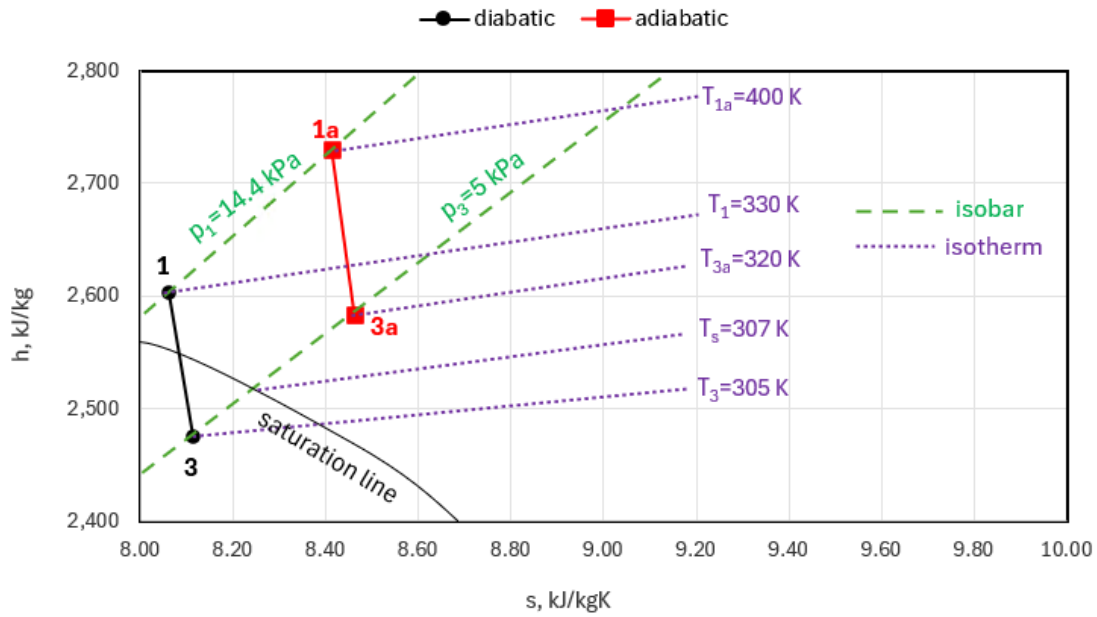
Fig. 4.18. Expansion process along the turbine stage for diabatic and adiabatic flows

Figure 4.19 illustrates the impact of steam condensation on static pressure across different sections of the span (10%, 50%, and 90%). In this chart, the values on the vertical axis have been normalized by the total pressure at the inlet (p_{01} = 14.4 kPa). For the stator, regions near the shroud (90% span) show little difference between the diabatic and adiabatic cases. However, near the stator hub (10% span) on the suction side, steam condensation causes the shock waves to be delayed and shift downstream. In the rotor, steam condensation on the suction side causes the shock waves to move upstream. Notably, for both the stator and rotor, condensation serves to strengthen the intensity of the shock waves.

Figure 4.20 depicts the influence of steam condensation on the Mach number across various span sections (10%, 50%, and 90%). The most pronounced differences between the diabatic and adiabatic Mach contours are observed near the hub (10% span), specifically at the trailing edge of the stator and the suction side of the rotor, which corresponds to the areas with the highest wetness values. In these regions, condensation significantly reduces the Mach number, leading to a decrease in flow velocity. This highlights the substantial effect of condensation on flow parameters and emphasizes the necessity for a comprehensive investigation of this phenomenon.
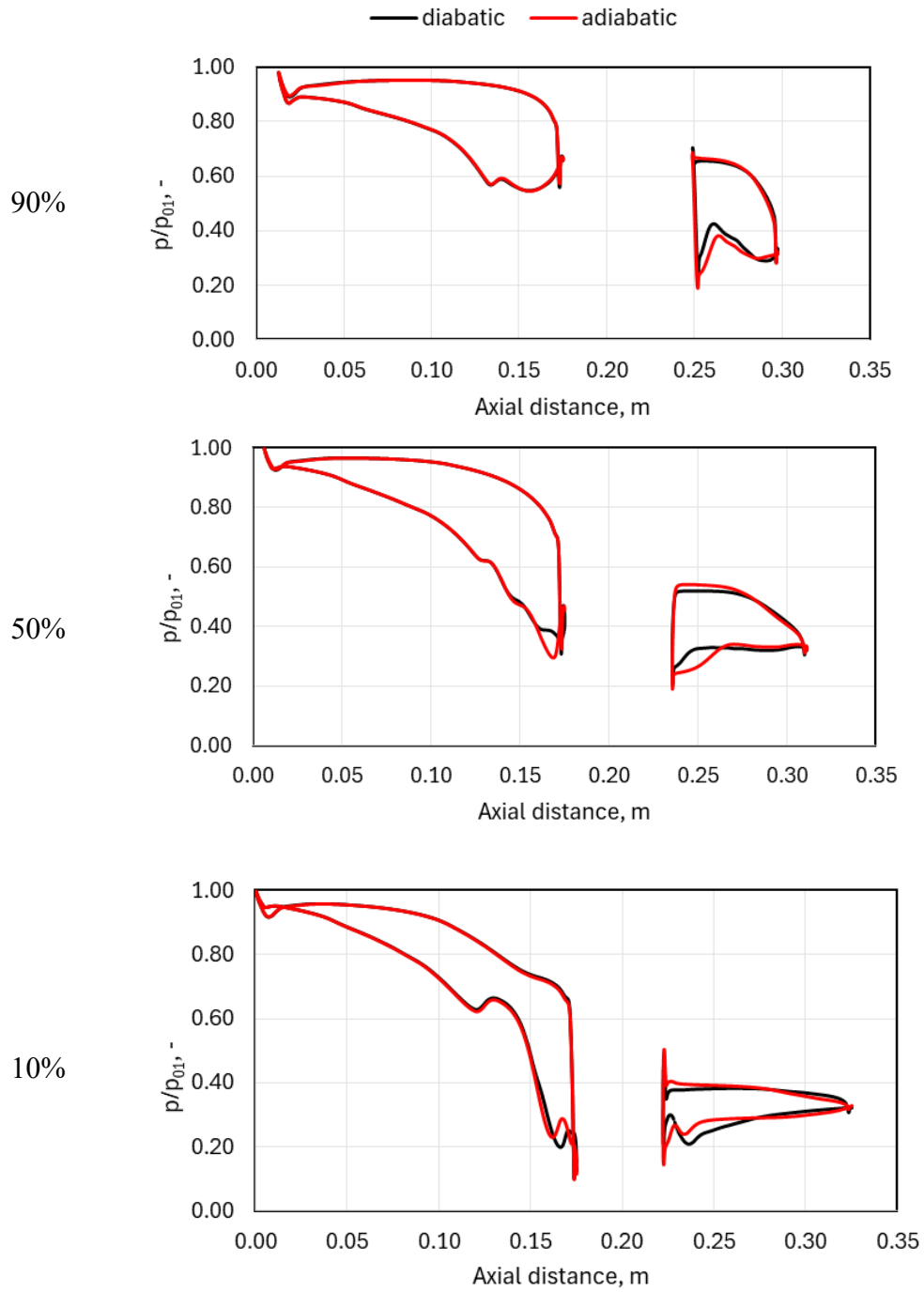
Fig. 4.19. Static pressure distribution on the blades for diabatic and adiabatic flows (axial direction)
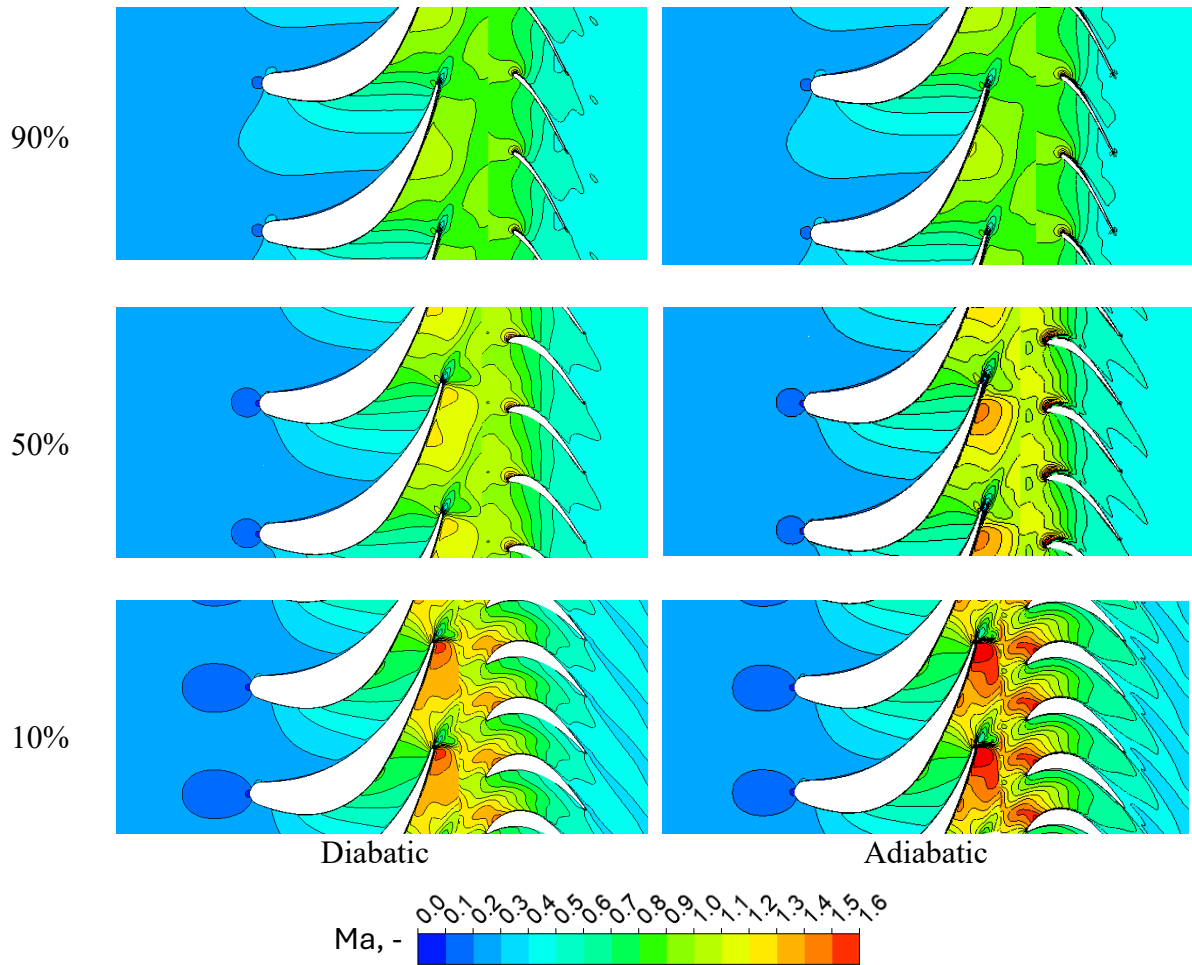
Fig. 4.20. Absolute Mach number distribution for different sections of span under diabatic and adiabatic flow conditions

Figure 4.21 depicts the influence of steam condensation on the exit flow angle at the stator and rotor outlet. At the stator outlet, there is little distinction between the diabatic and adiabatic cases. However, at the rotor outlet, the flow angle in the diabatic case is smaller compared to the adiabatic case. This indicates that condensation results in a reduction of the exit flow angle.

In this section, calculation of the values of entropy generation, losses, and efficiency for the adiabatic flow was made and compared with the results of the diabatic flow. Fig. 4.22 shows the averaged values of entropy generation, entropy loss coefficient, isentropic efficiency and the output power for diabatic and adiabatic cases. Table 4.3 summarizes these results and expresses the differences between the cases as percentages. As can be seen, steam condensation causes entropy generation and losses to increase by 2.39% and 11.65% respectively, compared to the adiabatic case, while the stage efficiency and output power decrease by 1.27% and

15.04%, respectively. These cases clearly demonstrate the substantial and negative impact of condensation, which diminishes both the turbine's efficiency and its output power.

Stator outlet   Rotor outlet
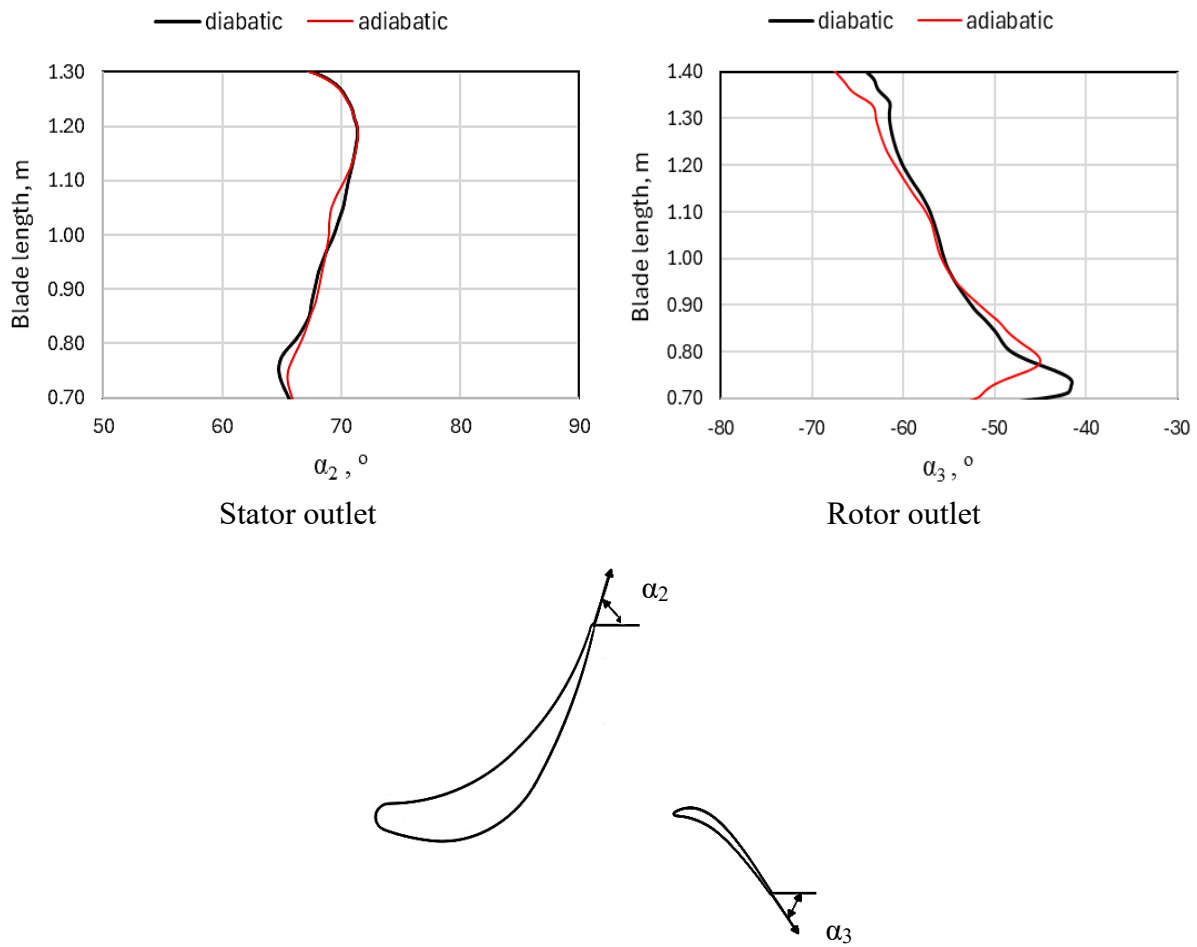
Fig. 4.21. Mean outlet flow angle for diabatic and adiabatic flows (radial direction)
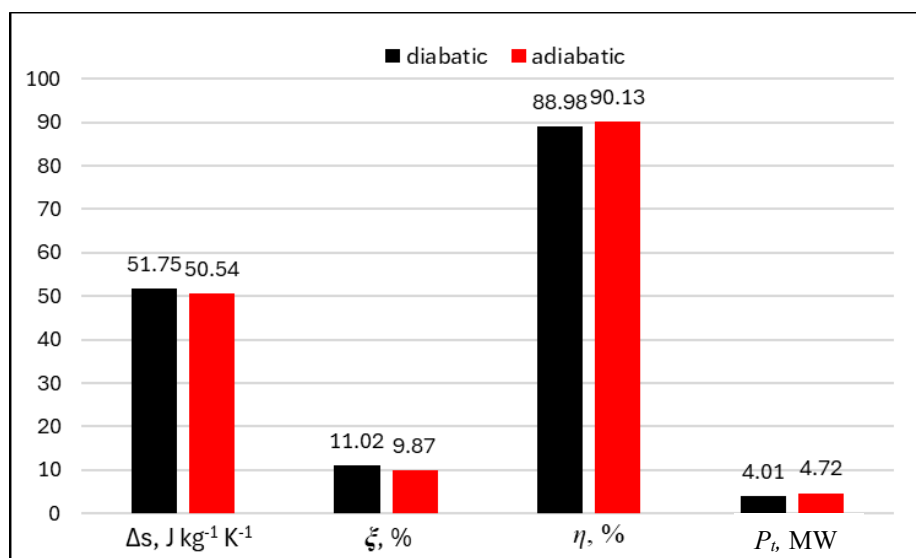
Fig. 4.22. The average values of entropy generation, entropy loss coefficient, isentropic efficiency and output power for diabatic and adiabatic flows

Table 4.3- The averaged values of entropy generation, entropy loss coefficient, isentropic efficiency, and power along the stage for diabatic flow compared to the adiabatic flow

	Δs	ξ	η	P_t
Diabatic flow	51.75 J kg^{-1} K^{-1}	11.02 %	88.98 %	4.01 MW
Adiabatic flow	50.54 J kg^{-1} K^{-1}	9.87 %	90.13 %	4.72 MW
Difference (%)	+2.39 %	+11.65 %	-1.27 %	-15.04 %

4.5.3. LP section of steam turbine

In this section, the results of the LP section of the steam turbine were analyzed and then compared with the results of the last stage (section 4.5.1). The LP section of the turbine includes the Baumann rotor and the last stage, with the inlet boundary conditions set so that the entire last stage operates in a wet condition. However, in section 4.5.1 (where only the last stage is considered), wetness begins at the trailing edge of the stator.

Figure 4.23 shows the contour of the absolute Mach number for different span sections. As observed, near the hub, the flow velocity significantly increases at the stator's trailing edge. Figure 4.24 displays the contour of the liquid mass fraction for various span sections. Wetness starts at the Baumann rotor's trailing edge and continuously increases toward the outlet. Near the hub, a notable increase in wetness is observed at the stator's trailing edge, which is due to secondary condensation.

Figure 4.25 shows the specific entropy from the inlet to the outlet for two cases: LS and LP. LS refers to the case where only the last stage is considered, while LP represents the case where the last stage and the Baumann rotor are both considered. As observed in the figure, the entropy rise along the stator in the LP case (where the entire last stage is in a wet condition) is significantly higher compared to the LS case, and it is because of secondary condensation at the stator's trailing edge, which explained earlier. And this can impact on the entropy generation and losses. Figures 4.26 and 4.27 show the spanwise distribution of entropy generation and losses for cases LS1 and LS2. LS1 represents the case where only the last stage is considered, while LS2 refers to the case where the last stage is simulated in combination with the Baumann rotor. The amount of entropy generation and losses in case LS2 is significantly higher than in LS1, which is due to secondary condensation that creates a sharp entropy difference along the stator. Figure 4.28 presents the average values of entropy generation, losses, efficiency, and

output power for the last stage in cases LS1 and LS2. The efficiency and output power in case LS2 are significantly lower compared to case LS1.

90%

50%

10%
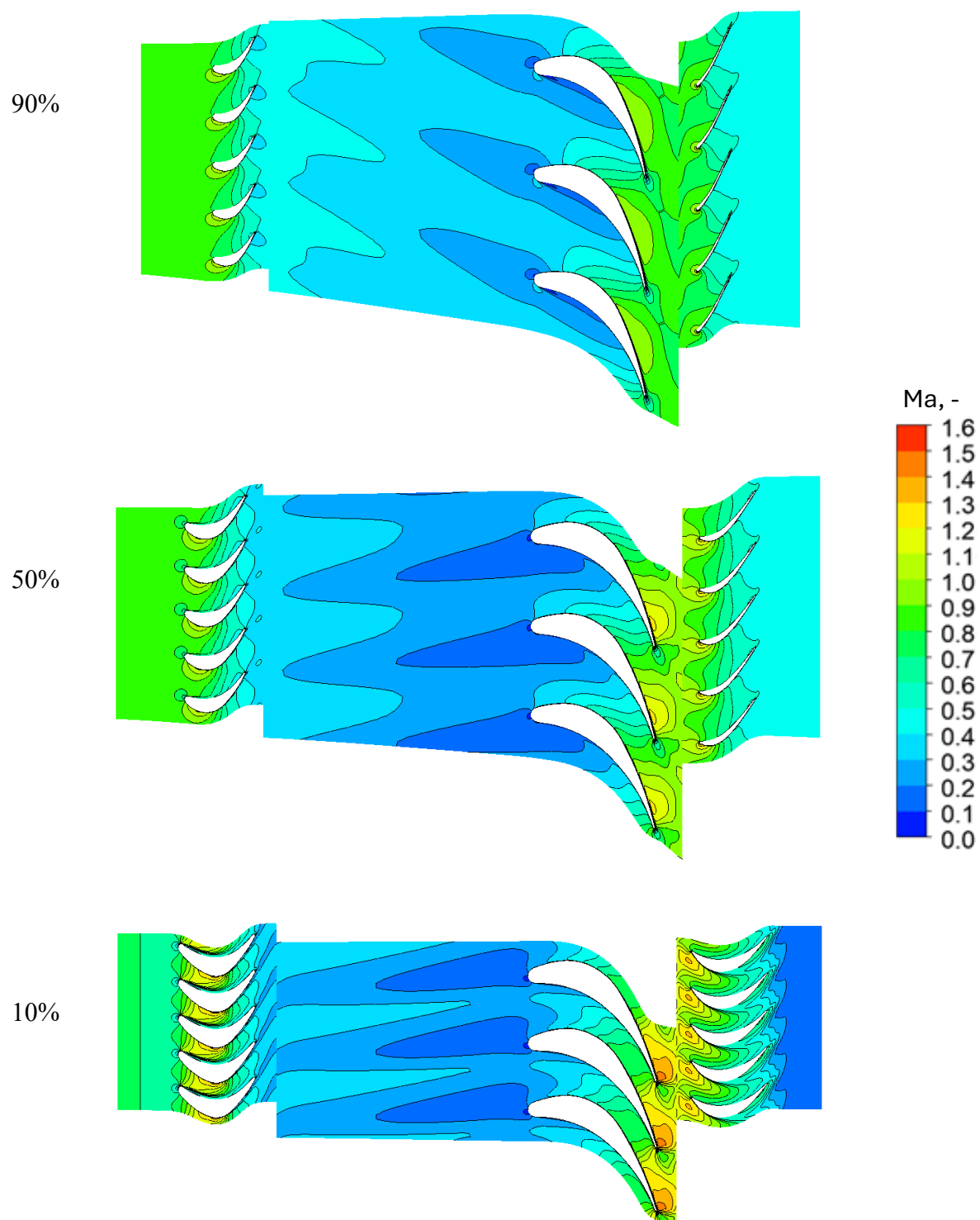
Fig. 4.23. Absolute Mach number distribution along the LP part for different parts of span
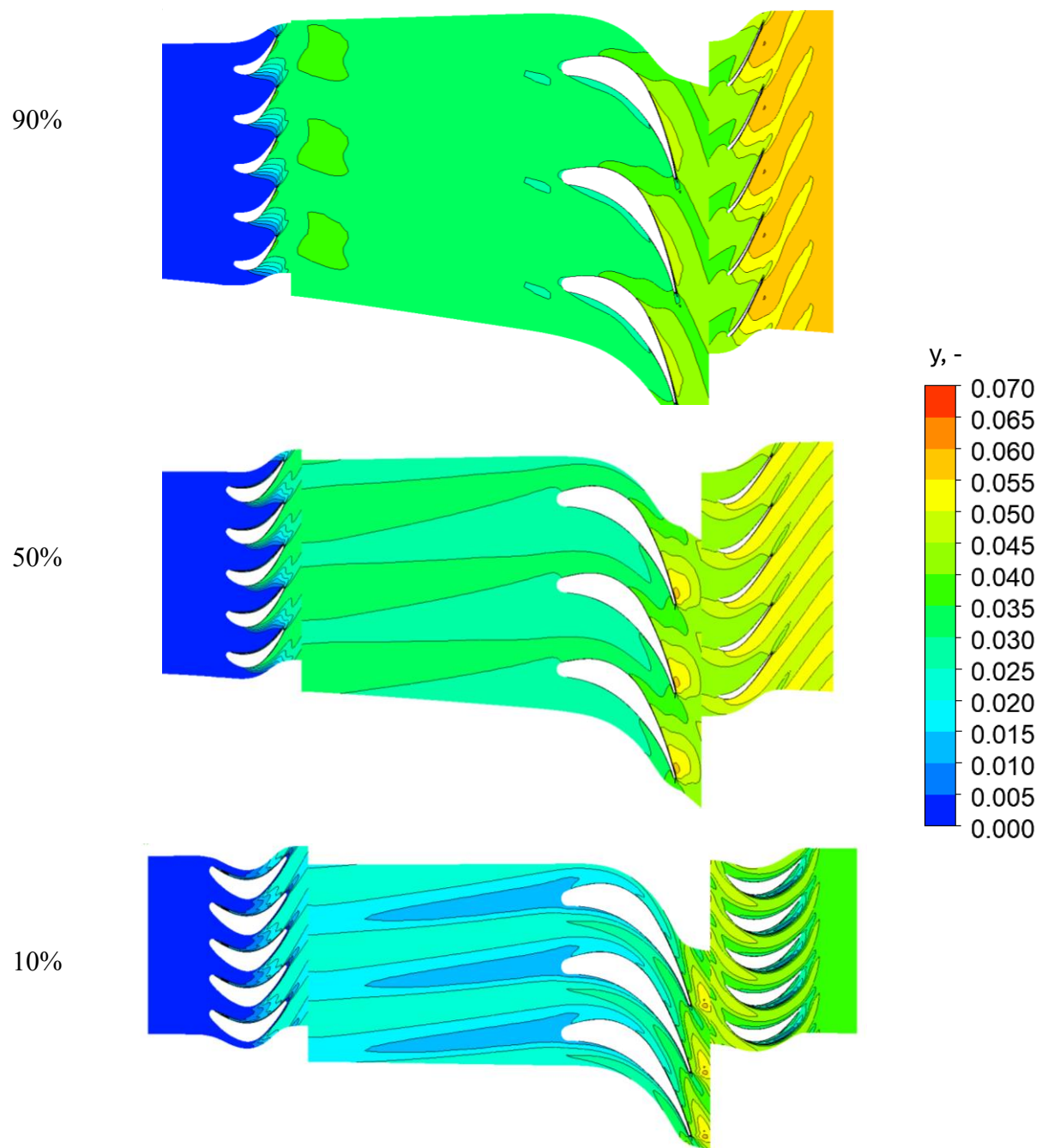
Fig. 4.24. Liquid mass fraction along the LP part for different parts of span
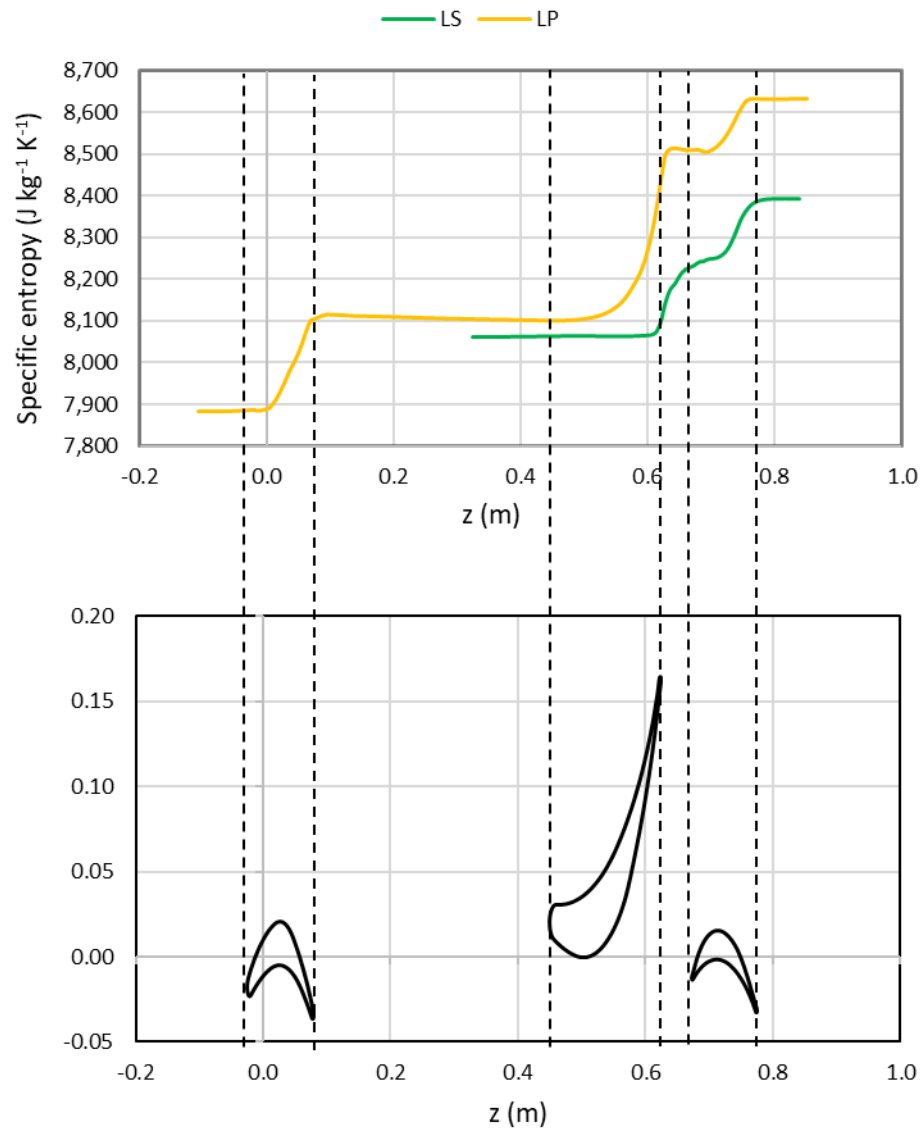
Fig. 4.25. Specific entropy from inlet to outlet- LS vs LP
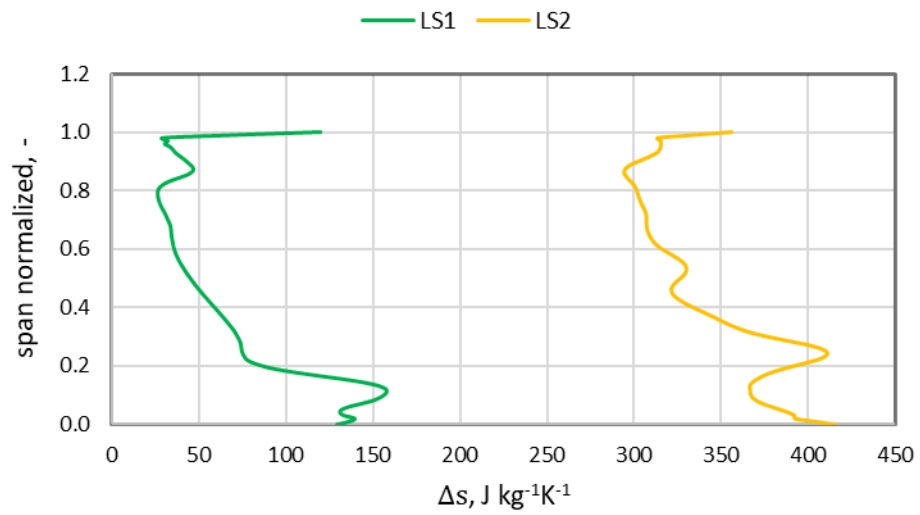
Fig. 4.26. Spanwise distribution of entropy generation along the last stage- LS1 vs LS2
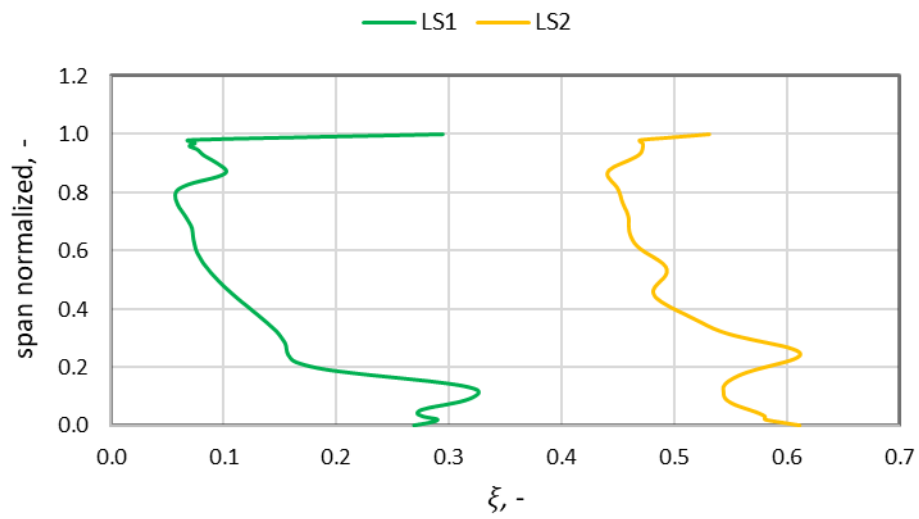
Fig. 4.27. Spanwise distribution of loss coefficient along the last stage- LS1 vs LS2
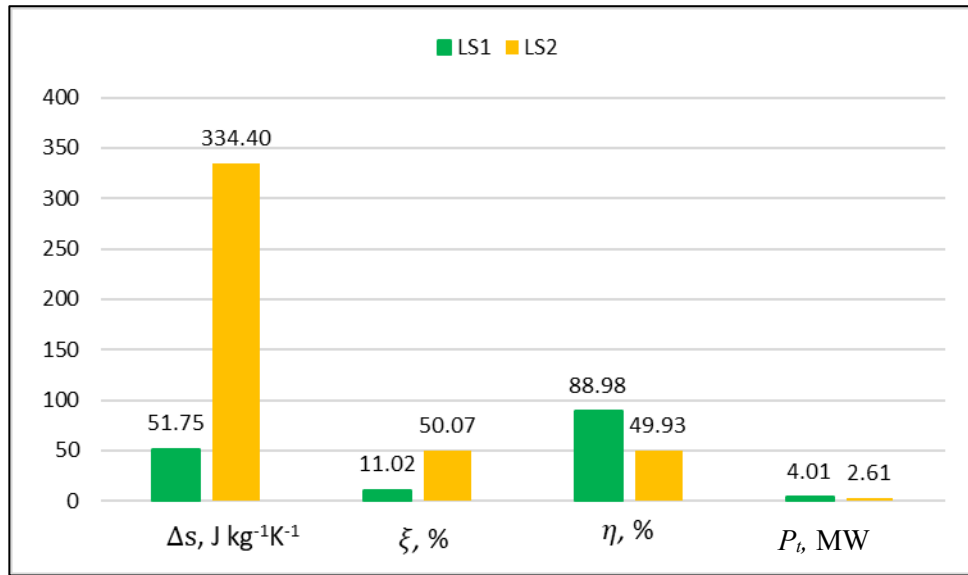
Fig. 4.28. The average values of entropy generation, entropy loss coefficient, isentropic efficiency and output power- LS1 vs LS2

4.6 Conclusions

The numerical simulation of wet steam flow in the low-pressure section of a steam turbine was conducted. The primary focus of the study was to predict the behavior of wet steam flows while estimating efficiency and losses. The objective was to employ accurate CFD models that effectively capture the complex three-dimensional steam flow conditions within the real LP turbine geometry. The results were then compared to those from adiabatic flow, where condensation is absent, to emphasize the substantial impact of steam condensation on various flow parameters. In conclusion, the following remarks can be made:

- when the last stage considered alone,

    - condensation occurs at the stator trailing edge in the region close to the hub, and in the suction side of rotor, in the region close to the shroud,
    - max entropy rise occurs at the stator hub and at the rotor shroud, so in these regions the highest amount of losses can be seen,
    - along the stator, more entropy rise occurs than along the rotor, so the max amount of losses occurs along the stator,
    - 10% of losses occur along the stator and 1% along the rotor, and a total of 11% of losses occur along the entire stage. And finally, the efficiency of the stage is calculated to be 89%.

- comparison with adiabatic flow,

  - near the stator hub, condensation on the suction side causes a delay in the shock waves, pushing their position downstream. In contrast, on the rotor's suction side, condensation shifts the shock waves upstream. Notably, in both the stator and rotor, the presence of condensation increases the intensity of the shock waves,
  - in regions with the highest levels of wetness, the occurrence of condensation significantly lowers the Mach number, which in turn reduces the flow velocity,
  - condensation also impacts the outlet flow angles by decreasing the exit flow angle at the rotor outlet,
  - condensation generally decreases the turbine's efficiency and results in a reduction of the turbine's output power. For the analyzed configuration, it was 1.27% for efficiency and 15.04% for power, respectively.

- the last stage considered together with Baumann rotor (LP section),
  - In this case, the entire last stage was set to operate in wet conditions. Secondary condensation occurs in the stator trailing edge, which causes a significant entropy generation and additional losses. In this case, the resulting losses led to reduced efficiency and output power. However, the severity of this impact may vary with different operating conditions.

The above remarks highlight the substantial effects of steam condensation on the flow within steam turbines, leading to changes in flow parameters, increased losses, and decreased efficiency. Accurate simulations of these flows, particularly in complex three-dimensional geometries, yield more realistic results. The accurate calculation of losses in these flows is vital, as it serves as a foundation for implementing effective strategies aimed at reducing losses and enhancing the efficiency of steam turbines.

5. Assessing Stage Performance Sensitivity to Minor Variations in Stator Blade Configurations

The performance sensitivity of a steam turbine stage to small variations in stator blade configurations, specifically within the final stage of a 200 MW turbine will be evaluated. Using advanced CFD simulations, modeling of wet steam two-phase flow around the stator blades will be made. These simulations capture critical flow dynamics, such as pressure distributions, flow patterns, and energy losses, which are instrumental in optimizing blade design. Building on insights from previous chapters, where the significant influence of the stator on overall stage efficiency and losses was established, this chapter investigates how minor changes to stator geometry affect the rotor and the entire stage performance.

By introducing small modifications to the stator configuration, the impact on turbine efficiency, flow behavior, and overall stage performance is investigated, providing key insights into design improvements for enhanced turbine operation. The geometry examined in this research is the real 3D geometry of the final stage of the steam turbine (Fig.5.1), which was analyzed in the previous chapter. In this chapter, primary focus is on the stator blade.
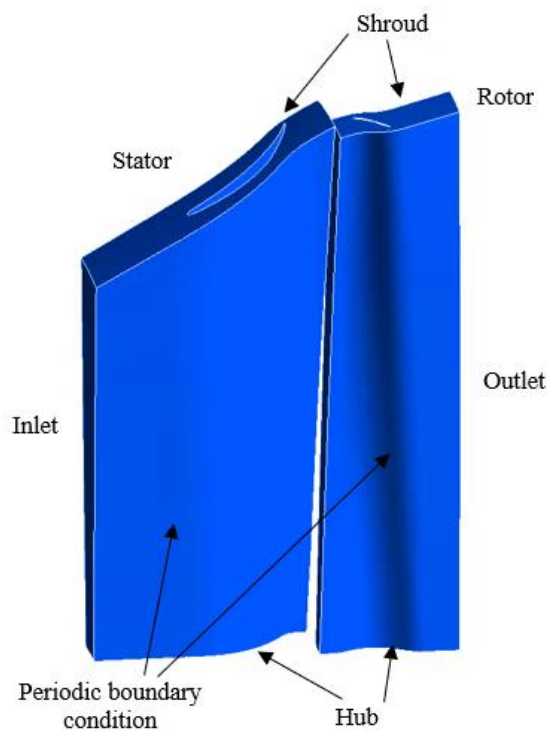
Fig. 5.1. Computational domain

5.1 2D modification of the stator blade configuration

Investigation of the effect of the twist of the blade profile along the span, number of blades in a row (the pitch size), change of the blade profile, and the rotation of the blade, on the entire stage parameters will be presented. The boundary conditions and numerical setup remain the same as in the previous chapter for the last stage case. Hence, details about the numerical method are avoided here, with emphasis placed on the simulation results.

5.1.1. The effect of the twist of the blade profile along the span

The original 3D blade profile of the stator consists of 8 profiles in the radial direction, as shown in Fig.5.2. The profile number 1 is close to the hub and profile number 8 is close to the shroud. The goal of this section is to assess the effect of the twist of the blade along the span, so that new profile choosing the 4th and the 8th profile is created. Therefore, for the region close to the shroud there is no difference between the new and the original profile, as both use the profile number 8. However, for the region close to the hub, the profiles are given in Fig. 5.3.

Fig. 5.4 shows the effect of the new profile on the flow angles and velocities at the stator-rotor interface. The velocity triangles are according to Fig. 4.1. The effect is more significant in the hub region, as expected. In this region, the velocity magnitude decreases while the flow angle increases. As a result, the flow moves at a lower speed and strikes the rotor blade at a steeper angle. Fig. 5.5 shows the effect of the new profile on the mass flow rate and the output power. The output power is dependent on two parameters, mass flow rate and the total enthalpy change, as explained in the previous chapter. As can be seen in this figure, for the region close to the hub, the channel area between two blades decreases in the new profile compared to the original one, so that the mass flow rate and the output power decrease in the new profile. As shown in Fig. 5.6, which illustrates the effect of the new profile on the wetness fraction, wetness increases at the stator outlet, but ultimately decreases at the stage outlet. The reduction in wetness is more pronounced in the regions near the hub. The increase in wetness at the stator outlet, is because the expansion rate increases in the stator channel for the new profile, according to Fig.5.3.
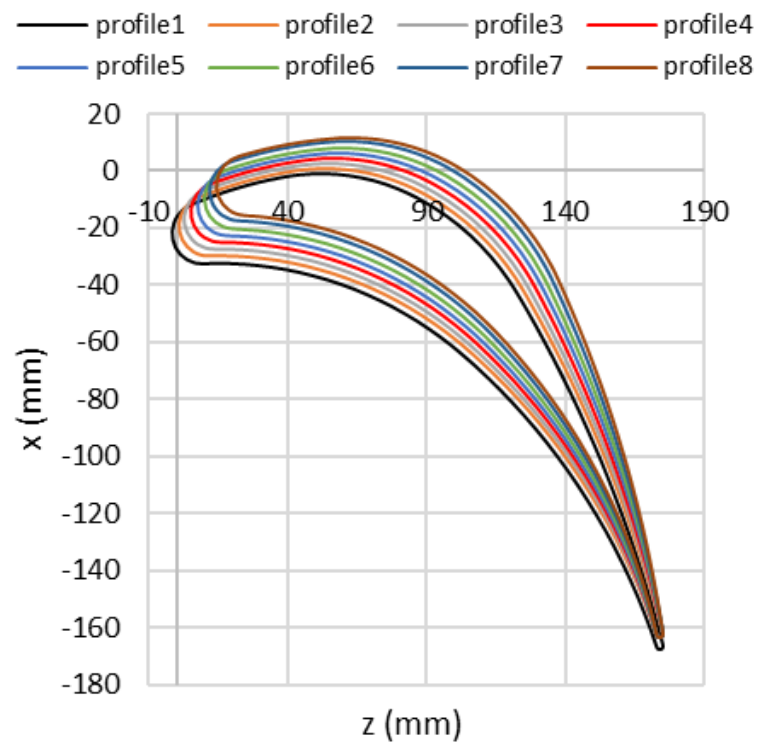
Fig. 5.2. Stator blade profile with 8 blades in the radial direction
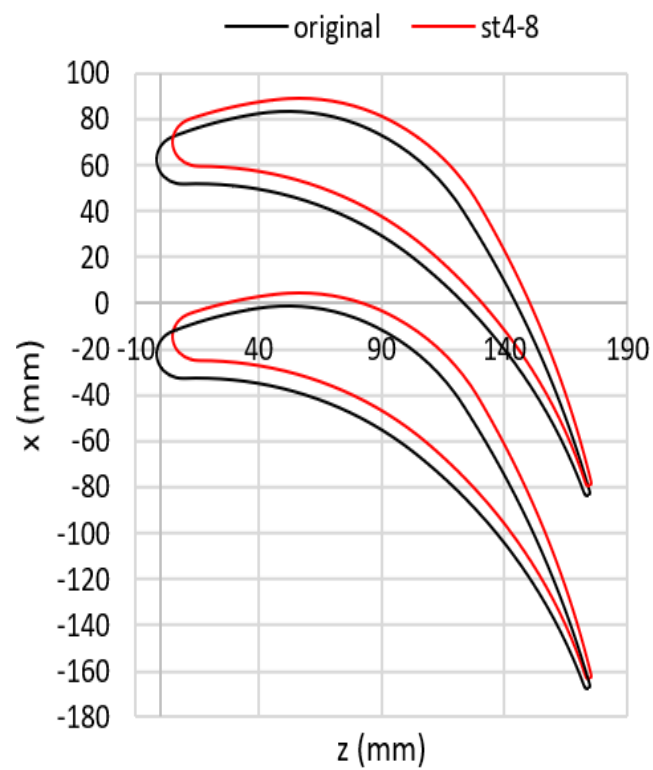
Fig. 5.3. Comparison of blade profiles near the hub: Original vs. new profile
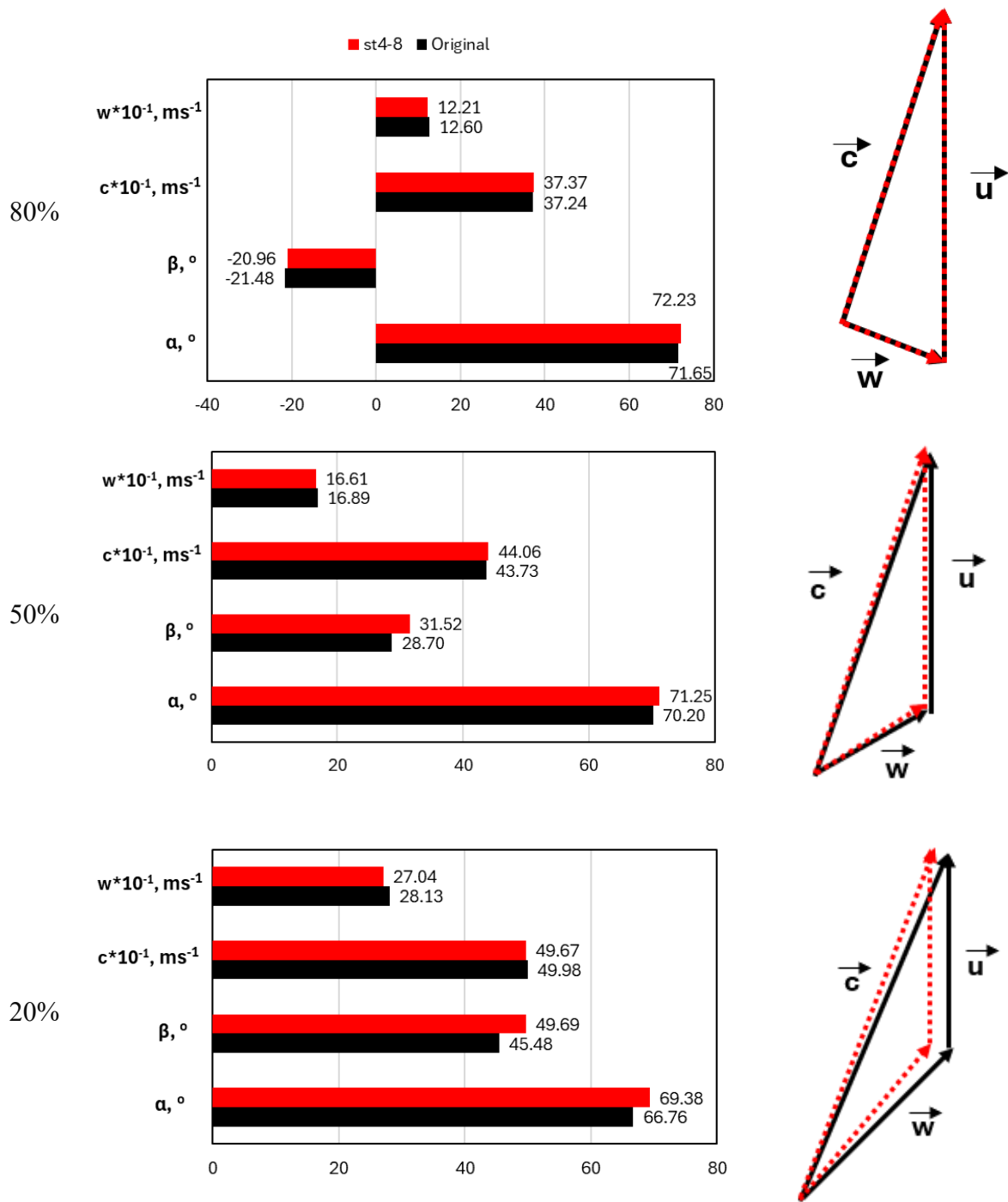
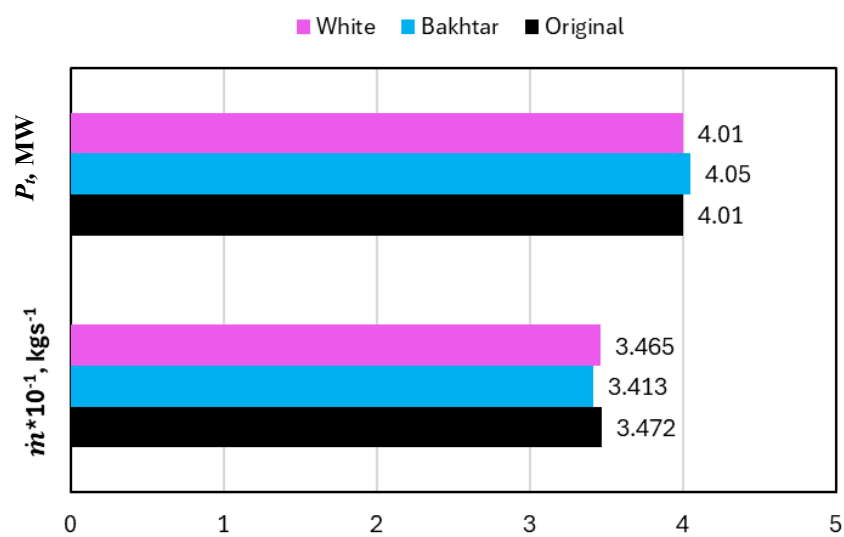Fig.5.4. Flow angles and velocities at the stator-rotor interface
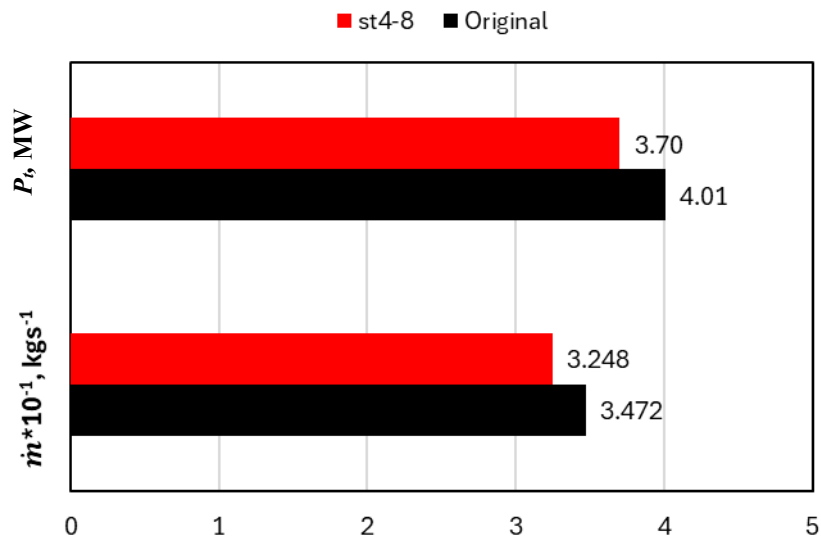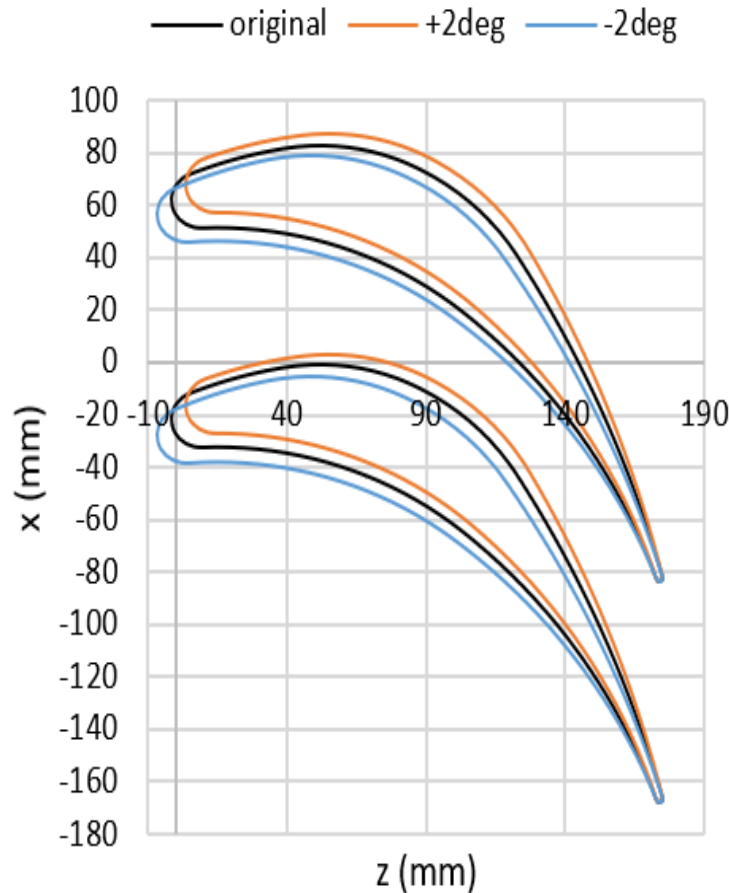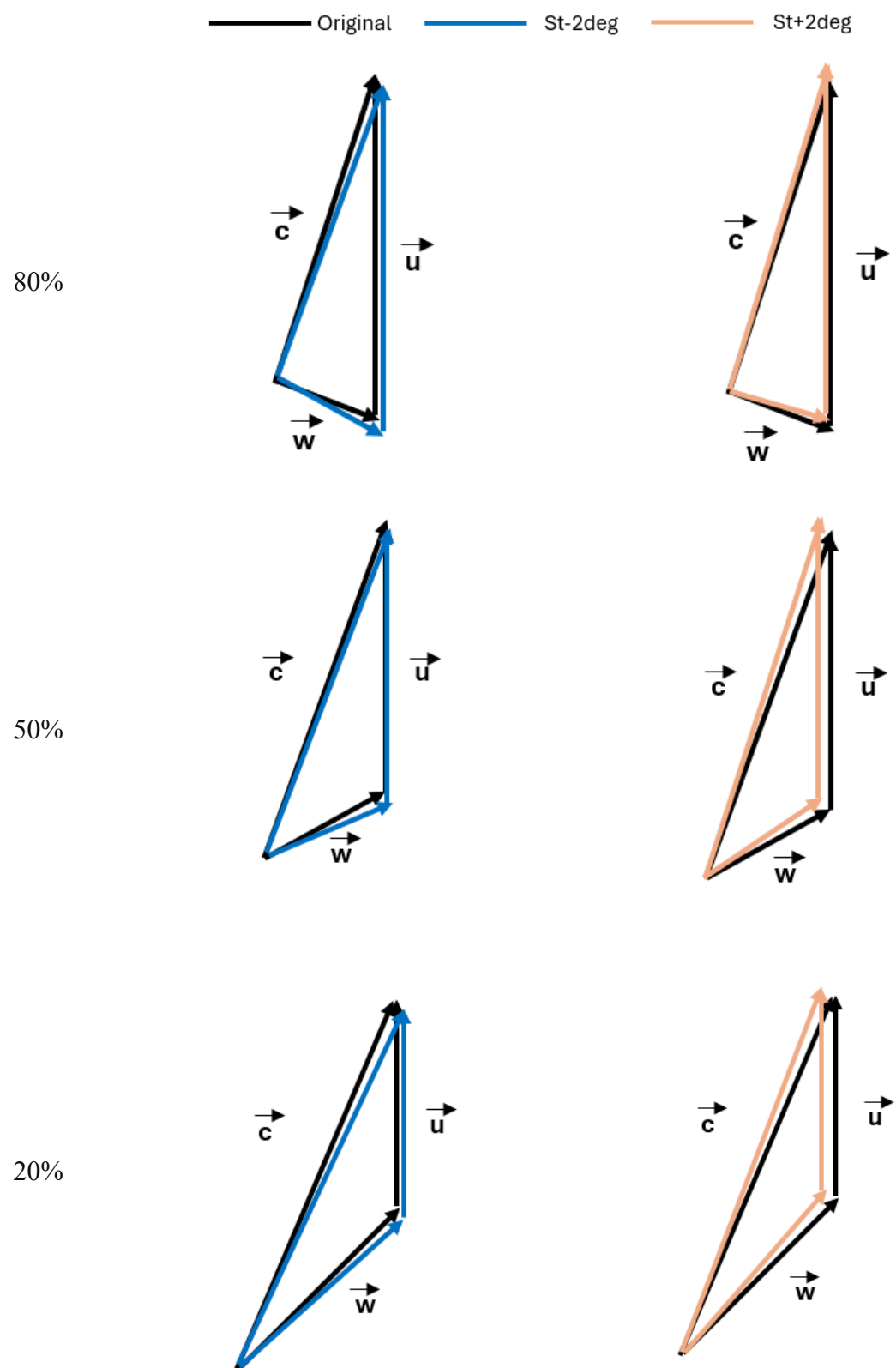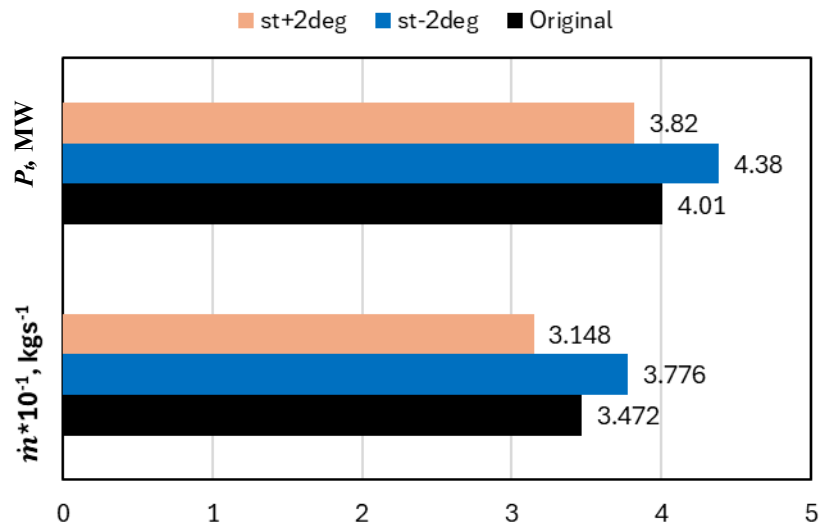
Fig.5.5. Average mass flow rate and output power
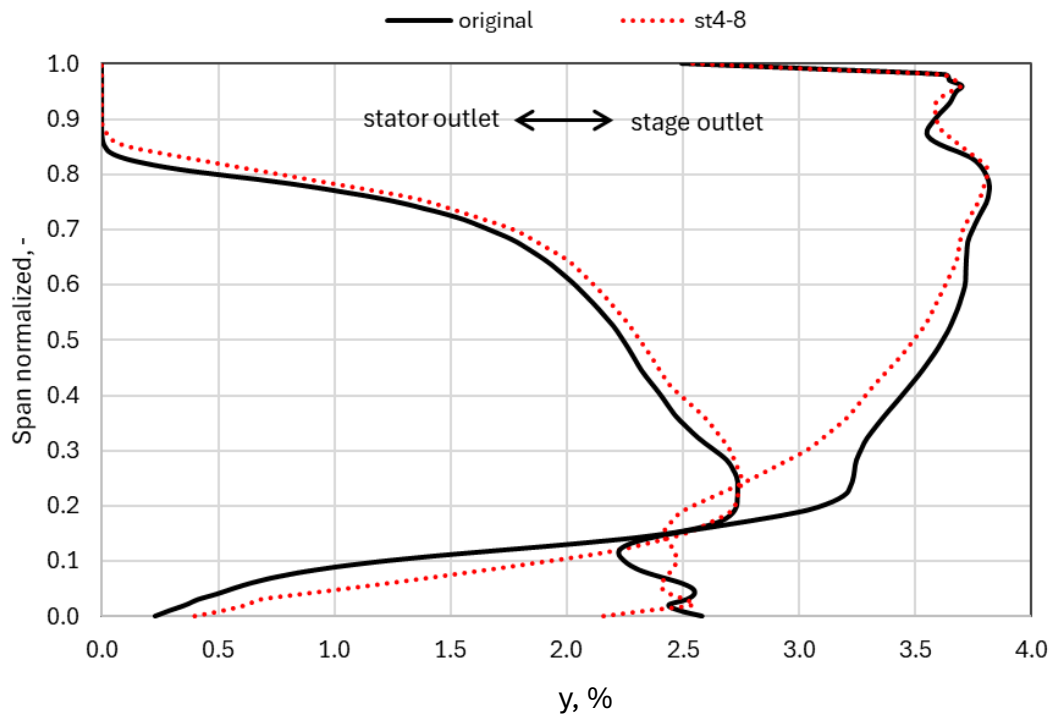
Fig.5.6. Wetness fraction along the span (stator outlet and stage outlet)

5.1.2. The effect of the number of blades in a row (the pitch size)

In the original stator row, there are 50 blades, and the distance from the stator hub to the shaft center is 670 mm. Therefore, the pitch size in the region near the hub can be calculated as follows:

$$original\ pitch = \frac{2\pi \times 670mm}{number\ of\ blades} = \frac{2\pi \times 670mm}{50} = 84.194\ mm$$

In this section, an investigation is carried out on how varying the number of blades in a stator row affects the flow. The blade count is adjusted to 52 and 48, respectively, resulting in corresponding changes in pitch size, as detailed below. Fig.5.7 shows these two cases in comparison with the original case.

$$case\ 1 - pitch = \frac{2\pi \times 670mm}{52} = 80.956\ mm$$

$$case\ 2 - pitch = \frac{2\pi \times 670mm}{48} = 87.702\ mm$$

As can be seen in Fig.5.7, the velocity magnitude at the interface for the cases remains almost constant. The velocity angles for st52 increases, but for st48 decreases. Fig. 5.8 and 5.9 confirm this information. As shown in Fig. 5.8, the channel area between two blades decreases in case st52 and increases in case st48 compared to the original design, leading to a reduction in mass flow rate and output power for the former case and an increase for the latter (Fig.5.10). Additionally, as depicted in Fig. 5.11, wetness increases in case st52 and decreases in case st48 at the stator outlet; however, this trend reverses at the stage outlet. The increase in wetness at the stator outlet in case st52, is because the expansion rate in the stator channel increases, according to Fig. 5.7, however, as the expansion rate decreases in case st48, so that the wetness decreases at the stator outlet.
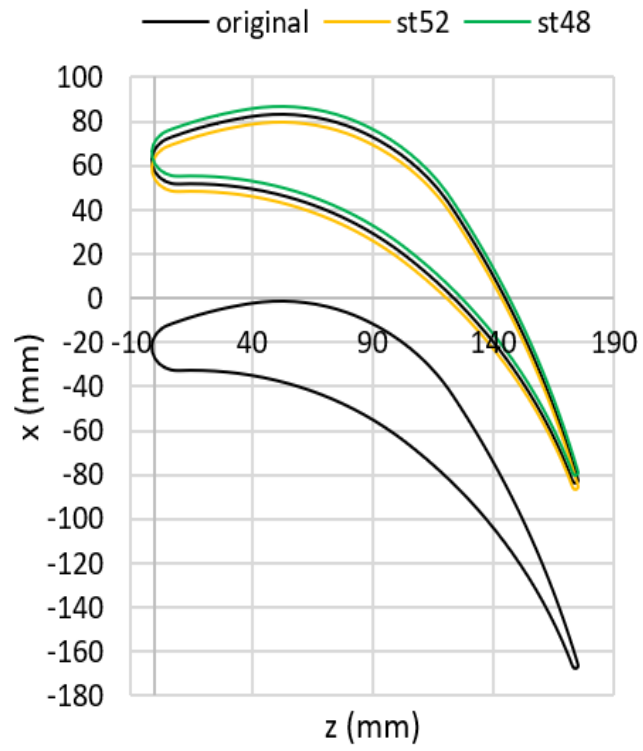
Fig.5.7. Comparison of blade profiles: Original vs. new profiles
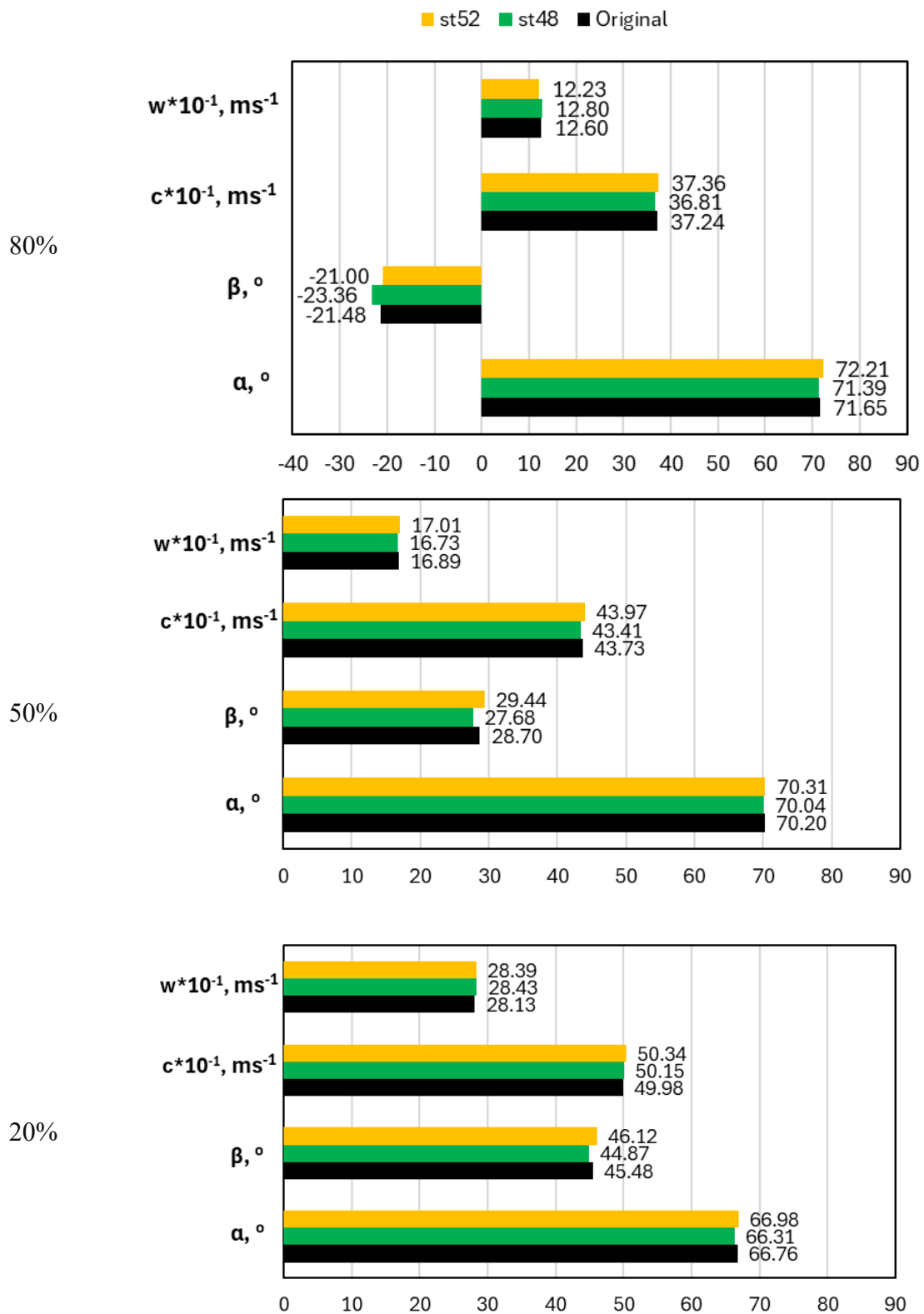
Fig.5.8. Flow angles and velocities at the stator-rotor interface
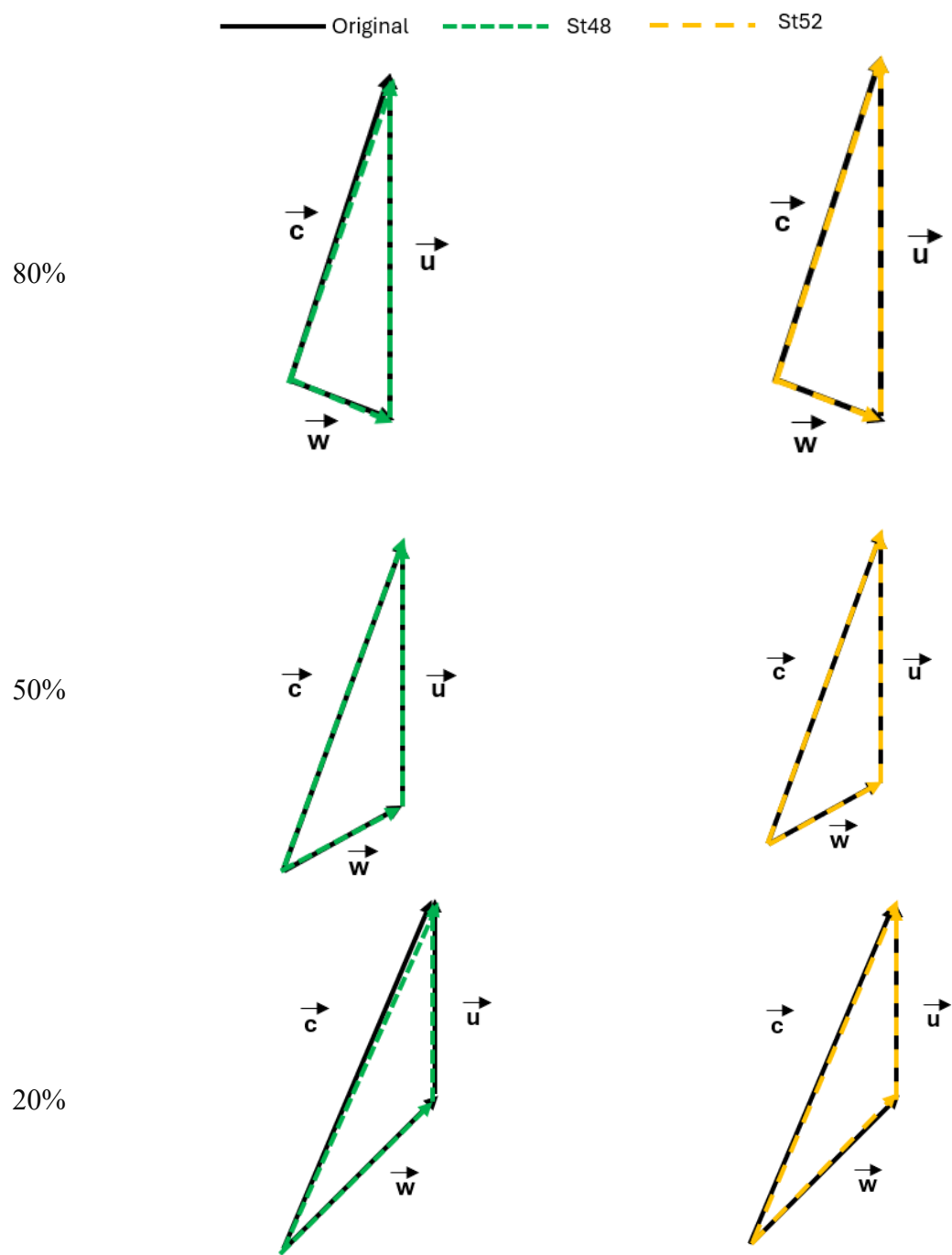
Fig.5.9. Velocity triangles at the stator-rotor interface
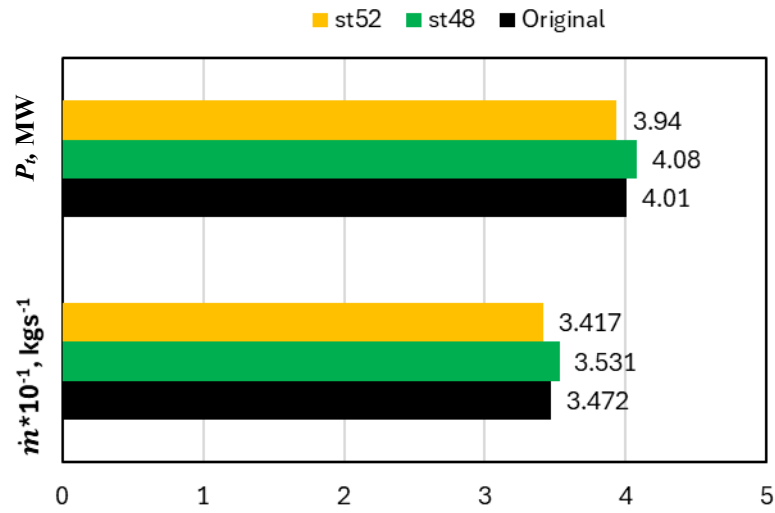
Fig.5.10. Average mass flow rate and output power
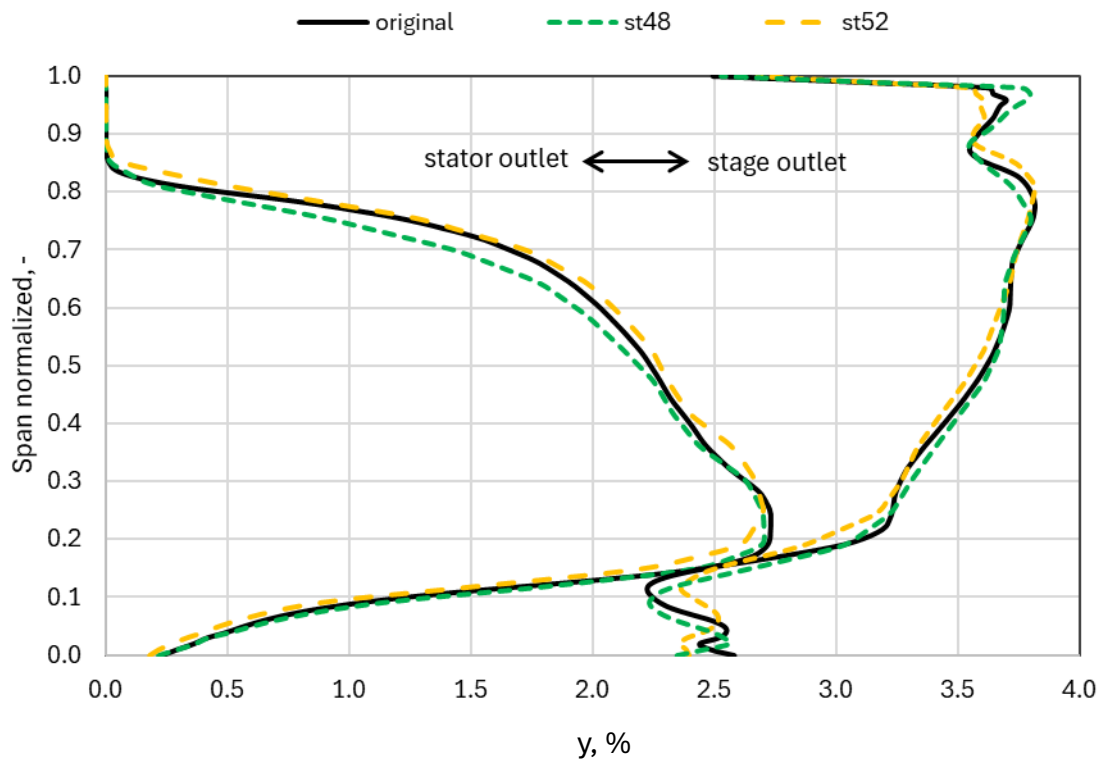
Fig.5.11. Wetness fraction along the span (stator outlet and stage outlet)

5.1.3. The effect of change of the blade profile

In this section, two well-known stator profiles, proposed by White [9] and Bakhtar [8], are investigated. The difference between these two profiles and the original blade is especially in the suction side of the blade, which is visible in Fig. 5.12 and 5.13. In the original profile compared to the Bakhtar profile, on the suction side, there is a bump which causes the pressure profile not to decrease gradually, and a bump in the pressure profile appears.

As illustrated in Fig. 5.14 and 5.15, the velocity magnitude and flow angles near the shroud region show no significant differences between the cases. However, at the 50% span and near the hub region, both the velocity magnitude and flow angles increase for the Bakhtar and White profiles. As shown in Fig. 5.13, the channel area between the two blades decreases in both the Bakhtar and White profiles compared to the original design, resulting in a reduction in mass flow rate (Fig. 5.16). However, as seen in Fig. 5.16, despite the reduced mass flow rate, the output power increases for the Bakhtar profile and remains unchanged for the White profile. This is because the output power depends not only on the mass flow rate but also on the total enthalpy change across the entire stage. Figure 5.17 shows that the wetness increases at the stator outlet and the stage outlet for both the Bakhtar and White profiles. This effect is particularly pronounced in regions close to the hub. The increase in wetness at the stator outlet, is because the expansion rate in the stator channel in Bakhtar and White profile increases compare to the original profile, according to Fig. 5.13.
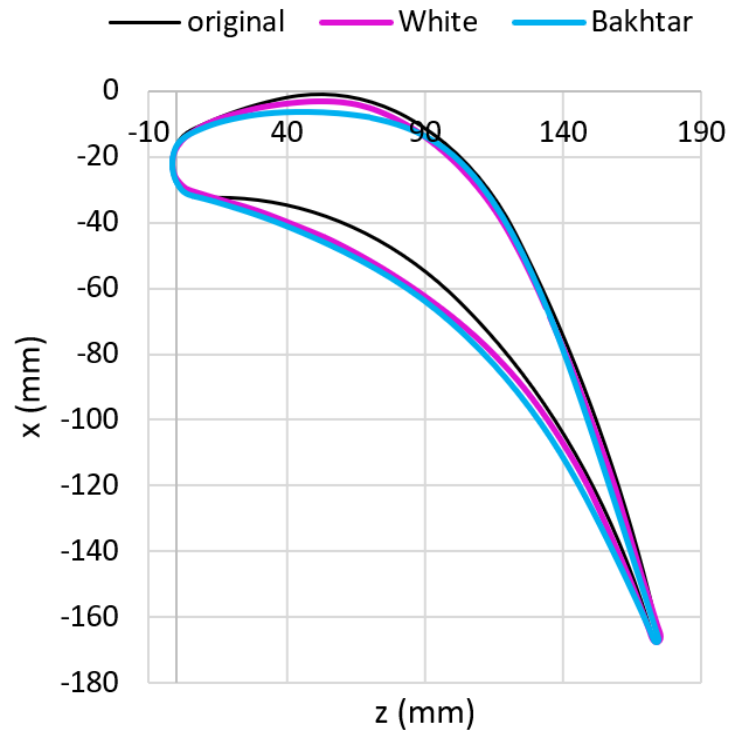
Fig. 5.12. Comparison of blade profiles: Original vs. new profiles
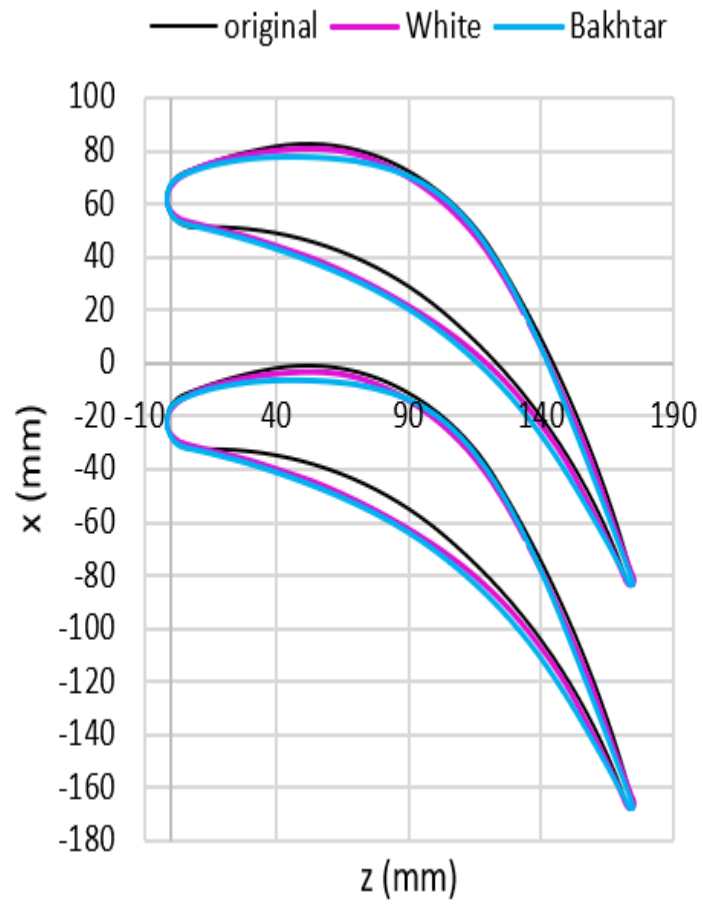
Fig. 5.13. Comparison of blade profiles: Original vs. new profiles
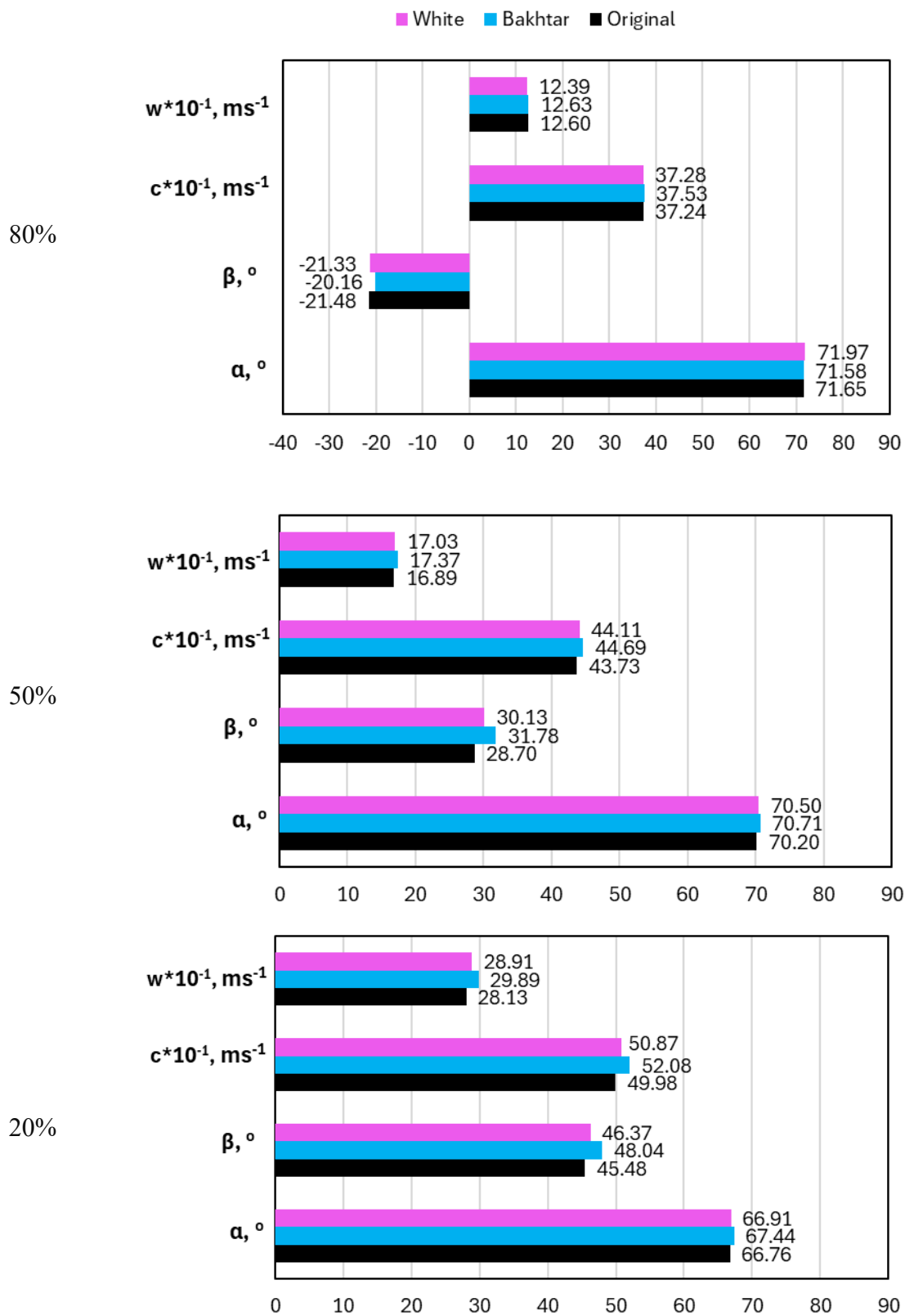
Fig.5.14. Flow angles and velocities at the stator-rotor interface
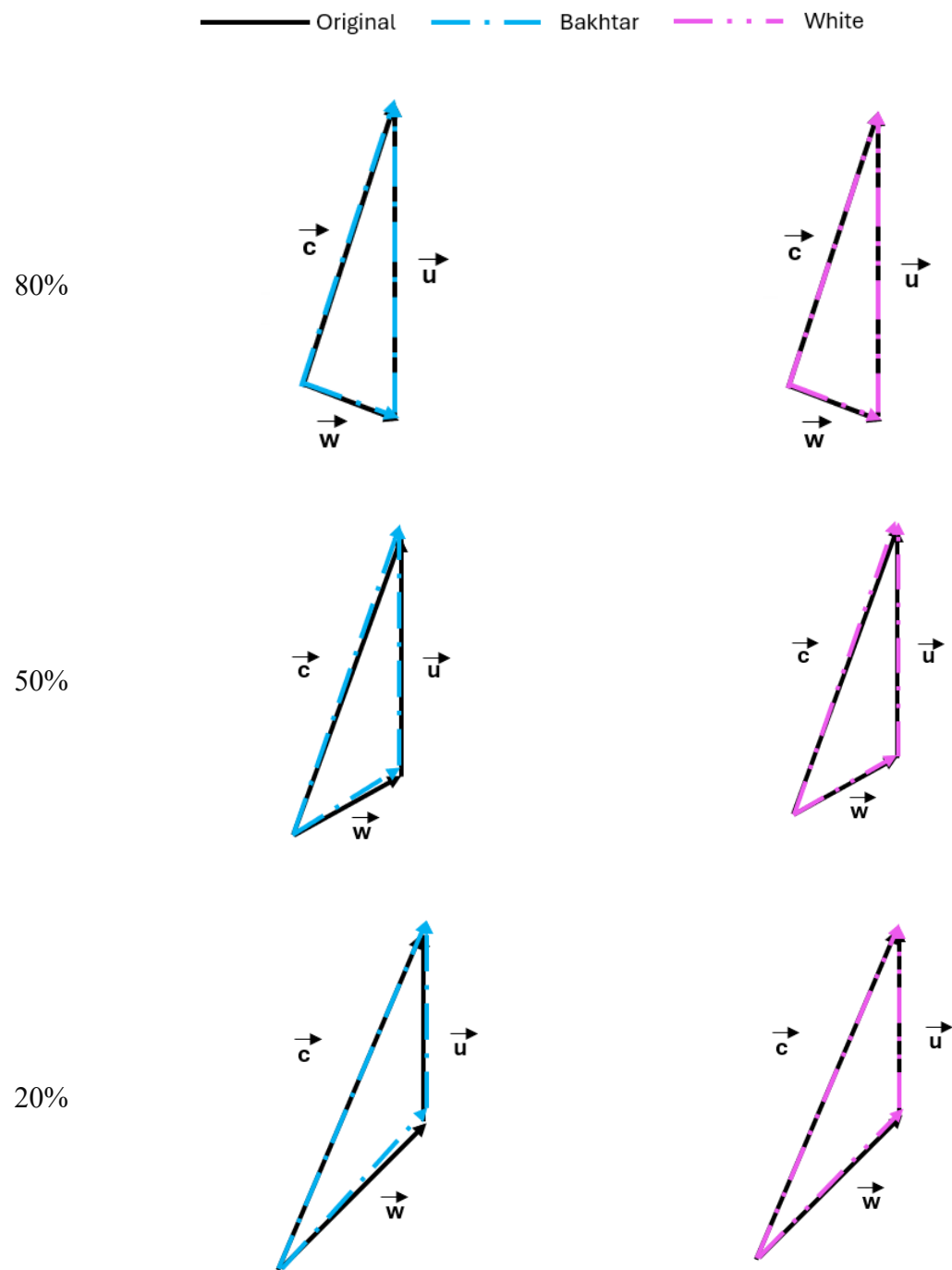
Fig.5.15. Velocity triangles at the stator-rotor interface

80%

50%

20%

Fig.5.16. Average mass flow rate and output power
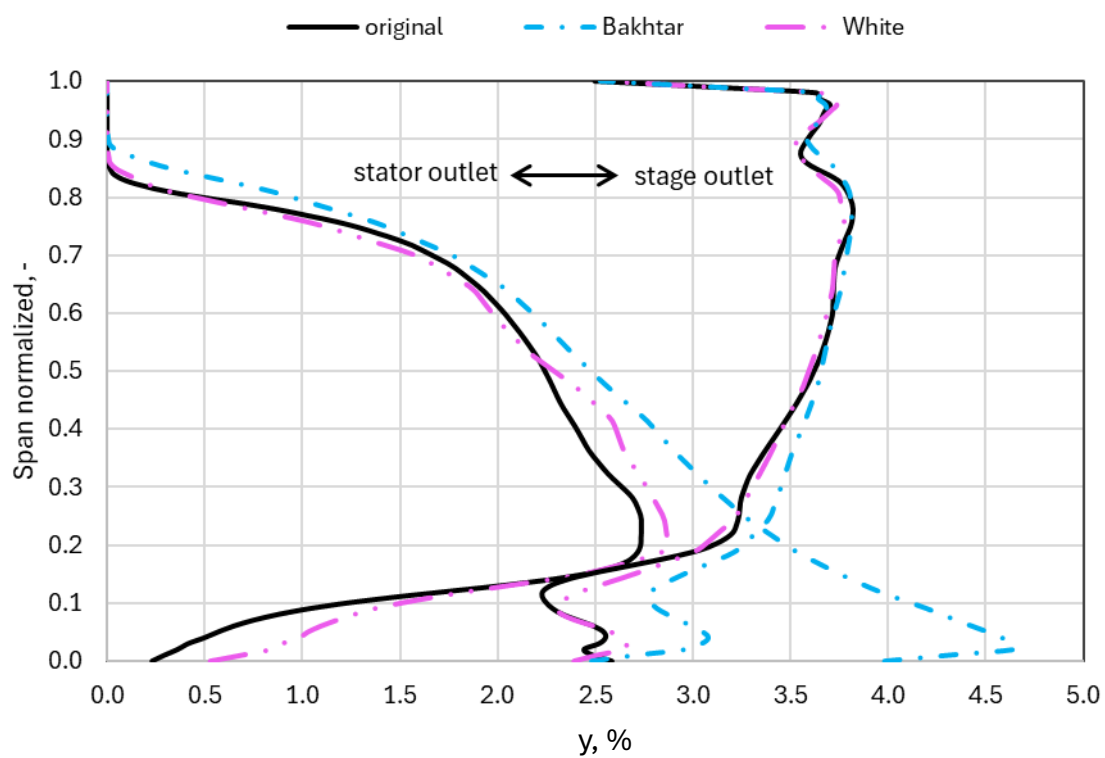
Fig.5.17. Wetness fraction along the span (stator outlet and stage outlet)

5.1.4. The effect of the rotation of the blade

In this section, the effect of the rotation of the blade is investigated. The trailing edge of the blade is considered as a base point, and the leading edge is rotated by +2 and -2 degrees to create two other cases. Fig. 5.18 shows these two cases.

As depicted in Fig. 5.19 and 5.20, both the velocity magnitude and flow angles increase at 50% span and near the hub region for the st+2deg case, while they decrease for st-2deg. According to Fig. 5.18, the channel area between the blades narrows in st+2deg and widens in st-2deg compared to the original design, leading to a decrease in both mass flow rate and output power for st+2deg, while the opposite is true for st-2deg (Fig. 5.21). Figure 5.22 indicates that wetness rises at the stator outlet but drops at the stage outlet for st+2deg, whereas the reverse trend is observed for st-2deg. This effect is particularly noticeable in regions near the hub. The increase in wetness at the stator outlet for st+2deg, is because the expansion rate in the stator channel increases in this case according to Fig.5.18, however, the decrease in expansion rate in case st-2deg results in a reduction in wetness at the stator outlet.

Fig. 5.18. Comparison of blade profiles: Original vs. new profiles
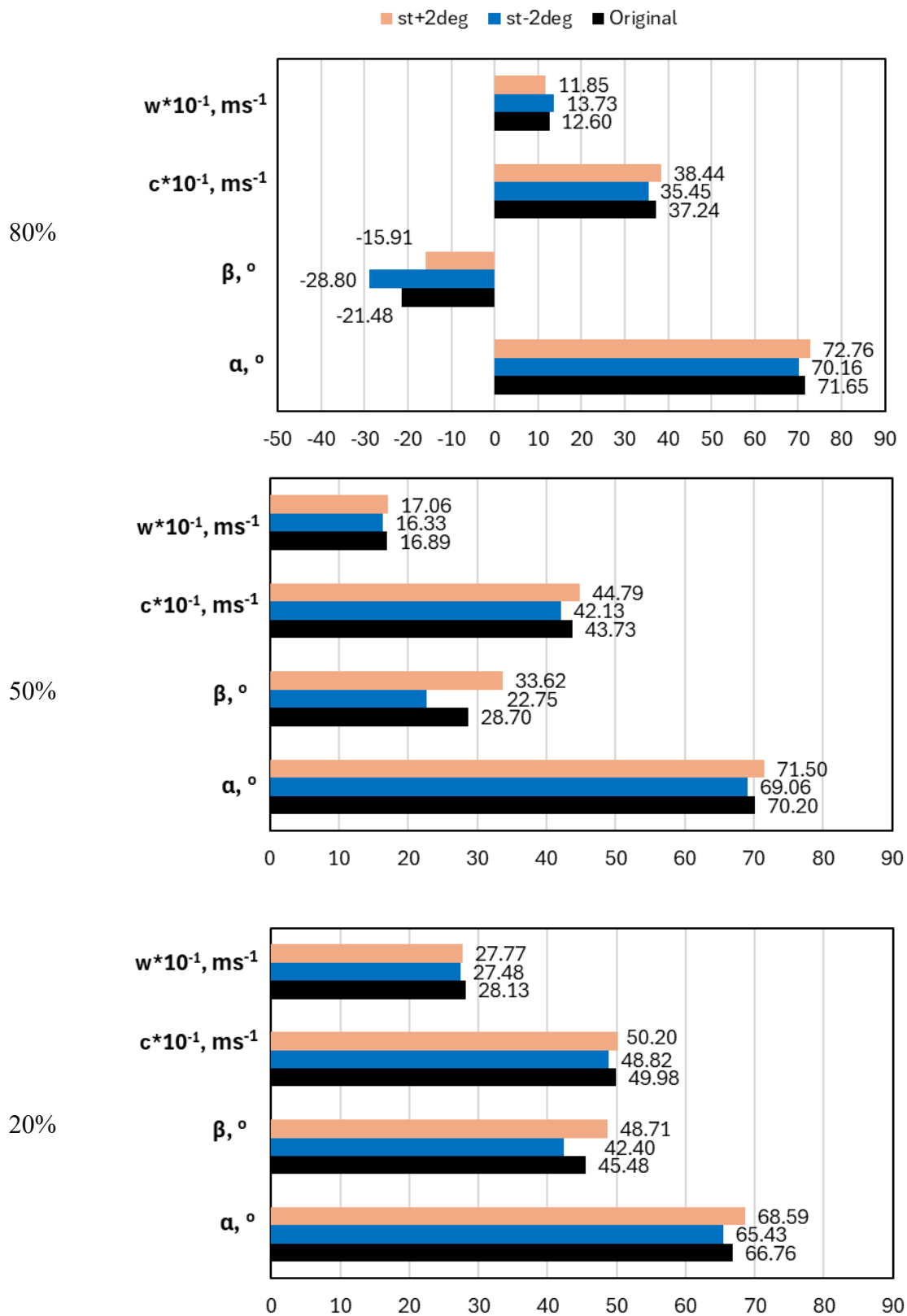
Fig.5.19. Flow angles and velocities at the stator-rotor interface

Fig.5.20. Velocity triangles at the stator-rotor interface

Fig.5.21. Average mass flow rate and output power
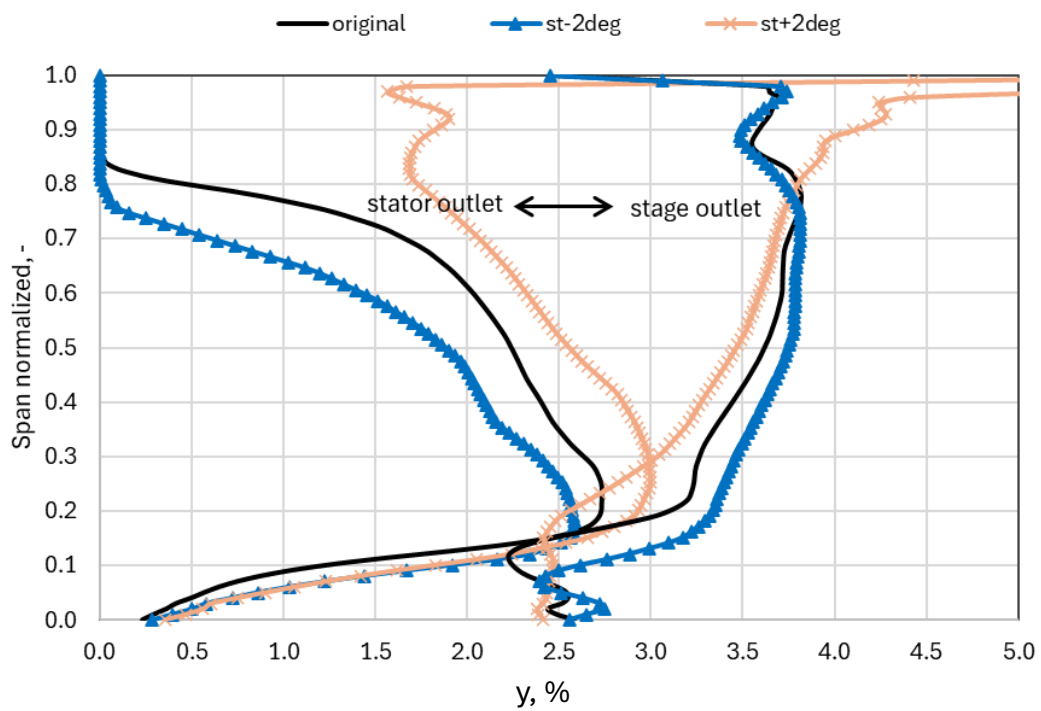
Fig.5.22. Wetness fraction along the span (stator outlet and stage outlet)

5.1.5. Comparison of all cases

Figure 5.23 presents the static pressure distribution on the stator blade near the hub region for all cases. As shown, the bump on the suction side of the Bakhtar and White profiles is smoother and less pronounced compared to the original case, where the bump is sharper, as previously explained.

Figures 5.24 and 5.25 compare the stage efficiency across all cases. As observed, the Bakhtar and st-2deg profiles show the highest efficiency, particularly in regions near the hub, while the st+2deg profile shows the lowest efficiency. Figure 5.26 shows the wetness at the stage outlet for all cases. According to this figure, the st+2deg profile has the highest wetness, while the st4-8 profile has the lowest.
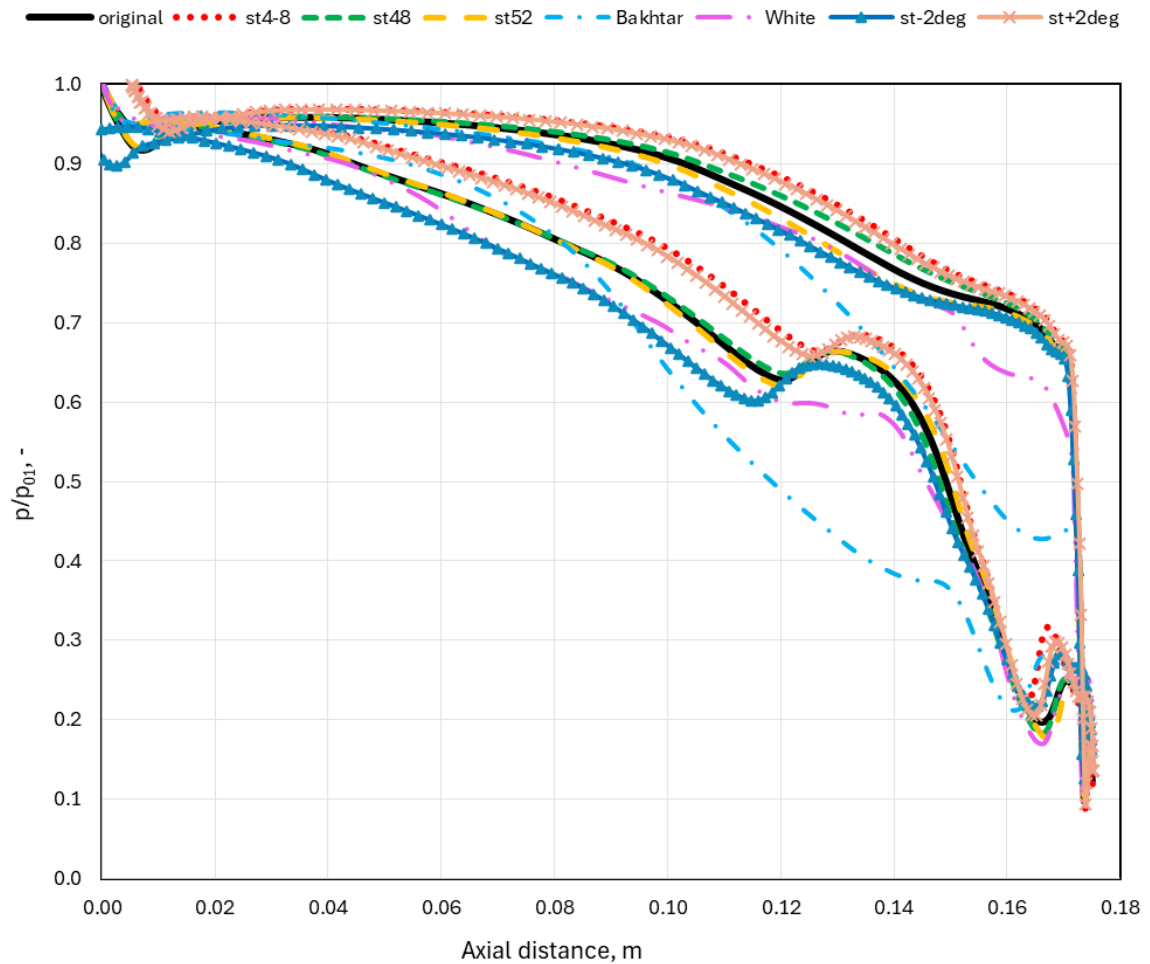
Fig.5.23. Pressure profile distribution on the stator blade in axial direction for the regions near the hub (20% span) for all cases
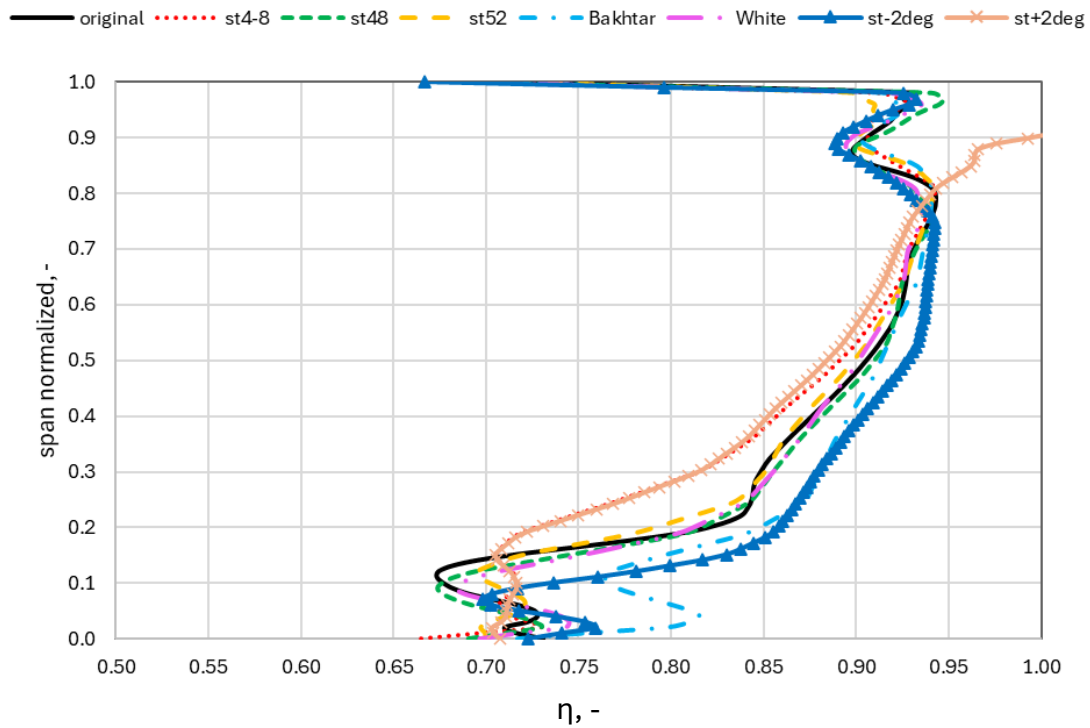
Fig.5.24. Stage efficiency distribution along the span for all cases
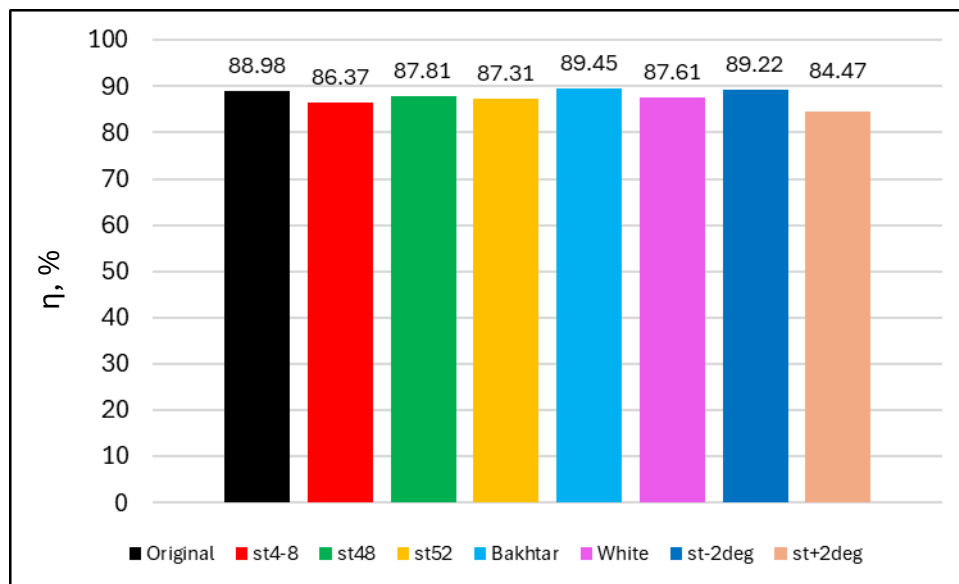
Fig.5.25. Average efficiency for the entire stage for all cases
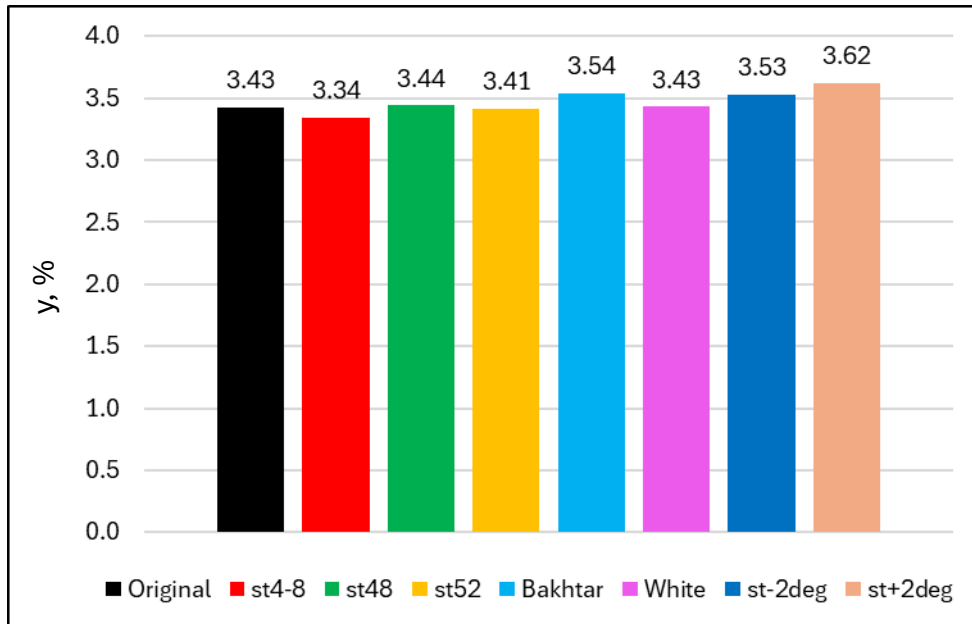
Fig.5.26. Average wetness at the stage outlet for all cases

To clarify the results of the case comparisons, the findings are summarized in Table 5.1. This table displays the changes in each parameter for every case relative to the original case, indicating the extent of increase (+) or decrease (-). According to the table, the Bakhtar profile and st-2deg case show the greatest improvement in efficiency. Additionally, the st-2deg case demonstrates the most significant increase in output power. However, both the Bakhtar and st-2deg cases also experience an increase in wetness, which is a crucial consideration. The st4-8 case shows the largest reduction in wetness but significantly decreases both output power and efficiency. The st+2deg case is the least favorable, as it not only results in a considerable increase in wetness but also substantially reduces efficiency and output power. The White profile has minimal impact on the results, with parameter values being nearly identical to those of the original case.

Table 5.1. Overview of changes in parameters for all cases compared to the original case

Cases	P_t (%)	η (%)	y (%)
st4-8	-7.73	-2.93	-2.62
st48	+1.74	-1.31	+0.29
st52	-1.74	-1.87	-0.58
Bakhtar	+0.99	+0.52	+3.2
White	0	-1.54	0
st-2deg	+9.22	+0.27	+2.91
st+2deg	-4.73	-5.06	+5.53

5.2 3D modification of the stator blade configuration

The stator blade discussed in the previous section belongs to the last stage of a traditional steam turbine. As observed, this original blade does not feature any sweep or lean in either the axial or circumferential directions. In contrast, modern steam turbines incorporate blades with more advanced geometrical features. In this section, the effects of axial sweep and circumferential lean on the stator blade are examined, and their impact on stage performance is evaluated. The angles used for sweep and lean modifications were selected based on the research by Lampart [75]. According to Table 5.2 and Fig. 5.27, four different cases are considered:

- Case AS involves the application of axial sweep.

- Case CL1 represents the application of circumferential lean in the direction of rotor rotation.

- Case CL2 includes circumferential lean in the opposite direction of rotor rotation.

- Case ASCL combines both axial sweep and circumferential lean.

Table 5.2. The appropriate angles for sweeping and leaning the stator blade

	AS	CL1	CL2	ASCL
Sweep angle	3.7º	-----	-----	4.3º
Lean angle	-----	13.6º	-6.8º	1.6º
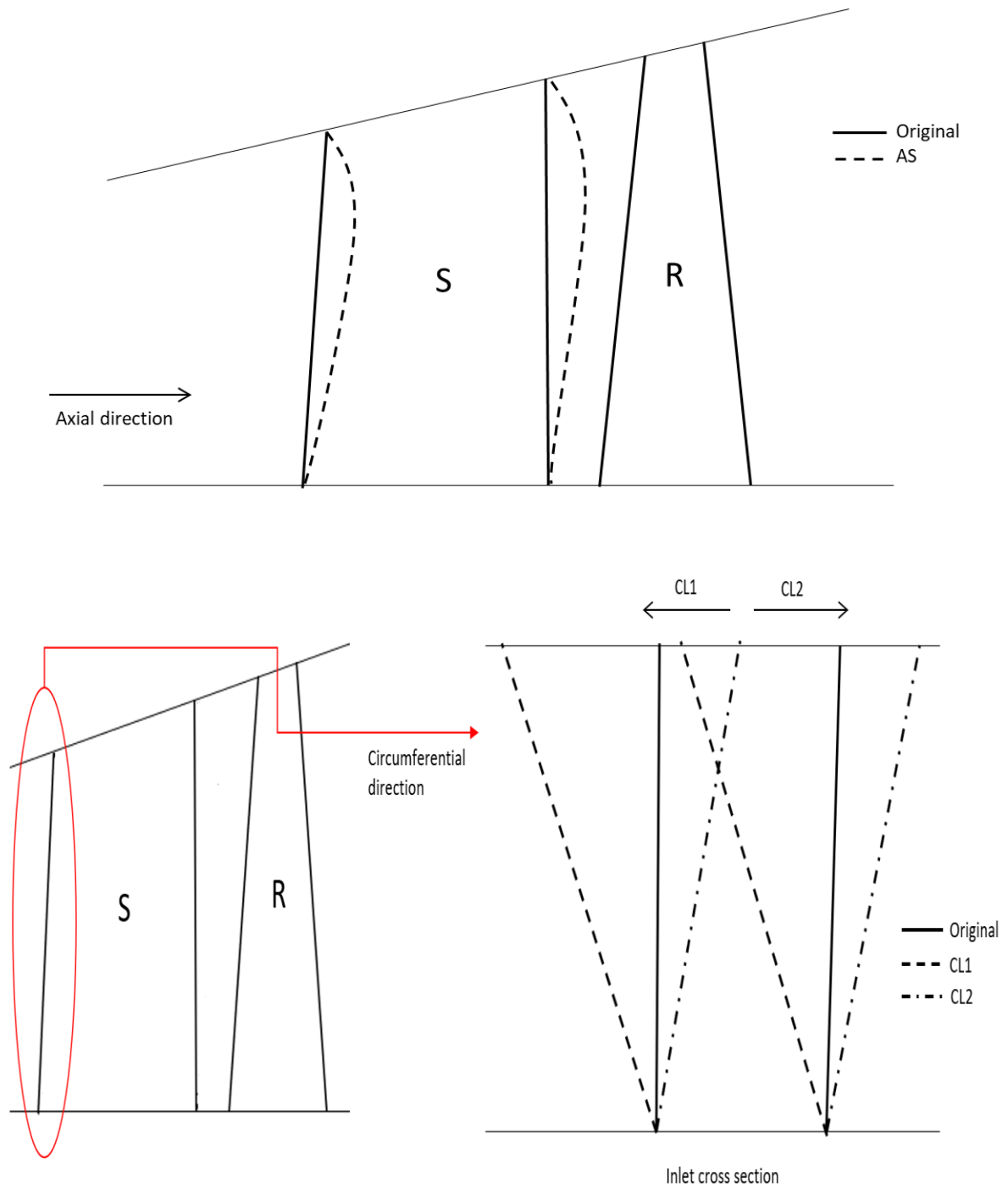
Fig. 5.27. Axial sweep (Top) and circumferential lean (Bottom) of the stator blade

The aim of this research is to investigate the effects of various modifications on stage performance. Consequently, the results of the different cases were compared in terms of stage efficiency, as shown in Fig. 5.28. As illustrated, case CL1 demonstrates the best performance, particularly in the hub regions, leading to a significant increase in efficiency. In contrast, cases AS and ASCL show no notable impact. Additionally, case CL2 even results in a decrease in efficiency in some areas.
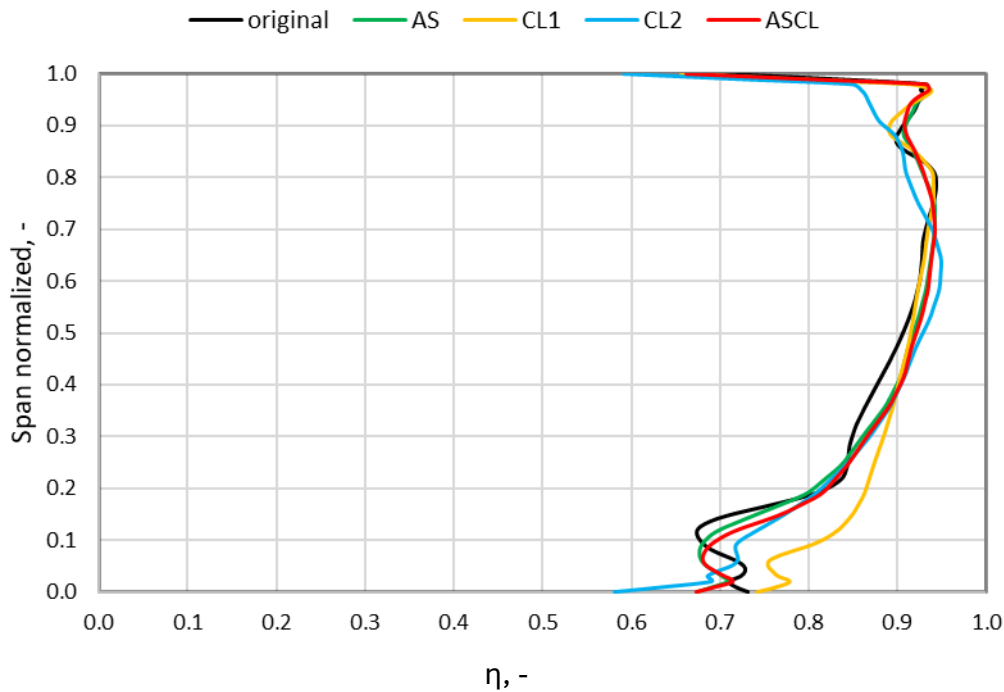
Fig. 5.28. Stage efficiency distribution along the span for the AS, CL1, CL2 and ASCL cases in comparison with the original one [definitions in Table 5.2]

Figure 5.29 compares the average values of various parameters for the examined cases for the entire stage. As can be seen, case CL1 has the greatest impact on increasing efficiency. The mass flow rate in this case remains nearly constant compared to the original case, while also contributing to an increase in the turbine's output power. On the other hand, case CL2 not only leads to a decrease in efficiency but also significantly reduces both the mass flow rate and the turbine's output power. Therefore, it can be concluded that circumferential lean has a positive and significant impact on turbine performance, resulting in a 0.7% increase in efficiency and a 2.2% increase in output power for this case.
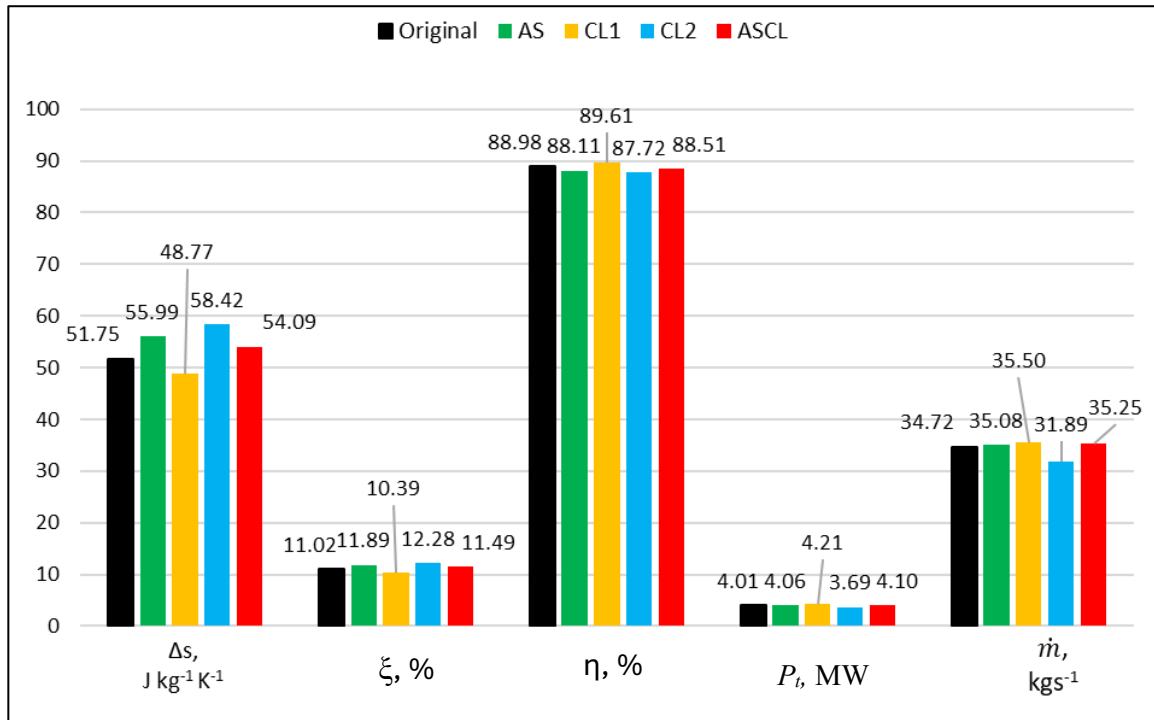
Fig. 5.29. The average values of entropy generation, entropy loss coefficient, isentropic efficiency, output power, and mass flow rate for the cases

5.3 The optimal configuration of the stator blade

In Section 5.1, it was concluded that the Bakhtar blade profile results in the least losses and the highest efficiency. In Section 5.2, it was observed that leaning the blade in the circumferential direction improves efficiency. In this section, these two effects are combined by placing the Bakhtar blade profile in a circumferentially leaned position (Case CL1 from Section 5.2). Figure 5.30 shows that the efficiency in the Bakhtar-CL1 case increases compared to both the original case and case CL1, particularly in the areas near the hub. Figure 5.31 indicates that the Bakhtar-CL1 case results in a 3.2% increase in efficiency and a 13.7% increase in turbine output power compared to the original case. The results are summarized in Table 5.3. Figure 5.32 compares the contours of the Bakhtar-CL1 with the original case.
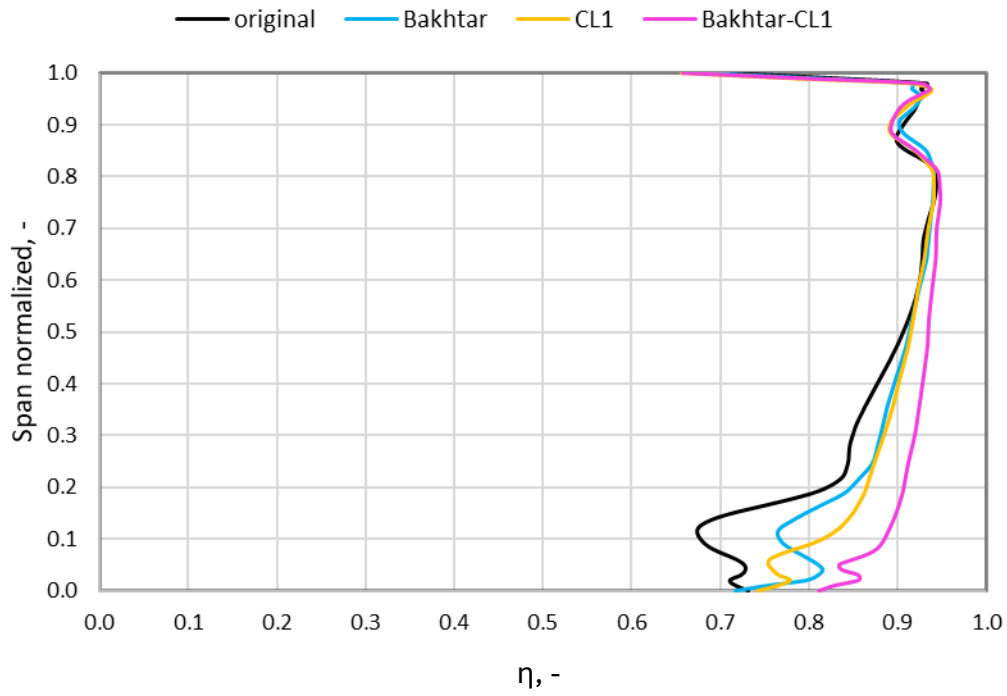
Fig. 5.30. Stage efficiency distribution along the span for the cases
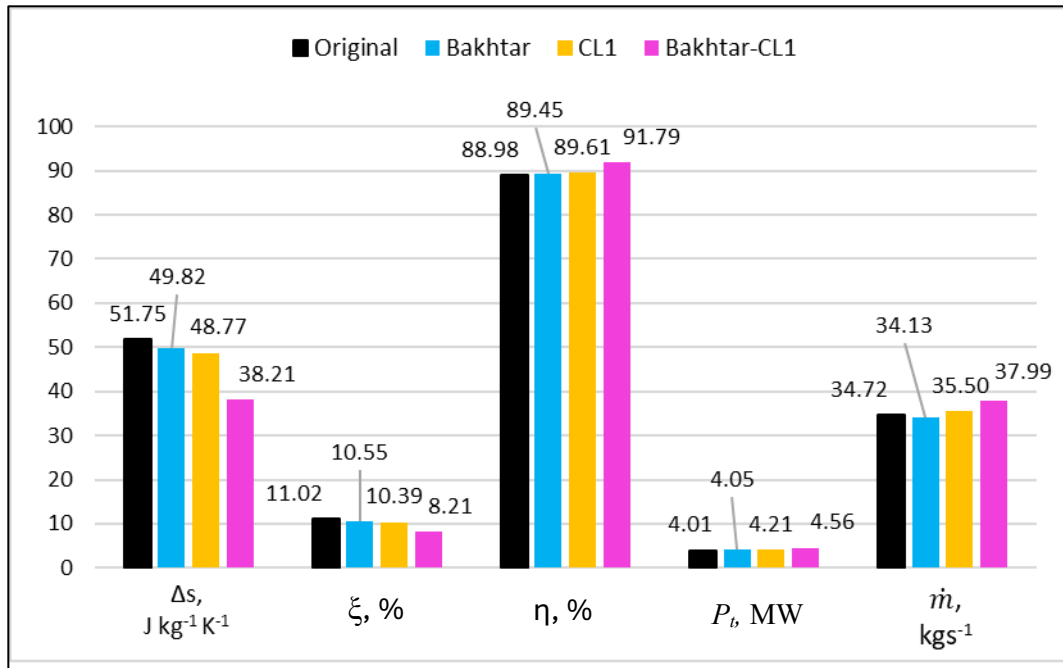
Fig. 5.31. The average values of entropy generation, entropy loss coefficient, isentropic efficiency, output power, and mass flow rate for the cases

Table 5.3. Overview of changes in parameters for the cases compared to the original case

Cases	ξ (%)	η (%)	P_t (%)
Bakhtar	-4.26	+0.52	+0.99
CL1	-5.7	+0.7	+2.2
Bakhtar-CL1	-25.5	+3.2	+13.7
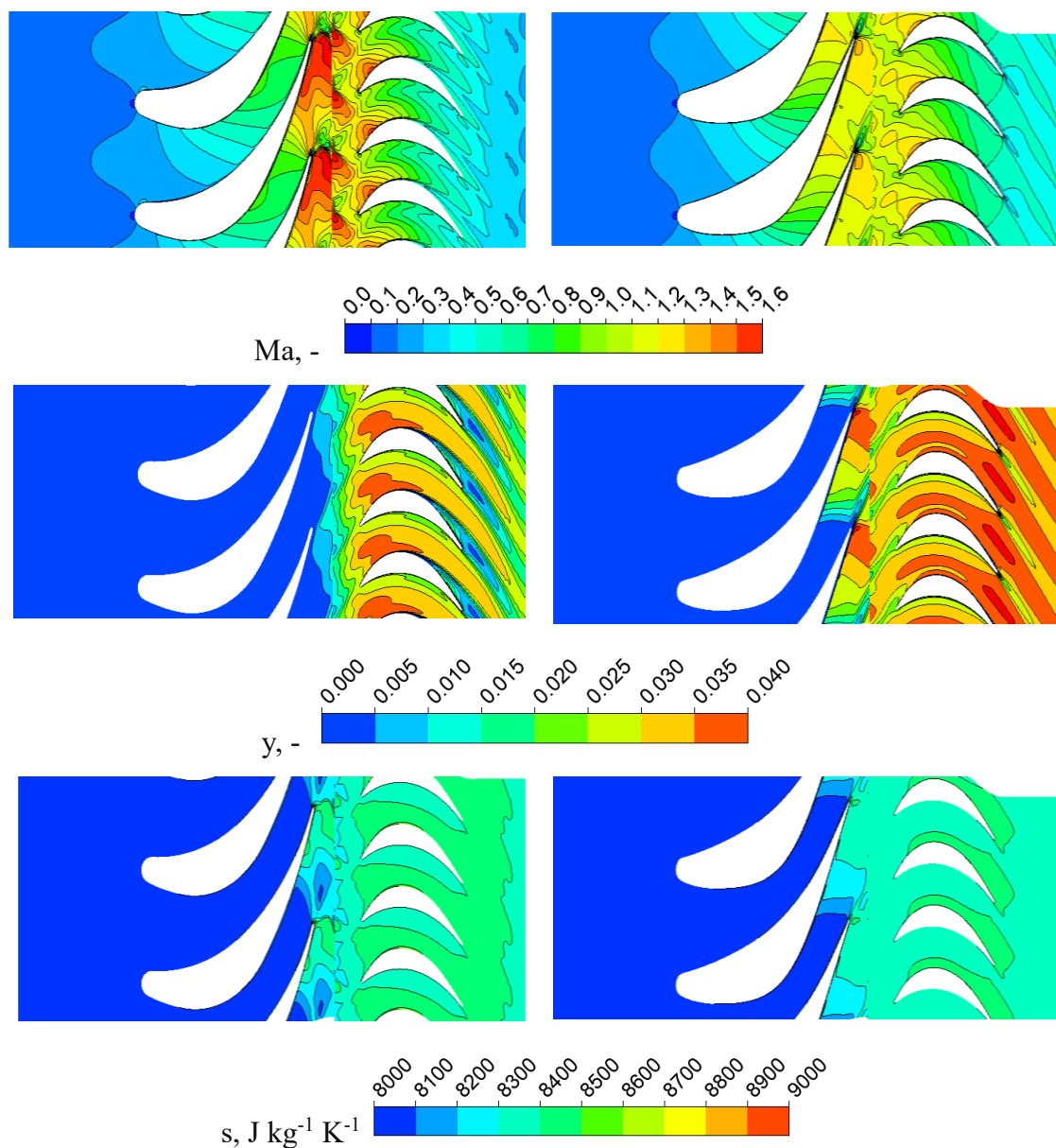
Fig. 5.32. Absolute Mach number, liquid mass fraction and specific entropy for original profile (Left) vs Bakhtar-CL1 profile (Right) at 10 % span

5.4 Conclusions

In this chapter, the wet steam flow through the final stage of a steam turbine, examined in the previous chapter, was reassessed. All configurations and numerical methods remained consistent with those used earlier. The primary focus of this chapter was on the stator blade, as it has the most significant impact on the entire stage results. Modifications to the stator profile include variations in spanwise rotation (st4-8), changes in pitch (st48 and st52), alterations to the profile shape (Bakhtar and White blades), and adjustments to the rotation of the stator profile (st-2deg and st+2deg). Then, the effect of axial sweep and circumferential lean of the stator blade was examined, and four cases were considered: AS, CL1, CL2, and ASCL. The results are as follows:

- In all cases, the changes in parameters are more pronounced in the regions near the hub compared to other areas.

- Even minor changes in the blade profile can lead to variations in mass flow rate, which in turn affects output power; this should be carefully considered. Another crucial point is that the velocity and angle of the stator's output flow directed towards the rotor also undergo changes, which is undesirable and should be taken into account when modifying the blade profile.

- The results at the stator outlet and stage outlet can differ with each other. For example, in some cases, wetness may increase at the stator outlet while decreasing at the stage outlet. Consequently, it is important to assess and analyze the influence of stator profile modifications on the results for the entire stage.

- The Bakhtar profile and st-2deg case exhibit the highest efficiency improvements, with the st-2deg case also showing a notable increase in output power. However, it's important to note that both cases experience a rise in wetness, which is a critical factor to consider.

- The st+2deg case is the least advantageous, as it causes a substantial rise in wetness while significantly diminishing both efficiency and output power.

- The circumferential lean in the direction of rotor rotation improves the stage efficiency, while the lean in the opposite direction reduces the efficiency.

- The proposed case is the Bakhtar profile while leaning in the direction of rotor rotation (Bakhtar-CL1). It improves the efficiency by 3.2 %.

6. Summary and Conclusions

6.1 Summary of the research

Wet steam, which consists of both vapor and liquid phases, plays a crucial role in the low-pressure stages of steam turbines, where its presence can lead to significant performance losses. Modeling wet steam flows presents a considerable challenge due to the complex interactions between the liquid and vapor phases, and the intricate geometry of turbine blades. This research is part of a broader effort to refine numerical models capable of accurately simulating wet steam flows, improving the design and operation of steam turbines, and ultimately enhancing their efficiency.

This thesis focused on several key aspects of wet steam flow modeling, including the application of various CFD tools to simulate the behavior of wet steam in both Laval nozzles and linear blade cascades. By comparing numerical simulation results with experimental data from the SUT in-house laboratory, this research aimed to identify the most accurate and reliable models for simulating wet steam flows. In particular, the study assessed the performance of different droplet growth models, such as the Gyarmathy, Fuchs-Sutugin, and Young models, for their ability to predict condensation and other flow characteristics.

Detailed investigations were carried out in various turbine geometries, including the low-pressure section of a 200 MW turbine, to quantify the impact of condensation on turbine efficiency and performance. Additionally, the effects of blade design modifications, such as 2D modifications in stator blade configurations, 3D modifications such as axial sweep and circumferential lean, were explored to understand their influence on stage performance and loss mechanisms.

The research also extended to the assessment of turbine efficiency and losses in the presence of wet steam. Detailed loss calculations for steam turbine stages provided valuable insights into the design of more efficient turbines, with a particular focus on minimizing the losses caused by condensation. This work contributes to the broader field of turbine optimization by addressing the gap in research related to wet steam modeling in complex three-dimensional turbine geometries.

6.2 Key findings and conclusions

Based on the results obtained from the various CFD simulations and their comparison with experimental data, several important conclusions can be drawn:

1. Selection of optimal models for wet steam flow simulation:

   - Cases 3, 4, and 6, which employed the Gyarmathy and Fuchs-Sutugin droplet growth models, provided the most accurate predictions of static pressure distributions in both the Laval nozzle and rotor-blade cascade geometries. These models demonstrated superior reliability and consistency in predicting flow behavior compared to the Young model, which was found to be less effective for modeling wet steam flows.

   - Cases 1, 2, and 7 were considered unsuitable for wet steam flow simulations because their isentropic efficiency values were unrealistic, making them unreliable for precise simulations.

   - It is recommended that the Gyarmathy and Fuchs-Sutugin models (particularly cases 3, 4, and 6) be used for simulating condensation phenomena in wet steam flows. However, adjustments to these models may be necessary to improve the accuracy of predicting droplet diameters.

2. Impact of wet steam on turbine efficiency and losses:

   - Wet steam flow leads to significant changes in turbine flow parameters. Notably, condensation at the stator trailing edge close to the hub and rotor suction side close to shroud, results in entropy generation and loss of efficiency. In the simulations, condensation was found to decrease turbine efficiency by approximately 1.27% and reduce output power by 15.04%.

   - A comparison between adiabatic (dry) and wet steam flows showed that condensation causes shifts in shock wave positions and increases their intensity. Additionally, it lowers the Mach number in wet regions, reducing flow velocity and affecting the outlet flow angles.

3. Effect of blade configuration modifications on stage performance:

   - The investigation of stator blade modifications, including variations in blade twist, pitch size, profile shape, and the implementation of axial sweep and circumferential lean, demonstrated that even small changes in blade geometry can significantly affect the overall turbine stage performance.

   - Modifying the stator blade configuration had a more pronounced effect on the stage efficiency near the hub region compared to changes in other areas. The implementation of circumferential lean in the direction of rotor rotation improved efficiency, while lean in the opposite direction reduced it.

- The Bakhtar blade profile, combined with circumferential lean in the direction of rotor rotation (Bakhtar-CL1), was identified as the most effective configuration, improving efficiency by 3.2%.

4. Effect of wet steam on turbine losses and performance sensitivity:

- Wet steam flow leads to significant entropy generation and increased losses, particularly in regions where condensation occurs. These losses were quantified, and the results showed that the stator contributes to the majority of losses, with approximately 10% of the total losses occurring along the stator and only 1% along the rotor.

- The study also revealed the sensitivity of turbine performance to changes in stator configurations. Even minor modifications to the stator configuration can lead to significant variations in flow parameters and efficiency, highlighting the importance of precise blade design for optimal turbine performance.

6.3 Recommendations for future research

The findings of this study underscore the complexity of modeling wet steam flows in steam turbines and the importance of selecting appropriate numerical models for accurate predictions. However, several areas remain for further exploration:

- Model refinement: While the Gyarmathy and Fuchs-Sutugin models showed promise, further refinements are necessary to improve their ability to predict droplet diameter more accurately. Additional studies should focus on adjusting these models to reduce uncertainty in wet steam flow predictions.

- Experimental validation: While CFD simulations provided valuable insights, additional experimental data, particularly in real turbine geometries, would be beneficial to further validate the simulation results and improve the reliability of the models.

- Cross-validation using alternative CFD software: The results from this study should be cross-checked and verified against simulations performed using other CFD software platforms. Comparing results from different tools will help identify any discrepancies and offer a broader confidence in the predictions. It is important that the outcomes from various CFD solvers be consistently aligned to ensure their accuracy and to provide a comprehensive understanding of wet steam dynamics in turbines.

References

1. Bakhtar F, Moetazedian M. A Study of the Throughflow of Nucleating Steam in a Turbine Stage by Means of Time-Averaged CFD. Proc. Inst. Mech. Eng. Part A: J. Power Energy. 2013, vol. 227(4), pp. 449–461.

2. Zhang H, Liu J, Li Z, Zhang M, Yu H. Performance of Non-Equilibrium Condensation Flow in Wet Steam Turbines. Appl. Therm. Eng. 2022, vol. 204, 117974.

3. Bakhtar, F., Mashmoushy, H., Jadayel, O.C. On the performance of a cascade of turbine rotor tip section blading in wet steam – Part 2: Surface pressure distributions. Proc. Inst. Mech. Eng. Part C: J. Mech. Eng. Sci., 1997, 211(7), 519–529.

4. Wen, C., Yang, Y., Ding, H., Sun, C., Yan, Y. Wet steam flow and condensation loss in turbine blade cascades. Appl. Therm. Eng., 2021, 189, 116748.

5. Young J. The spontaneous condensation of steam in supersonic nozzles. PhysicoChem Hydrodyn 1982, vol. 3, no.1, pp. 57-82.

6. Moses CA and Stein GD. On the growth of steam droplets formed in a laval nozzle using both static pressure and light scattering measurements. Trans ASME J Fluids Eng 1978, vol. 100, no.1, pp. 311-322.

7. Barschdorff D, Hausmann G, Ludwig A. Flow and Drop Size Investigations of Wet Steam at Subsonic and Supersonic Velocities with the Theory of Homogeneous Condensation. Pr.Inst. Maszyn Przeplywowych 1976, vol. 1, no. 1, pp. 241-250.

8. Bakhtar F, Mahpeykar MR, Abbas K. An Investigation of Nucleating Flows of Steam in a Cascade of Turbine Blading-Theoretical Treatment. J. Fluids Eng. 1995, vol. 117, pp. 138-144.

9. White A. Condensation in Steam Turbine Cascades. Doctoral Dissertation 1992, King's college, DOI: 10.13140/RG.2.2.16703.18082.

10. Dykas S, Majkut M, Strozik M, Smołka K. Experimental study of condensing steam flow in nozzles and linear blade Cascade. International Journal of Heat and Mass Transfer 2015, vol. 80, pp. 50-57.

11. Han, X., Han, Z., Zeng, W., Li, P., Qian, J. Numerical simulation of wet steam transonic condensation flow in the last stage of a steam turbine. Int. J. Numer. Meth. Heat Fluid Flow, 2018, 28(10), 2378–2403.

12. Zhao, X., He, Z., Wang, F. Numerical investigation of non-equilibrium condensation in wet steam flow through a turbine cascade using an improved wet steam model. Energy, 2020, 195, 116949.

13. Chandler KD, White AJ, Young JB. Non-equilibrium wet-steam calculations of unsteady low-pressure turbine flows. Proc IMechE, Part A: J Power and Energy 2014, vol. 228, pp. 143-152.

14. Halama J, Benkhaldoun F, Fort J. Flux schemes based finite volume method for internal transonic flow with condensation. Int J Numer Method Fluids 2010, vol. 65, pp. 953-968.

15. Halama J, Benkhaldoun F, Fort J. Numerical modeling of two-phase transonic flow. Math and Comput Simul 2010, vol. 80, pp. 1624-1635.

16. Wroblewski W, Dykas S, Gepert A. Steam condensing flow modeling in turbine channels. Int J Multiph Flow 2009, vol. 35, pp. 498-506.

17. Yamamoto S and Daiguji H. Higher-order-accurate upwind schemes for solving the compressible Euler and Navier-stokes equations. Comput Fluids 1993, vol. 22, pp. 259-270.

18. Yamamoto S. Computation of practical flow problems with release of latent heat. Energy 2005, vol. 30, pp. 197-208.

19. Starzmann J, Hughes FR, Schuster S, et al. Results of the International Wet Steam Modeling Project. Proceedings of the Institution of Mechanical Engineers, Part A. 2018, vol. 232, no. 5, pp. 550-570.

20. Kalikmanov VI. Classical nucleation theory. in Nucleation theory: Springer 2013, pp. 17-41, https://doi.org/10.1007/978-90-481-3643-8_3.

21. Becker R and Döring W. Kinetische behandlung der keimbildung in übersättigten dämpfen. Annalen der physik 1935, vol. 416, no. 8, pp. 719-752, https://doi.org/10.1002/andp.19354160806.

22. Patel, V., et al. Effect of turbulence modeling on condensing steam flows in a nozzle and turbine blade cascade. Journal of Fluids Engineering, 2021, 143(7), 071103.

23. Wittmann, T., Bode, C., Friedrichs, J. The feasibility of an Euler–Lagrange approach for the modeling of wet steam. Journal of Engineering for Gas Turbines and Power, 2021, 143(4), 041019.

24. Courtney WG. Remarks on Homogeneous Nucleation. J. Chem. Phys. 1961, vol. 35, no. 117, pp. 2249-2250.

25. Wolk J, Strey R, Heath CH, Wyslouzil BE. Empirical Function for Homogeneous Water Nucleation Rates. J. Chem. Phys. 2002, vol. 117, no. 10.

26. Kantrowitz A. Nucleation in very rapid vapor expansions. The Journal of Chemical Physics 1951, vol. 19, no. 9, pp. 1097-1100.

27. Bakhtar F, Young J, White A, Simpson D. Classical nucleation theory and its application to condensing steam flow calculations. Proceedings of the Institution of Mechanical Engineers 2005, Part C: Journal of Mechanical Engineering Science, vol. 219, no. 12, pp. 1315-1333.

28. Spalding DB. Combustion of liquid fuels. Nature 1950, vol. 165, no. 4187, https://doi.org/10.1038/165160a0

29. Young J. The condensation and evaporation of liquid droplets in a pure vapour at arbitrary Knudsen number. International journal of heat and mass transfer 1991, vol. 34, no. 7, pp. 1649-1661.

30. Bakhtar F and Zidi K. On the self diffusion of water vapour. Proceedings of the Institution of Mechanical Engineers 1985, Part C: Journal of Mechanical Engineering Science, vol. 199, no. 2, pp. 159-164.

31. Young J. Two-Dimensional, Nonequilibrium, Wet-Steam Calculations for Nozzles and Turbine Cascades. Journal of Turbomachinery 1992, vol. 114, no. 3, pp. 569-579, 1992.

32. Peters F and Paikert B. Measurement and interpretation of growth and evaporation of monodispersed droplets in a shock tube. International journal of heat and mass transfer 1994, vol. 37, no. 2, pp. 293-302.

33. Gyarmathy G, Burkhard H, Lesch F, Siegenthaler A. Spontaneous condensation of steam at high pressure: first experimental results. Proceedings of IMechE Conference on Heat and fluid flow in steam and gas turbine plant 1973, vol. 3, pp. 182-186.

34. Peeters P, Luijten C, Van Dongen M. Transitional droplet growth and diffusion coefficients. International journal of heat and mass transfer 2001, vol. 44, no. 1, pp. 181-193.

35. Hanimann L, Mangani L, Kasartelli E, Vogt DM, Darwish M. Real Gas Models in Coupled Algorithms Numerical Recipes and Thermophysical Relations. International Journal of Turbomachinery Propulsion and Power 2020, vol. 5, no. 3.

36. Raman SK and Kim HD. Solutions of supercritical CO2 flow through a convergent-divergent nozzle with real gas effects. International Journal of Heat and Mass Transfer 2018, vol. 116, pp. 127-135.

37. Raman SK and Kim HD. A new equation of state to predict S-CO2 flow with real gas effects. Journal of Mechanical Science and Technology 2018, vol. 32, no. 3, pp. 1099-1104.

38. Wen CH, Yang Y, Zhu X, Walther JH, Ding H, Feng Y, Yan Y. Real gas effects on non-equilibrium condensation of carbon dioxide contributing to carbon capture and storage. International Conference on Applied Energy 2019, 1029.

39. Furusawa T, Moriguchi SH, Miyazawa H, Yamamoto S. Real Gas Simulation for High-pressure and Low-pressure Nonequilibrium Condensation in Transonic Flows. Proceedings of Global Power and Propulsion Society, Beijing Conference 2019, https://doi.org/10.33737/gpps19-bj-093

40. Patel Y, Patel G, Turunen-Saaresti T. Influence of turbulence modelling on non-equilibrium condensing flows in nozzle and turbine cascade. Int J Heat and Mass Transf 2015, vol. 88, pp. 165-180.

41. Wu X, Li L, Li G, Feng Z. Numerical investigation of the effect of inlet condition on self-excited oscillation of wet steam flow a supersonic turbine cascade. Int J Numer Meth Fluids 2009, vol. 60, pp. 1334-1350.

42. ANSYS CFX-Solver Theory Guide, release 15 November 2013

43. ANSYS Fluent User's Guide, release January 2022

44. Ihm, S. W., & Kim, C. (2008). Computations of homogeneous-equilibrium two-phase flows with accurate and efficient shock-stable schemes. AIAA Journal, 46, 3012–3037. https://doi.org/10.2514/1.37520

45. Schuster, S., Benra, F., Dohmen, H., et al. (2014). Sensitivity analysis of condensation on calculated liquid film motion in radial turbines. ASME Turbo Expo 2014: Turbine Technical Conference and Exposition, Düsseldorf, Germany, GT2014-26981. https://doi.org/10.1115/GT2014-26981

46. Grübel, M., Starzmann, J., Schatz, M., et al. (2015). Two-phase flow modeling and measurements in low-pressure turbines: Part 1 – Numerical validation of wet steam models and turbine modeling. Journal of Engineering for Gas Turbines and Power, 137(6), 062604. https://doi.org/10.1115/1.4029024

47. Kermani MJ and Gerber AG. A General Formula for the Evaluation of Thermodynamic and Aerodynamic Losses in Nucleating Steam Flow. Int. J. Heat and Mass Transfer 2003, vol. 46, no. 17, pp. 3265-3278.

48. Yu X, Xiao Zh, Xie D, Wang Ch, Wang C. A 3D method to evaluate moisture losses in a low pressure steam turbine: Application to a ultimate stage. International Journal of Heat and Mass Transfer 2015, vol. 84, pp. 642-652.

49. Bahr Ennil A, Al-Dadah R, Mahmoud S, Rahbar K, Al-Jubori A. Minimization of loss in small scale axial air turbine using CFD modeling and evolutionary algorithm optimization. Applied Thermal Engineering 2016, vol. 102, pp. 841-848.

50. Ding H, Zhao Y, Wen Ch, Wang Ch, Sun Ch. Energy efficiency and exergy destruction of supersonic steam ejector based on nonequilibrium condensation model. Applied Thermal Engineering 2021, vol. 189, 116704.

51. Wen Ch, Yang Y, Ding H, Sun Ch, Yan Y. Steam flow and condensation loss in turbine blade cascades. Applied Thermal Engineering 2021, vol. 189, 116748.

52. Vatanmakan M, Lakzian E, Mahpeykar MR. Investigating the entropy generation in steam flow in turbine blades with volumetric heating. Energy 2018, vol. 147, pp. 701-714.

53. Lampart, P., Yershov, S., & Rusanov, A. Increasing flow efficiency of high-pressure and low-pressure steam turbine stages from numerical optimisation of 3D blading. Engineering Optimization, 2005, 37(2), 145–166.

54. Wróblewski, W., Dykas, S., Gardzilewicz, A., & Kolovratnik, M. Numerical and Experimental Investigations of Steam Condensation in LP Part of a Large Power Turbine. Journal of Fluids Engineering, 131(4), 041301 (2009).

55. Bondyra R, Przytulski J, Dominiczak K. Development of ultimate stage blade of 13K215 turbine intermediate pressure module. archives of thermodynamics 2022, vol. 43, no. 1, pp. 45-62.

56. Heidari M and Amini K. Structural modification of a steam turbine blade. IOP Conference Series: Materials Science and Engineering 2017, vol. 203, 012007, doi:10.1088/1757-899X/203/1/012007

57. Ansari M, Esfahanian V, Izadi MJ, Bashi H, Tavakoli A, Kordi M. A new optimization strategy for wet steam effect minimization in steam turbine using combined 2D non-equilibrium wet steam flow and mean-line analysis. International Journal of Heat and Mass Transfer 2024, vol. 220, 124964.

58. Gribin VG, Tishchenko AA, Alekseev RA et al. Application of the Parametric Method for Profiling the Interblade Channels in the Nozzle Cascades of Axial-Flow Turbine Machines. Thermal Engineering 2020, vol. 67, no. 8, pp. 536–542. https://doi.org/10.1134/S0040601520080029

59. Noori Rahim Abadi SMA, Ahmadpour A, Abadi SMNR, Meyer JP. CFD-based shape optimization of steam turbine blade cascade in transonic two phase flows. Applied Thermal Engineering 2017, vol. 112, pp. 1575-1589.

60. Muhammad G, Diana L, Ulum AB. Numerical Study Analysis of The Effect of Trailing Edge Thickness of Low-Pressure Steam Turbine Stator on Steam Condensation. 2021 International Electronics Symposium 2021, pp. 380-385, https://doi.org/10.1109/IES53407.2021.9593946.

61. Miyazawa H, Uemura A, Furusawa T, Yamamoto S, Yonezawa K, Umezawa S, Ohmori S, Suzuki T. Unsteady Flow Simulation Through Stator-Rotor Blade Rows in Intermediate-Pressure Steam Turbines With Cutback Blades. Proceedings of the ASME Turbo Expo 2020: Turbomachinery Technical Conference and Exposition. https://doi.org/10.1115/GT2020-14937

62. Wen Ch, Yang Y, Ding H, Sun Ch, Yan Y. Wet steam flow and condensation loss in turbine blade cascades. Applied Thermal Engineering 2021, vol. 189, 116748.

63. Tavassoli E, Tamimi M. Effects of Steam Turbine Last Stage Blade Profile Modification on Performance Considering the Spontaneous Condensation of Nonequilibrium Phenomenon: Changing the Blade Chord Length. 2023. Available at SSRN: https://ssrn.com/abstract=4541244 or http://dx.doi.org/10.2139/ssrn.4541244

64. Schippling S, Fuhrer C, Vogt DM. Aerodynamic Parametrization of Last Stage Steam Turbine Blades. Proceedings of the ASME Turbo Expo 2023: Turbomachinery Technical Conference and Exposition. https://doi.org/10.1115/GT2023-103951

65. Keisari S and Shams M, Shape optimization of nucleating wet-steam flow nozzle, Applied Thermal Engineering 2016, vol. 103, pp. 812-820.

66. Zhao S, Li X, Jia Z. Relation between the divergent section's angle and two-phase heat in the condensation flow of wet steam in a supersonic nozzle. Multiscale and Multidiscip. Model. Exp. and Des. 2024, vol. 7, pp. 777-785.

67. Nugraha AD, Fairin MK, Malik ZH et al. Tilt Angle Optimization of Steam Turbine Blade Model Based on Aluminium: The Multi-Simulation Perspective. Journal of Engineering Science and Technology Review 2023, https://api.semanticscholar.org/CorpusID:263179679

68. Majkut, M., Dykas, S., & Smołka, K. (2020). Light extinction and ultrasound method in the identification of liquid mass fraction content in wet steam. Archives of Thermodynamics, 41(4), 63–92.

69. Twomey S. On the Numerical Solution of Fredholm Integral Equations of the First Kind by the Inversion of the Linear System Produced by Quadrature. Journal of the ACM 1963, vol. 10, no. 1, pp. 97-101.

70. Majkut M. Monografia: ZAAWANSOWANE TECHNIKI BADAŃ EKSPERYMENTALNYCH I WIZUALIZACJI PRZEPŁYWU GAZÓW ŚCIŚLIWYCH W MASZYNACH ENERGETYCZNYCH, WYDAWNICTWO POLITECHNIKI ŚLĄSKIEJ, GLIWICE 2019

71. Shan L, Xu L, Cao L, et al. Inversion of particle size distribution based on iterative non-negative Philips-Twomey algorithm. Transactions of the Institute of Measurement and Control 2019, vol. 42, no. 4, pp. 805-812.

72. Alam, M. M. A., Takao, M., & Setoguchi, T. (2017). Numerical Simulation of Non-Equilibrium Two-Phase Wet Steam Flow through an Asymmetric Nozzle. Fluids, 2(4), 63.

73. Halama, J., & Fořt, J. (2013). Numerical simulation of transonic flow of wet steam in nozzles and turbines. Computing, 95(1), 303–318.

74. Fuchs NA, Sutigin AG, HIGH-DISPERSED AEROSOLS. International Reviews in Aerosol Physics and Chemistry, 1971.

75. Lampart P. Numerical optimization of stator blade sweep and lean in an LP turbine stage. Proceedings of IJPGC.02, International Joint Power Generation Conference 2002.

List of Figures

147

List of Tables

Abstract

Steam turbines play a vital role in energy and industrial sectors due to their high efficiency and reliability. Among various turbine stages, the low-pressure (LP) stage is of particular interest because of the formation of wet steam caused by condensation during expansion. This phenomenon leads to energy losses, reduced efficiency, and mechanical issues such as blade erosion due to droplet impact. The present thesis focuses on investigating and improving the performance of the LP stage of a steam turbine by analyzing the behavior of wet steam through advanced numerical simulations and experimental comparisons.

To achieve this, several CFD models were evaluated, and their results were validated using experimental data from a Laval nozzle and a linear blade cascade. Among the tested models, those using Gyarmathy and Fuchs-Sutugin droplet growth approaches coupled with appropriate equations of state showed the most accurate predictions. These findings emphasize the need for careful selection of numerical models to reliably simulate wet steam flows.

Furthermore, detailed 3D simulations were conducted on the last stage of a 200 MW steam turbine to analyze the impact of condensation on flow behavior and efficiency. The results revealed that the stator blades contribute significantly to overall losses, with entropy generation concentrated near the stator hub and rotor shroud. Condensation was found to alter shock wave patterns, reduce Mach numbers in high-wetness regions, and lower outlet flow angles, ultimately decreasing stage efficiency and power output.

In the final stage of this study, various stator blade modifications were tested, including spanwise rotation, pitch changes, profile alterations, and axial/circumferential sweeps. The Bakhtar profile combined with a circumferential lean in the direction of rotor rotation showed the best performance, improving stage efficiency by 3.2%. These results underscore the critical influence of blade geometry on the aerodynamic and thermodynamic performance of wet steam turbines.

Overall, this work contributes to the development of accurate numerical tools for predicting condensation effects in steam turbines and provides practical guidelines for blade design improvements aimed at minimizing energy losses and enhancing turbine efficiency.

Streszczenie

Turbiny parowe odgrywają kluczową rolę w sektorze energetycznym i przemyśle dzięki swojej wysokiej sprawności i niezawodności. Szczególne znaczenie dla osiągania wysokich sprawności ma stopień niskociśnieniowy (LP), w którym podczas rozprężania pary dochodzi do zjawiska kondensacji i powstania pary mokrej. Prowadzi to do strat energetycznych, obniżenia sprawności oraz problemów mechanicznych, takich jak erozja łopatek spowodowana uderzeniami kropel. Niniejsza praca poświęcona jest analizie zachowania pary mokrej oraz poprawie wydajności ostatniego stopnia turbiny parowej przy użyciu zaawansowanych symulacji numerycznych oraz porównań z danymi eksperymentalnymi.

W ramach pracy oceniono kilka modeli CFD, a ich wyniki zweryfikowano na podstawie danych eksperymentalnych uzyskanych z dyszy Lavala oraz liniowej kaskady łopatkowej. Modele oparte na równaniach wzrostu kropel Gyarmathy'ego i Fuchsa-Sutugina, w połączeniu z odpowiednimi równaniami stanu, wykazały największą dokładność. Wyniki te podkreślają znaczenie odpowiedniego doboru modeli numerycznych dla wiarygodnego odwzorowania przepływu pary mokrej.

Dalsza część pracy obejmuje szczegółowe trójwymiarowe symulacje ostatniego stopnia turbiny parowej o mocy 200 MW. Analiza wykazała, że największe straty energetyczne występują w obszarze łopatek kierowniczych, szczególnie w pobliżu piasty i osłony wirnika. Obecność kondensacji wpływała na układ fal uderzeniowych, zmniejszenie liczby Macha w rejonach o niskim stopniu suchości oraz powodowała spadek kąta wylotowego czynnika, co przekładało się na zmniejszenie sprawności i mocy wyjściowej turbiny.

W końcowym etapie badań przeanalizowano różne modyfikacje łopatek kierowniczych, takie jak zmiany kąta obrotu wzdłuż rozpiętości, skoku, profilu oraz pochyleń osiowych i obwodowych. Najlepsze wyniki osiągnięto dla profilu typu „Bakhtar" z pochyloną łopatką w kierunku obrotu wirnika, co skutkowało wzrostem sprawności o 3.2%. Wyniki analiz pokazują, jak istotny wpływ na charakterystykę aerodynamiczną i termodynamiczną ma geometria łopatki.

Podsumowując, niniejsza praca wnosi istotny wkład w rozwój dokładnych narzędzi numerycznych do modelowania kondensacji pary w turbinach oraz dostarcza praktycznych wskazówek do optymalizacji geometrii łopatek w celu minimalizacji strat i zwiększenia efektywności energetycznej stopni turbiny.